Magnetic Resonance Imaging of Anomalous Diffusion and Entropy in Neural Tissue

BY

Carson Ingo
Honors B.S. (Marquette University) 2002

Thesis

Submitted as partial fulfillment of the requirements
for the degree of Doctor of Philosophy in Bioengineering
in the Graduate College of the
University of Illinois at Chicago, 2013

Chicago, Illinois

Defense Committee:
Richard L. Magin, Chair & Advisor
Thomas H. Mareci, University of Florida
Alex Leow, Psychiatry
Thomas Royston
Xiaohong Joe Zhou

To my family,

Mom, Dad, Natalie, and Ty.

Thanks, Ty, for teaching math that was too difficult for me in the 1^{st} grade.

ACKNOWLEDGMENTS

I thank:

- Professor Richard L. Magin. In these past three years, I've never had so much fun.
- Thomas R. Barrick for providing key insight to successfully implement of this work on a clinical scanner.
- Luis Colon-Perez, William Triplett, and Professor Thomas H. Mareci for setting up the experimental protocols.
- Daniel Plant for assistance in configuring the spectrometer.
- Matt G. Hall for helpful discussions on fitting techniques.
- Professor X. Joe Zhou and Yi Sui for sharing ideas to characterize anomalous diffusion.
- Jennifer Andrew and Bruce & Gayle Wheeler for their hospitality in Gainesville, FL.

I would also like to acknowledge the following funding agencies:

- National Institute of Biomedical Imaging and Bioengineering, NIH R01EB007537.
- National Institute of Neurological Disorders and Stroke, NIH R01NS06336.
- National High Magnetic Field Laboratory, External Users Program ML-MAGIN-001, ML-MAGIN-002, and National Science Cooperative Agreement No. DMR-1157490 between the State of Florida and U.S. Department of Energy.
- The Whitaker Foundation for providing future grant support to continue this work on a 7T clinical scanner at Leiden University, Leiden, Netherlands.

TABLE OF CONTENTS

TABLE OF CONTENTS (Continued)

CHAPTER **PAGE**

LIST OF TABLES

LIST OF TABLES (Continued)

TABLE **PAGE**

LIST OF FIGURES

LIST OF FIGURES (Continued)

FIGURE **PAGE**

LIST OF FIGURES (Continued)

LIST OF ABBREVIATIONS

aDTI	anomalous Diffusion Tensor Imaging
aDWI	anomalous Diffusion Weighted Imaging
AMRIS	Advanced Magnetic Resonance Imaging and Spectroscopy
BET	Brain Extraction Tool
CC	Corpus Callosum
CCC	Central Corpus Callosum
Cor	Cortex
CSF	Cerebral Spinal Fluid
CTRW	Continuous Time Random Walk
DEC	Direction Encoded Color
DTI	Diffusion Tensor Imaging
DWI	Diffusion Weighted Imaging
EPI	Echo Planar Imaging
GM	Gray Matter
HCP	Human Connectome Project
IACUC	Institutional Animal Care and Use Committee

LIST OF ABBREVIATIONS (Continued)

FA	Fractional Anisotropy
FOV	Field of View
LCC	Lateral Corpus Callosum
LQ	Lower Quartile
NHMFL	National High Magnetic Field Laboratory
MLF	Mittag-Leffler Function
MRI	Magnetic Resonance Imaging
MSD	Mean Squared Displacement
pdf	Probability Distribution Function
PGSTE	Pulsed Gradient Stimulated Echo
ROI	Region of Interest
RW	Random Walk
SE	Spin Echo
SGUL	St. George's, University of London
SPIR	Spectral Presaturation by Inversion Recovery
SSGR	Slice Selection Gradient Reversal
StD	Standard Deviation
Str	Striatum

LIST OF ABBREVIATIONS (Continued)

TE	Echo Time
TFE	Turbo Field Echo
Tr	Trace
TR	Repetition Time
UF	University of Florida
UQ	Upper Quartile
UIC	University of Illinois at Chicago
WM	White Matter

SUMMARY

The novelty in this project lies in the cross-pollination of distinct disciplines in physics, information theory, and bioengineering to provide new insight about biological tissue structure. MRI is an ideal tool to non-invasively probe biological tissue and is flexible to allow for measurements at a wide range of temporal and spatial resolutions. By utilizing a generalized mathematical model to interpret the diffusion dynamics, the data is free of statistical assumptions and is allowed to 'talk', such that the continuous time random walk model 'listens' as it converges to a fit that describes a class of diffusion, whether it is normal, sub-, or even super-. Furthermore, this approach is firmly cast in the probabilistic regime with the continuous time random walk so that diffusion decay signal is simply the characteristic function (i.e., Fourier transform) of the probability density function. Consequently, we can integrate information theory via entropy measurements of the characteristic function to formulate the problem of anomalous diffusion as one of statistical 'uncertainty' or 'information', inspired by C. E. Shannon (1). Most importantly, this project has been designed with a scope intended to demonstrate these methods are not only viable research tools, but also translatable to a clinical setting that poses additional hardware and scan time constraints. With these pilot studies, we intend to present a pipeline of new 'information' starting with *ex vivo* healthy adolescent and adult neural tissue in animals and ending with new 'information' in *in vivo* neural anatomy in humans.

CHAPTER 1

INTRODUCTION

The diagnostic capability of magnetic resonance imaging (MRI) is principally dependent on the performance of both system hardware (RF coil arrays, increased gradient strength, and high magnetic fields) and software (parallel processing, compressed sensing, and reconstruction methodology). Another source of contrast lies in the underlying mathematical models of MRI phenomena (2). While the fundamental processes of precession and relaxation encoded in the Bloch equation are the basis for imaging, there is additional contrast available through modulating factors such as chemical exchange, local magnetic field inhomogeneity, and diffusion (3). In the case of diffusion, where the simplest model predicts a single exponential signal decay, $exp[-(bD)]$, (where D is the diffusion coefficient (mm^2/s) and b is a pulse sequence controlled parameter), the restrictions introduced by cell membranes, extracellular matrix and tissue heterogeneity provide a rich mix of phenomena that are both anisotropic and heterogeneous (4). DTI, for example, provides new biomarkers (mean diffusivity and fractional anisotropy) that capture additional anatomical features in the brain (e.g., white matter connectivity and fiber density) (5). Here, we extend classical DTI through fractional order modeling of anomalous diffusion to describe underlying tissue complexity through measurements of signal attenuation at high b-values.

We consider a probabilistic approach to modeling diffusion attenuation in neural tissue by generalizing the underlying random walk statistics (6; 7). The generalization relaxes the

constraint that the diffusing particle must take equal length jumps at regular intervals, by allowing variable increments in both the jump distance and the waiting times between jumps. We allow the statistical properties of the physics to separately fall off with jump length and waiting time probability distributions as inverse power laws ($|x|^{-(1+\beta)}$, $t^{-(1+\alpha)}$) (8; 9). This generalization is formally incorporated into the analysis of MRI diffusion data as the CTRW model (10).

The central feature of Brownian motion is that the mean squared displacement (MSD) grows linearly with time, $\langle x^2(t)\rangle \sim t$. However, three conditions must be satisfied: 1) the increments are normally distributed with zero mean, 2) the increments are independent (i.e., no memory), and 3) the process is continuous with an initial starting value set to zero (11). When any of these conditions are not met, the diffusion process is called anomalous and the MSD grows as a power law, $\langle x^2(t)\rangle \sim t^C$ (12). When $C > 1$, the diffusion process is 'super-diffusive' and when $0 < C < 1$, the diffusion process is 'sub-diffusive'. For Brownian motion, the characteristic function is represented by a mono-exponential decay process with respect to time. In diffusion MRI studies, this is modeled as $exp[-(bD)]$, where D is the diffusion coefficient (mm^2/s) and b is a pulse sequence controlled parameter (13). However, numerous research groups have reported diffusion decay processes which deviate from the mono-exponential model (14; 15; 16; 17; 18; 19; 20; 21).

The RW model is a practical approach to derive the features of Brownian motion. In the RW model, the random walker's motion is governed by two stochastic processes: jump length distance, Δx, and waiting time (between jump lengths), Δt. When these incremental processes

are governed by a finite characteristic waiting time and jump length variance, in the continuum limit as $\Delta x \to 0$ and $\Delta t \to 0$, the diffusion equation naturally arises (i.e., Fick's 2^{nd} law) (6). A generalization to the RW model is the CTRW model in which the incremental processes are no longer constrained by a Gaussian or Poissonian probability distribution function (pdf). Rather, the jump lengths and waiting times are governed by arbitrary and independent pdfs (6; 7). In the most general case, the random walker's motion is represented with fractional powers α and β on the waiting time and jump length intervals, respectively, such that the MSD can be represented as a power law,

$$\langle x^2(t) \rangle \sim t^{2\alpha/\beta}, \tag{1.1}$$

where $0 < \alpha \leq 1$, $0 < \beta \leq 2$, and $2\alpha/\beta = C$. When $2\alpha/\beta = 1$, the process is normal diffusion. When $2\alpha/\beta > 1$, the process is 'super-diffusion'. When $0 < 2\alpha/\beta < 1$, the process is 'sub-diffusion'. Solving the CTRW in the continuum limit yields a characteristic decay process that is represented by the Mittag-Leffler function (22). The MLF is attractive in that it relaxes *a priori* assumptions about the governing statistics of the diffusion process.

In this report, we describe diffusion using the MLF (via α and β) and quantify the uncertainty of the CTRW using entropy for diffusion weighted MRI studies on healthy, fixed rat brains using an imaging spectrometer (Chapters 4 & 5). Furthermore, we investigate the effects of weighting either q (i.e., gradient strength spatial resolution) and Δ (i.e., mixing time) on the data collected in diffusion MRI experiments. To interpret the value of anomalous diffusion features, we measure the amount of 'information' gained about biological tissue features when the diffusion decay process is modeled with a decay function that is not mono-exponential.

Finally, we translate these methods and analyses to a clinical MRI system for anomalous diffusion measurements on healthy human volunteers (Chapter 6). However, before presentation of the experimental results, we first establish the theoretical treatment of the CTRW and entropy (Chapter 2) and motivation for fractional order modeling (Chapter 3).

CHAPTER 2

THEORY

2.1 From random walks to continuous time random walks

In the context of RW theory in which the jump length variances and characteristic waiting times are finite, the one-dimensional Brownian motion of a diffusing particle, $P(x,t)$, in homogeneous and isotropic geometries can be described according to the second order partial differential equation,

$$\frac{\partial P(x,t)}{\partial t} = D\frac{\partial^2 P(x,t)}{\partial |x|^2}, \tag{2.1}$$

where D is the diffusion coefficient. The solution to (Equation 2.1) follows as the familiar Gaussian form,

$$P(x,t) = \frac{1}{\sqrt{4\pi Dt}} exp\Big(- \frac{x^2}{4Dt}\Big). \tag{2.2}$$

However, in the context of CTRW theory in which the jump length variances and characteristic waiting times follow asymptotic power law distributions, the one dimensional anomalous motion of a diffusing particle, $P(x,t)$, in heterogeneous biological tissues characterized by tortuous and porous geometries, can be described with a fractional partial differential equation of the form,

$${}_0^C\mathcal{D}_t^{\alpha}\big(P(x,t)\big) = D_{\alpha,\beta}\frac{\partial^{\beta} P(x,t)}{\partial |x|^{\beta}}, \tag{2.3}$$

where ${}_0^C\mathcal{D}_t^\alpha$ is the α^{th} $(0 < \alpha \leq 1)$ fractional order time derivative in the Caputo form, $\partial^\beta/\partial|x|^\beta$ is the β^{th} $(1 < \beta \leq 2)$ fractional order space derivative in the Reisz form, and $D_{\alpha,\beta}$ is the effective diffusion coefficient (e.g. mm^β/s^α) (23; 24; 25; 26; 27). The closed form solution of (Equation 2.3) can be given in the Fox's H function,

$$P(x,t) = \frac{1}{\beta|x|} H_{3,3}^{2,1}\Big[\frac{-|x|}{D_{\alpha,\beta}^{\frac{1}{\beta}} t^{\frac{\alpha}{\beta}}}\Big| \begin{matrix} (1,\frac{1}{\beta}) & (\alpha,\frac{\alpha}{\beta}) & (1,\frac{1}{2}) \\ (1,1) & (1,\frac{1}{\beta}) & (1,\frac{1}{2}) \end{matrix}\Big]. \tag{2.4}$$

When $\alpha = 1$ and $\beta = 2$, (Equation 2.4) collapses to the Gaussian form in (Equation 2.2) (for proof see (28)). However, the solution to (Equation 2.3) can be more succinctly written by performing a Fourier transform in space ($P(x,t) \rightarrow p(k,t)$) to obtain the characteristic function,

$$p(k,t) = E_\alpha\big(-D_{\alpha,\beta}|k|^\beta t^\alpha\big), \tag{2.5}$$

where E_α is the single-parameter Mittag-Leffler function. The MLF is a well-behaved function defined as a power series expansion,

$$f(z) = E_\alpha(z) = \sum_{k=0}^{\infty} \frac{(z)^k}{\Gamma(\alpha k + 1)}, \tag{2.6}$$

where the Γ function is the generalized form of the factorial function, defined for real numbers (29; 30; 31; 32). When $\alpha = 1$ and $\beta = 2$, (Equation 2.5) collapses to an exponential function in the Gaussian form with respect to k,

$$p(k,t) = exp\big(-D_{1,2}|k|^2 t\big). \tag{2.7}$$

When $\alpha = 1$ and $1 < \beta < 2$, (Equation 2.5) returns a stretched exponential function with respect to k,

$$p(k,t) = exp\big(-D_{1,\beta}|k|^\beta t\big). \tag{2.8}$$

When $0 < \alpha < 1$ and $\beta = 2$, (Equation 2.5) returns a stretched Mittag-Leffler function with respect to t,

$$p(k,t) = E_\alpha\big(-D_{\alpha,2}|k|^2 t^\alpha\big). \tag{2.9}$$

In the most general case of the solution to the diffusion equation shown in (Equation 2.5), the effective diffusion coefficient, $D_{\alpha,\beta}$, has units of $space^\beta/time^\alpha$. In order to formulate (Equation 2.5) such that the diffusion coefficient can be written as $D_{1,2}$ with units of $space^2/time$, we insert parameters μ (space) and τ (time) to give,

$$p(k,t) = E_\alpha\big(-D_{1,2}\frac{\tau^{1-\alpha}}{\mu^{2-\beta}}|k|^\beta t^\alpha\big), \tag{2.10}$$

such that,

$$D_{\alpha,\beta} = D_{1,2}\frac{\tau^{1-\alpha}}{\mu^{2-\beta}}. \tag{2.11}$$

As $\alpha \to 1$ and $\beta \to 2$, the term $(\tau^{1-\alpha}/\mu^{2-\beta}) \to 1$, and, that is to show (Equation 2.10) returns the Gaussian form in (Equation 2.7). The parameters, μ and τ, are needed as an empirical solution to preserve the units for the diffusion coefficient, however, others have derived analogs to these parameters (i.e., Δx, Δt) in conservation of mass problems and heavy tailed limit convergence of fractal and fractional dynamics (22; 33; 34; 35).

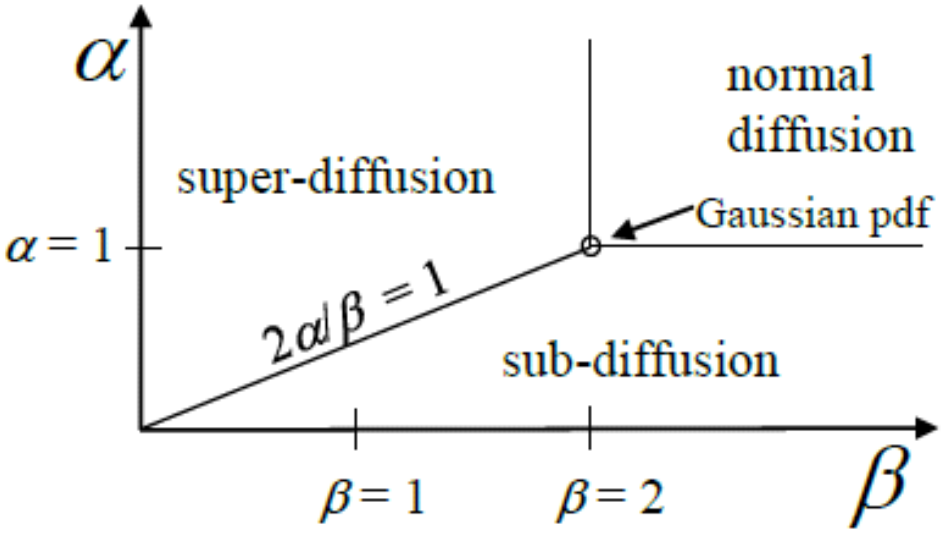

Figure 1. Anomalous diffusion phase diagram with respect to the order of the fractional derivative in space, β, and the order of the fractional derivative in time, α.

A phase diagram of α and β can be constructed to visualize the regions of sub-, super-, and normal diffusion processes as shown in Figure 1. Moving leftward from the point of Gaussian

diffusion ($\alpha = 1, \beta = 2$) by fixing $\alpha = 1$ and decreasing β, the characteristic form of super-diffusion is given by (Equation 2.8) as a stretched exponential function. Moving downward from the point of Gaussian diffusion ($\alpha = 1, \beta = 2$) by fixing $\beta = 2$ and decreasing α, the characteristic form of sub-diffusion is given by (Equation 2.9) as a stretched Mittag-Leffler function. For all other points inside the area bounded by the $\alpha = 1$ horizontal and $\beta = 2$ vertical lines, the characteristic form of anomalous diffusion is given by (Equation 2.10). The $2\alpha/\beta = 1$ diagonal represents effective normal diffusion in which the $\langle x^2(t)\rangle \sim t$, however α and β are fractional and the non-Gaussian waiting time and jump length pdfs vie for competition of the mean-squared trajectory (10).

2.2 From CTRW to diffusion weighted MRI

In spin-echo diffusion MRI experiments, the signal decay, S, is modeled with a mono-exponential as,

$$S/S_0 = exp(-bD), \tag{2.12}$$

where b is the product of the q-space and diffusion time terms, $b = q^2(\Delta - \delta/3)$ (13). For brevity, we will define $\bar{\Delta} = \Delta - \delta/3$. As such, a diffusion weighted experiment can be constructed with a set of b-values, with arbitrary weighting on the q and $\bar{\Delta}$ components, so that a choice can be made to fix $\bar{\Delta}$ and vary q in an array, or to fix q and vary $\bar{\Delta}$ in an array.

In (36), a stretched exponential was fit to data obtained in fixed Δ, varying q experiments with a μ exponent and in fixed q, varying Δ experiments with an α exponent as an approach to independently interrogate fractional space and fractional time diffusion features described in (6), respectively. Additionally, in (21) temporal scaling effects were investigated in variable q and Δ

experiments of a rat hippocampus by utilizing higher moment analysis of the propagator to find parameters, d_w and d_s, as fractal dimensions of the diffusion process and spectra, respectively. We expand upon this previous work by using the generalized solution to the diffusion equation from CTRW theory in (Equation 2.5) and (Equation 2.10) to model anomalous diffusion in MRI as,

$$p(q, \bar{\Delta}) = E_\alpha\big(- D_{1,2}\frac{\tau^{1-\alpha}}{\mu^{2-\beta}}|q|^\beta \bar{\Delta}^\alpha\big), \tag{2.13}$$

where β absorbs the square of the q term to operate as $1 < \beta \leq 2$. With the perspective of the diffusion weighted decay as the characteristic decay function, we also consider an entropy measure as a method to compare and contrast diffusion processes.

2.3 From diffusion weighted MRI to entropy in b-space

In information theory, the amount of uncertainty in a discrete probability density function, $P(x)$ can be measured with,

$$H(x) = -\sum_{i=1}^{N} P(x_i) log_s\big(P(x_i)\big), \tag{2.14}$$

where $H(x)$ is the Shannon information entropy and s is the base of the logarithm (1). With the consideration of information formulated in the context of statistical uncertainty, we have a tool to compare systems governed by differing stochastic processes. For example, when comparing two α-stable distributions, the Gaussian and the Cauchy, normalized with the same full-width, half maximum values, the Cauchy distribution can be shown to have greater information entropy. Non-Gaussian, or anomalous, diffusion phenomena have been correlated to

regions of increased tissue complexity, like the white matter in the brain, which is relatively more anisotropic, heterogeneous, and tortuous compared to gray matter regions. From the information theory perspective, the white matter regions can be considered to have greater entropy than the gray matter regions as they are governed by more uncertain diffusion pdfs.

Another approach to measure the uncertainty in a system is to analyze the characteristic function in terms of the Fourier transform in space ($P(x) \rightarrow p(k)$) with spectral entropy,

$$H_k = -\sum_{i=1}^{N} \frac{\hat{p}(k_i) ln(\hat{p}(k_i))}{ln(N)}, \tag{2.15}$$

where $\hat{p}(k_i) = p(k_i)p^*(k_i)$ reflects the individual wavenumber's contribution to a normalized power spectrum of the Fourier transform, p_k, and the term, $ln(N)$ (i.e., discrete uniform distribution of N samples), is a normalization factor applied so that the spectral entropy, H_k, is between 0 and 1 (37; 38).

Furthermore, as (Equation 2.15) is generally defined to measure the uncertainty of a characteristic function, we can adapt this formalism for b-value diffusion decay signals as a function of q and $\bar{\Delta}$,

$$H(q, \bar{\Delta}) = -\sum_{i=1}^{N} \frac{\hat{p}(q, \bar{\Delta})_i ln(\hat{p}(q, \bar{\Delta})_i}{ln(N)}. \tag{2.16}$$

By inserting the characteristic function in (Equation 2.13) (or, any definition of the characteristic function) into (Equation 2.16), the entropy in the diffusion process can be measured.

2.4 From anomalous DWI to anomalous DTI

To estimate the directional anisotropy of the MLF and entropy parameters, we utilize Gaussian ellipsoids and use a fitting technique previously used to probe diffusion anisotropy in stretched exponential representations of diffusion weighted MRI signal decay to obtain symmetric 3×3 tensors (19). Necessarily, such a fitting procedure requires each MLF parameter to be defined in $n \geq 6$ radial lines through b-space. If the diffusion gradient directions are considered to be unit vectors, $\hat{\mathbf{x}} = \frac{\mathbf{g}}{|\mathbf{g}|} = \begin{pmatrix} g_x & g_y & g_z \end{pmatrix}$, then the ellipsoid representing, for example, α is given by the tensor, $\boldsymbol{\alpha}$ as follows,

$$\begin{aligned} \boldsymbol{\alpha} &= \begin{pmatrix} g_x & g_y & g_z \end{pmatrix} \begin{pmatrix} \alpha_{xx} & \alpha_{xy} & \alpha_{xz} \\ \alpha_{xy} & \alpha_{yy} & \alpha_{yz} \\ \alpha_{xz} & \alpha_{xz} & \alpha_{zz} \end{pmatrix} \begin{pmatrix} g_x \\ g_y \\ g_z \end{pmatrix} \\ &= \alpha_{xx}{g_x}^2 + \alpha_{yy}{g_y}^2 + \alpha_{zz}{g_z}^2 + 2\alpha_{xy}g_xg_y + 2\alpha_{xz}g_xg_z + 2\alpha_{yz}g_yg_z. \end{aligned} \tag{2.17}$$

To determine (Equation 2.17), a set of n simultaneous equations are solved using the general linear model following the methodology in (19). The tensor maps obtained from the MLF parameters, represent the diffusion coefficient, $\mathbf{D}$ computed from $D_{1,2}$, the waiting time exponent, $\boldsymbol{\alpha}$ computed from α, the step length exponent, $\boldsymbol{\beta}$ computed from β, the composite MSD exponent, $\mathbf{C} = 2\boldsymbol{\alpha}/\boldsymbol{\beta}$ computed from $C = 2\alpha/\beta$, and the entropy, $\mathbf{H}$ computed from H. As in classical DTI, after diagonalization, each tensor has 3 positive real eigenvalues, λ_1, λ_2 and λ_3, with corresponding eigenvectors, $\mathbf{v}_1$, $\mathbf{v}_2$ and $\mathbf{v}_3$ oriented along mutually orthogonal principal directions. This formalism allows for familiar scalar invariant maps of isotropy, such as (Tr)

and fractional anisotropy (FA). Since these may be applied to any parameter tensor, we adopt the notation, for example, $Tr(\boldsymbol{\alpha})$ and $FA(\boldsymbol{\alpha})$.

CHAPTER 3

INFORMATION IN TIME- AND SPACE-FRACTIONAL DIFFUSION

3.1 Background

To offer a new way of viewing the utility of fractional order models, we consider fractional calculus from the perspective of information theory (39). The fundamental idea is that fractional order models are better able to represent multi-scale systems because the fractional derivative provides a heuristic tool that includes in its very definition a distribution of time and space constants. Thus, we expect fractional order models to convey more information about the underlying structure and dynamics of complex systems. We apply (Equation 2.15) to diffusion phenomena as expressed by a fractional order random walk model of Brownian motion. In addition to normal, or Gaussian diffusion, this model predicts sub- and super-diffusion regimes, where the underlying dynamics do not follow Gaussian statistics (40; 41). In these regions, the pdf is not always simply expressed analytically in space and time, and we can not directly use (Equation 2.14) to estimate the entropy. In addition, for some cases, the second-moment of the pdf in space (variance), and the first-moment of the pdf in time (mean) will not exist. However, in these cases, the Fourier transform of the pdf, i.e., its characteristic function, can be concisely expressed as a mono-exponential, a stretched-exponential decay, or in general, by the Mittag-Leffler function (24). Hence, we shall be able to use (Equation 2.15) as an information-based tool to measure the entropic content of fractional order diffusion models.

Figure 2 shows three Gaussian probability density functions (pdf) with increasing variances as well as the Cauchy pdf (42). Using (Equation 2.14) with logarithm base $s = e$, the entropy of the Gaussian distribution is shown to have larger entropy values (in units of Nats) as the variance increases (i.e., the distribution spreads out). In order to compare the entropy of the Cauchy pdf with the Gaussian pdf ($\sigma^2 = 1$), we have scaled the two pdfs such that both distributions have equivalent half-width, half-maximum values. Under this condition, the Cauchy pdf has greater entropy than the Gaussian pdf. In general as the tails of the distribution extend, the entropy will increase, as there is an increased uncertainty in the likely location of a randomly selected member of the population.

In order to demonstrate the basics of information theory, we consider two simple stochastic systems: tossing an unbiased coin and tossing an unbiased dice, each with uniform probability distributions of 1/2 and 1/6, respectively. We can estimate the amount of information required to describe each system by applying (Equation 2.14) with logarithm base $s = 2$ (for units of *bits*) to the probability distributions. The dice system is described by $log_2(6)$ (~ 2.58) *bits* of information, whereas the coin system is described by $log_2(2)$, or one *bit* of information. As such, we argue the dice system has more information compared to the coin system because there are more possible states and, therefore, the uncertainty in the probability distribution is greater.

3.2 Results and Discussion

We calculated the entropy for the CTRW model of diffusion by substitution of (Equation 2.5) into (Equation 2.15) and evaluated for permutations of $0 < \alpha \leq 2$ and $0 < \beta \leq 4$. The calculations were performed in Matlab (Mathworks, Natick, MA) using the Mittag-Leffler algorithm

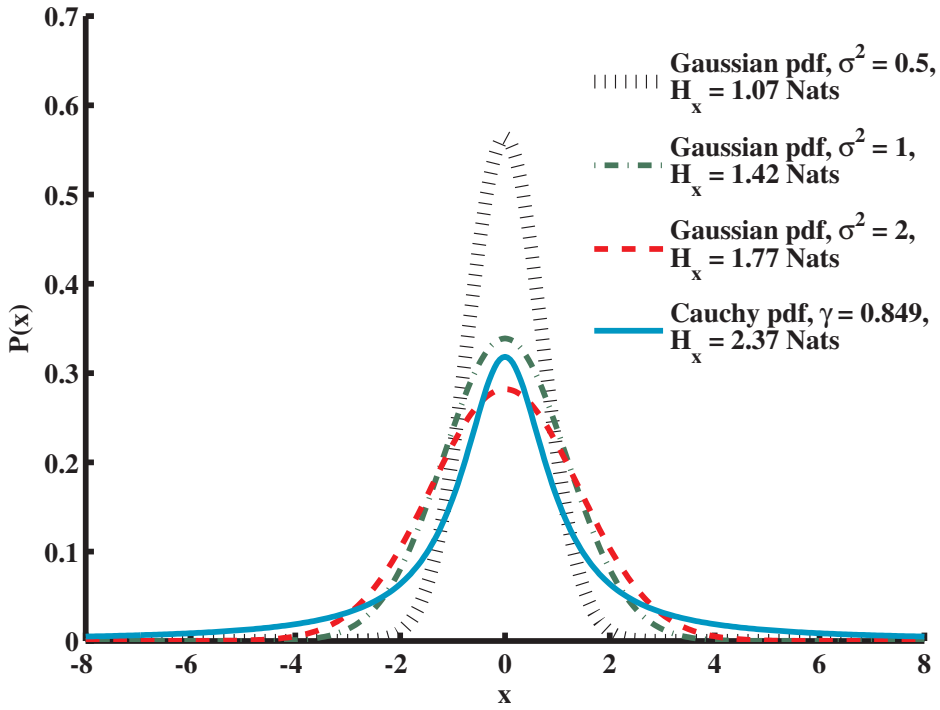

Figure 2. Plot of Gaussian and Cauchy pdfs with associated increasing entropy values.

published in (43), The results are presented in Figure 3 as a three-dimensional entropy surface drawn above a plane defined by the positive values of α and β. The floor of the plot is essentially the phase diagram shown in Figure 1. The overall shape of the surface resembles a small canyon with a stream of low entropy (near $\alpha = 1$) that flows in the direction of increasing β. The Gaussian, or normal distribution ($\alpha = 1$ and $\beta = 2$) appears near the bottom. The cross-

sectional shape of the canyon changes with time and with the assumed value of the diffusion constant.

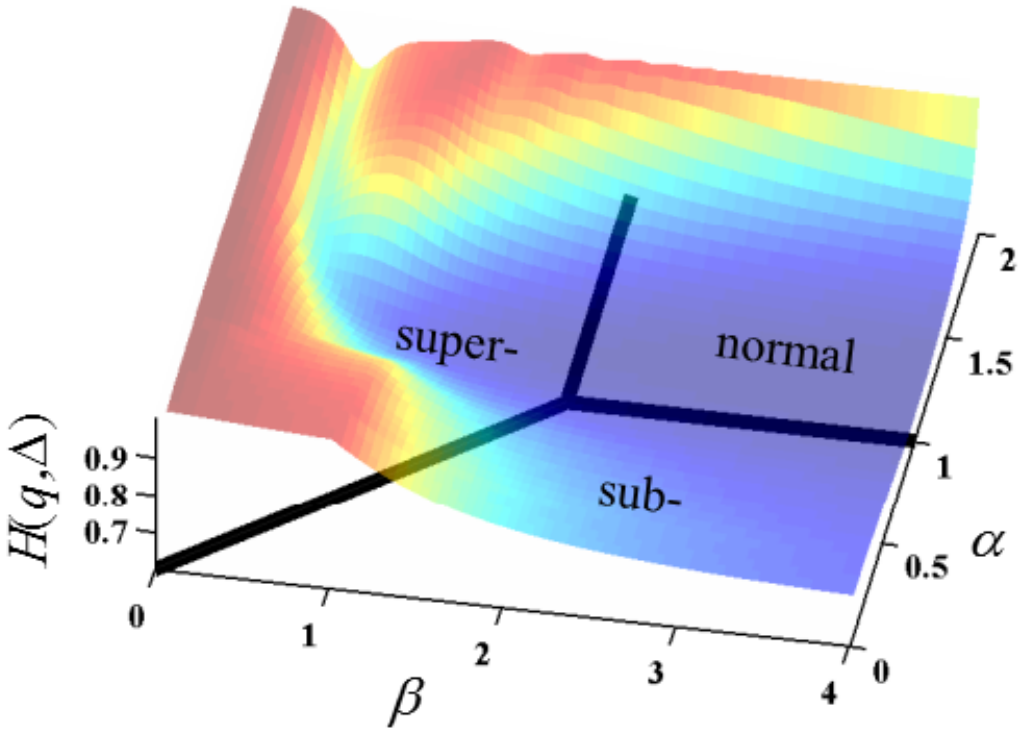

Figure 3. Spectral entropy surface plot for the Mittag-Leffler spatial frequency distribution function (Equation 2.5) with respect to the order of the fractional space derivative, β, and the order of the fractional time derivative, α ($D_{\alpha,\beta} = 1, t = 1$).

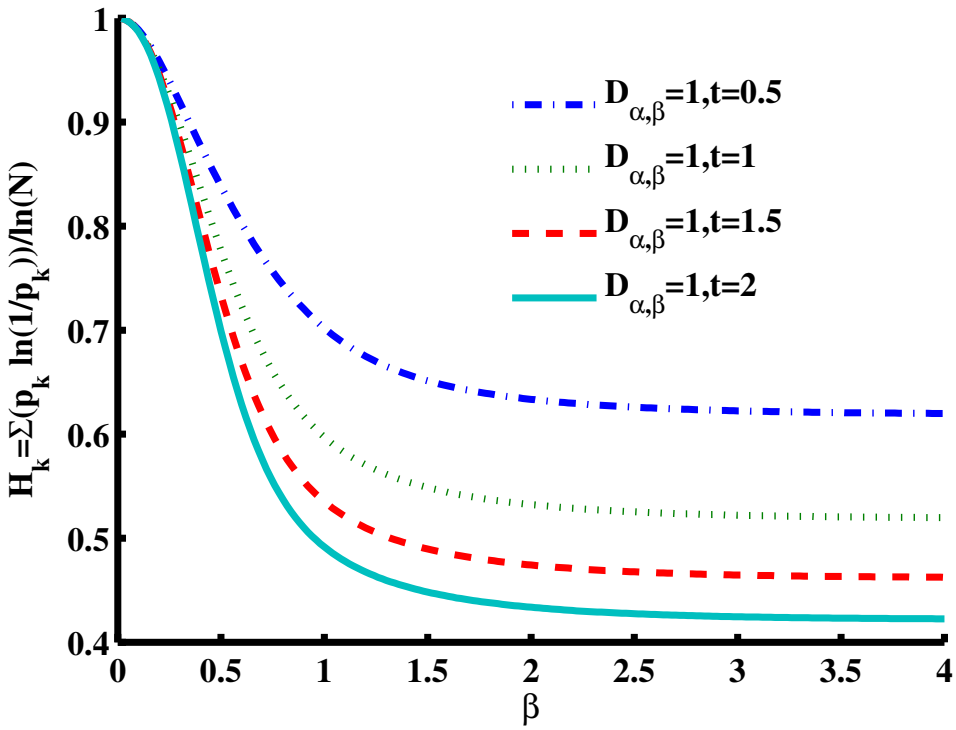

Figure 4. Spectral entropy for (Equation 2.5) with respect to the order of the fractional space derivative, β, with diffusion time cases where $t = 0.5, 1, 1.5, 2$ for $\alpha = 1$ and $D_{1,\beta} = 1$.

Figure 4 is a slice of the spectral entropy surface (for $\alpha = 1$ and four values of time) from the $\beta = 0$ rim out to the distance of $\beta = 4$. Selecting one case of the argument, say $D_{1,\beta} = 1, t = 1$, and starting at $\beta = 2$, we observe that the entropy increases as β gets smaller, with $\sim 20\%$ increase in the normalized spectral entropy when $\beta = 1$ (the Cauchy distribution); whereas travel in the direction of increasing β is mostly flat by this measure of entropy. From the Gaussian location, $\beta = 2$, the entropy appears to converge to a value near 0.5 for increasing β,

while for decreasing β the entropy increases in a monotonic manner at short times. For longer times, as β decreases below 2, the entropy first falls to a minimum and then rises sharply, but overall the effect of increasing time (or larger values of the diffusion coefficients) is to narrow the peak in normalized entropy and to move it closer to the rim. This area of the phase diagram (Figure 1: $\alpha = 1$ and $0 < \beta < 2$) is one of super-diffusion, and it is encouraging that this perspective portrays the region is one of higher entropy (in comparison with the Gaussian diffusion case).

Figure 5 is a slice of the spectral entropy surface (for $\beta = 2$ and four values of time) from the $\alpha = 0$ rim out to the distance of $\alpha = 2$. Selecting one case of the argument, say $D_{\alpha,2} = 1, t = 1$, and starting at $\alpha = 1$, we observe the entropy increasing in both directions, overall. Again, the depth of minimum grows for longer times, but in this cross sectional view, the location is in the direction of higher values of α. As is shown in the phase digram (Figure 1) when $\beta = 2$, values of $\alpha > 1$ are in a region of super-diffusion, and values of $\alpha < 1$, are in a region of sub-diffusion. Also, in Figure 5 we observe that for a specific value of time (and diffusion coefficient constant) the entropy generally increases (from the Gaussian diffusion case of $\alpha = 1$) as the value of α increases (super-diffusion), and as it decreases (sub-diffusion). Thus, both higher and lower values of the order of the fractional derivative α (relative to $\alpha = 1$) give higher entropy values.

In both Figure 4 and Figure 5, it is interesting to note that as the product of the diffusion coefficient and the time increases, the spectral entropy decreases. Mathematically, this behavior is consistent with the Fourier-transform duality between the space and the spatial frequency domains, in which the diffusion coefficient and time, $D_{\alpha,\beta}t$, change position from the

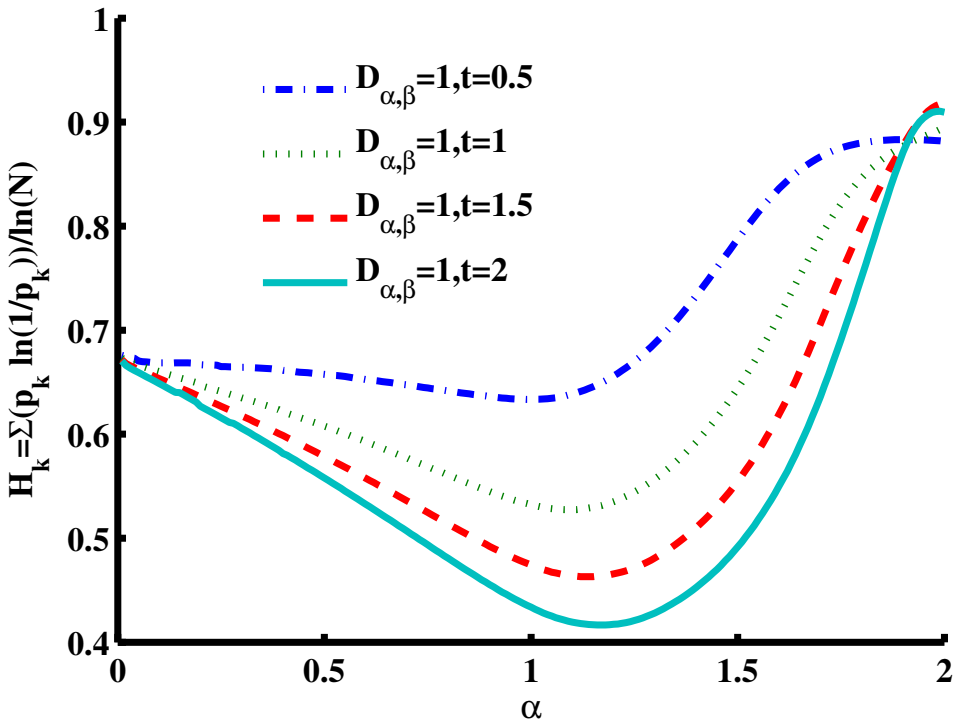

Figure 5. Spectral entropy for (Equation 2.9) with respect to the order of the fractional time derivative, α, for four diffusion time cases where $t = 0.5, 1, 1.5, 2$ for $\beta = 2$ and $D_{\alpha,2} = 1$.

denominator to the numerator of the argument (see (Equation 2.2) and (Equation 2.7) for the case of a Gaussian pdf). Thus, as diffusion time increases – in the framework of the space domain – we expect the distribution to widen and the entropy to increase (increasing variance for the Gaussian). Conversely, as the diffusion time increases – in the framework of the spatial frequency domain – we expect the distribution to narrow and the entropy to decrease. From a CTRW physical model perspective, as the diffusion time increases in the spatial domain, we

argue that the distribution widens and the entropy increases as a dynamic measure by which the uncertainty in predicting the location of the diffusing particle increases. As such, more information is required to specify the spatial location of the particle as the diffusion time increases. Conversely, as the diffusion time increases in the spatial frequency domain, we argue that the distribution narrows and the entropy decreases as a dynamic measure by which the amount of information to be gained about the diffusion environment decreases. Therefore, as the CTRW process progresses in time, the environment becomes completely explored and no new information can be captured about the system, albeit at the cost of maximum uncertainty about the particle's location in space.

In order to examine further the factors that are summed in (Equation 2.15) we plot (for a fixed diffusion coefficient and time) a single spectral entropy term as a function of spectral frequency for a series of β values in Figure 6 (stretched exponential function) and a series of α values in Figure 7 (stretched Mittag-Leffler function). Each curve shown in Figure 6 is a plot of the distribution of spectral entropy. Here for $\beta = 2$ we view the characteristic Gaussian shape, and as β decreases into the domain of super-diffusion, the spectrum appears to narrow, but in fact, due to the long power law tail, it actually spreads out, expanding the number and the range of higher spatial frequency components. The sum of many of these terms can be interpreted as adding information to the corresponding spatial distribution, increasing its variance and its entropy (as illustrated in Figure 2). Also, in this figure, we note that the Cauchy distribution ($\beta = 1$) has, in comparison with the Gaussian distribution, a wider spectral distribution, with a corresponding increase in spatial complexity and entropy (also noted in Figure 2).

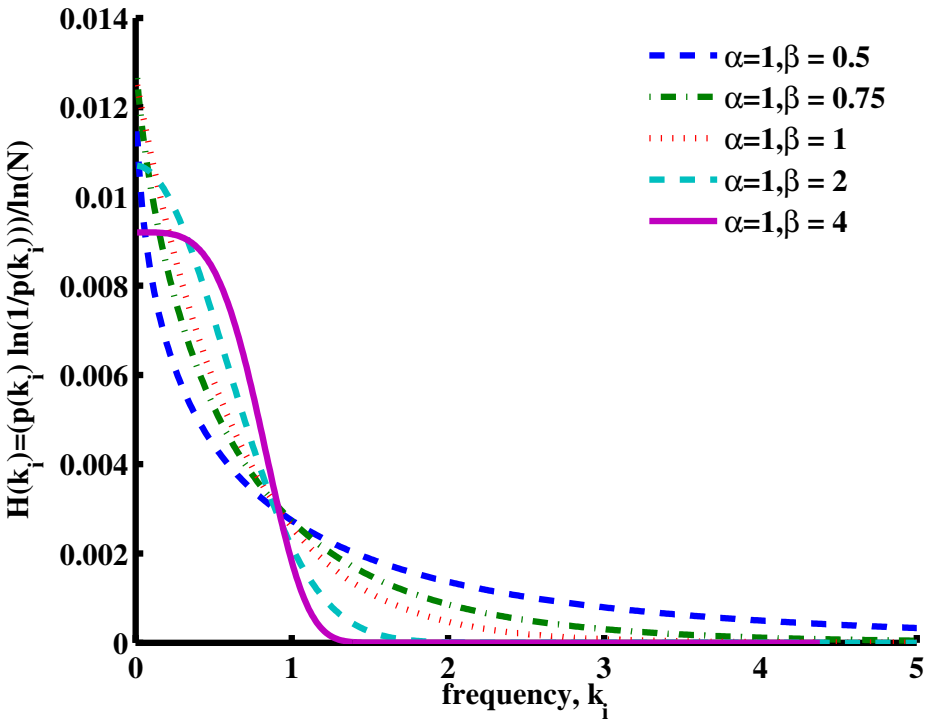

Figure 6. Plot of the individual frequency contributions to the spectral entropy of (Equation 2.5) when the order of the fractional space derivative $\beta = 0.5, 0.75, 1, 2, 4$ for $\alpha = 1$, $D_{1,\beta} = 1$, and $t = 1$.

The spectral entropy plotted in Figure 7 has similar features. For $\alpha = 1$ we have the expected Gaussian distribution of spectral entropy. When α is reduced to 0.5, the spectra expands (higher uncertainty, higher entropy), and when α is increased to 1.5 and to 2 an oscillation appears in the spectra due to the behavior of the Mittag-Leffler function that again pushes more spatial frequency components into the higher range. Such components would be

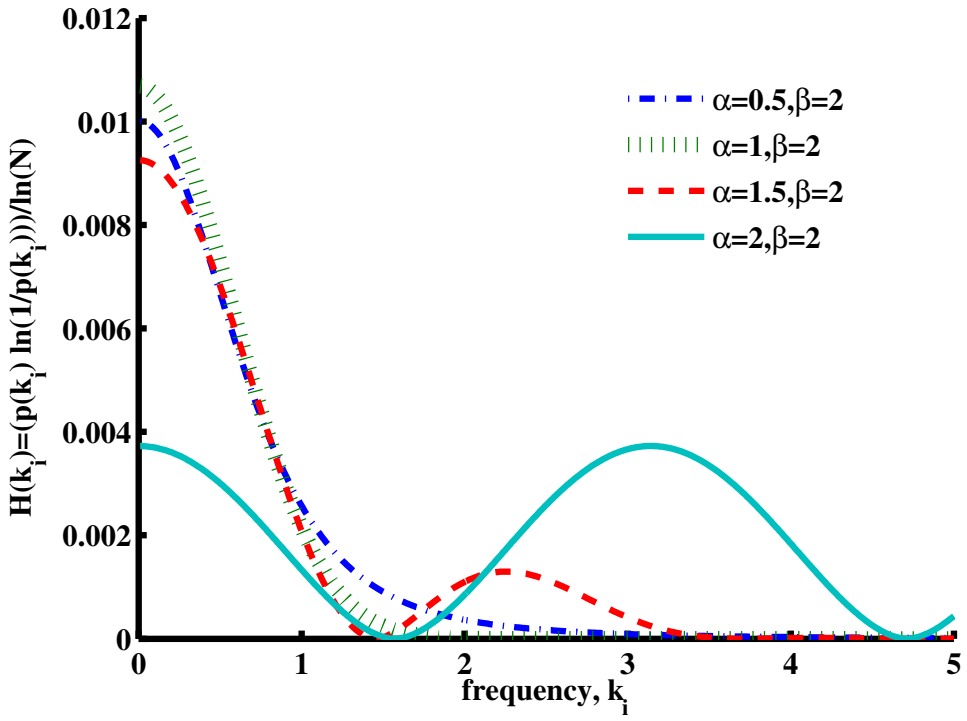

Figure 7. Plot of the individual frequency contributions to the spectral entropy of (Equation 2.9) when order of the fractional time derivative $\alpha = 0.5, 1, 1.5, 2$ for $\beta = 2$, $D_{\alpha,2} = 1$, and $t = 1$.

expected to add uncertainty and entropy to the spatial distribution. In the case of $\alpha = 2$ we have a cosine function in spatial frequency, which corresponds to a single very small spatial feature (a Dirac Delta function) in space.

3.3 Conclusions

The primary conclusion of this study is that the total spectral entropy can be used as a measure of the information content in a fractional order model of anomalous diffusion. In this paper both the space (β) and the time (α) fractional order dependence are expressed separately via generalized fractional order space- and time-derivatives. The classical, Gaussian case of normal diffusion ($\alpha = 1$; $\beta = 2$) falls near the global minimum of a 3D plot of the spectral entropy for the selected range of α and β. In all directions from the minimum on this surface the entropy increases, both for increasing and for decreasing values of the orders of fractional differentiation. The specific increase in entropy is uniquely characterized by a single parameter stretched Mittag-Leffler function where α gives the overall functional dependence, and β is a power-law weighting of the spectral frequency in the argument of the Mittag-Leffler function. When either α or β diverge from the Gaussian case, ($\alpha = 1$; $\beta = 2$) the spectra for each component of the total entropy expands or contracts in a manner that captures greater overall information about the system. Finally, there is an overall reduction in the total spectral entropy as time (or the diffusion coefficient) increases, corresponding to a wider spatial distribution of the individual diffusing components, which is consistent with the noted contraction of spectral frequencies in the Fourier spectral domain.

CHAPTER 4

DIFFUSION WEIGHTED IMAGING OF RANDOM WALKS AND ENTROPY IN NEURAL TISSUE

4.1 Methods

To evaluate the MLF parameters in (Equation 2.13) and the entropy, $H(q, \bar{\Delta})$, defined in (Equation 2.16) as potential biomarkers for biological tissue features, we performed diffusion weighted MRI measurements to investigate the effects of arraying q vs. arraying Δ on one healthy fixed 90 day old rat brain. The outcomes of this pilot study will inform the experimental setup of an inter-subject study on samples of healthy 25 day old and 90 day old fixed rat brains. As the scope of this study is to investigate the effects of experimental setup on observed diffusion processes within the same biological tissue, one diffusion weighted gradient direction was used. The y-axis diffusion weighting direction was chosen to evaluate the possibility of anomalous diffusion dynamics along the principal fiber direction of the CC, whereas other studies have reported anomalous diffusion in directions orthogonal to the principal fiber tracts (17; 19). The effects of the diffusion weighting direction on the parameter values will be investigated in future studies to evaluate correlations to tensor metrics (e.g., first eigenvalue and fractional anisotropy).

The animal was prepared according to University of Florida's UF IACUC protocol D710 (44). Overnight, prior to imaging experiments, the rat brain was soaked in phosphate buffered

saline. For the imaging experiment, the rat brain was placed in a 20 mm imaging tube, and the tube was filled with Fluorinert and secured with a magnetic susceptibility-matched plug to minimize vibrational movement due to the pulsed gradients. The rat brain was oriented in the spectrometer such that the anterior-posterior aligned with the main B0 field (z-axis), the superior-inferior with x-axis, and the lateral with the y-axis. At the AMRIS Facility (Gainesville, Florida), PGSTE diffusion weighted experiments were performed on a Bruker spectrometer at 750 MHz (17.6 Tesla, 89 mm bore) with the following parameters: TR=2 s, TE=28 ms, b-values up to 25,000 s/mm^2, $\delta = 3.5$ ms, NA = 2, y-axis diffusion weighting, 1 central slice in the $y - z$ plane, slice thickness = 1 mm, FOV = 27x18 mm, matrix size of 142x94 pixels, in-plane resolution of 190 μm. It should be highlighted that in all experiments, $\delta << \Delta$ to ensure the short-pulse approximation remained valid. Variable TR data (TE = 12.5 ms, TR = 300–3600 ms, increments of 300 ms) were collected to correct the PGSTE data for T1 relaxation effects. Additionally, the PGSTE data was Rician noise corrected. See Appendix for data processing details.

Two fixed Δ, variable q experiments were performed with Δ fixed at 17.5 and 50 ms. Two fixed q, variable Δ experiments were performed with gradient strengths (g_y) at 350 and 525 mT/m to achieve q-values of 52 and 78 mm^{-1}, respectively. For the fixed $\Delta = 17.5\,ms$ experiment, q was arrayed at 0, 39.7, 55.5, 67.7, 95.4, 116.7, 134.7, 150.5, 164.9, 178.1, and 190.3 mm^{-1}. For the fixed $\Delta = 50\,ms$ experiment, q was arrayed at 0, 24.9, 33.8, 40.9, 57.0, 69.4, 79.9, 89.2, 97.7, 105.4, 112.4 mm^{-1}. For the fixed $q = 78\,mm^{-1}$ experiment, Δ was arrayed

at 17.5, 31.5, 45.5, 59.5, 73.5, 87.5, 101.5, 108.5, and 115 ms. For the fixed $q = 52\,mm^{-1}$ experiment, Δ was arrayed at 17.5, 51.5, 85.5, 119.5, 153.5, 187.5, 221.5, 238.5, and 250 ms.

Because the generalized diffusion model in (Equation 2.13) specifies $D_{1,2}$, μ, and τ as a ratio, any number of parameter value combinations can satisfy successful fitting results. To constrain these parameters, $D_{1,2}$, μ, and τ were first estimated using intermediate fits. To estimate the diffusion coefficient, a mono-exponential function was fit to the first 3 low b-value samples, referred to as, D_m. After D_m estimation, two analogous stretched exponential fitting procedures were used to fit the fixed $\bar{\Delta}$ and fixed q experimental data in order to find estimates of μ and τ, denoted as $\bar{\mu}$ and $\bar{\tau}$. The form of these stretched exponential functions utilize the diffusion experiment pulse sequence parameters in order to independently constrain the magnitudes of $\bar{\mu}$ and $\bar{\tau}$. The stretching parameters in these intermediate fits, $\bar{\alpha}$ and $\bar{\beta}$, were each placed over the entire b-value (Eqs. (Equation A.3), (Equation A.6), (Equation A.9)), (Equation A.12)) which differs from the stretching form of $\bar{\Delta}^{\alpha}$ and q^{β} in (Equation 2.13). See Appendix A for fitting details.

Following the intermediate parameter estimations, D_m, $\bar{\mu}$, $\bar{\tau}$, $\alpha = 1$, $\beta = 2$ were used as starting values in the non-linear least squared fit of the Mittag-Leffler function (43) in order to converge upon $D_{1,2}$, μ, τ, α, and β values. $D_{1,2}$, μ, τ were allowed to float $\pm 50\%$ from their initial estimates. The value for α was bounded between 0 and 1.1 and β between 0 and 2.2. All fits were performed with a non-linear least squares fitting algorithm in Matlab (Mathworks, Natick, MA) in which the convergence criteria for the estimated coefficients was 10^{-6}.

To challenge the robustness of the fitting routine to identify the diffusion regimes delineated on the phase diagram in Figure 1 via the MLF parameters, simulations were performed for known permutations of α and β in the presence of random noise added to decay signals. Signals were created for: space- and time-fractional Brownian motion ($\alpha = 0.5$, $\beta = 1$) of the form in (Equation 2.5), Brownian motion ($\alpha = 1$, $\beta = 2$) of the form in (Equation 2.7), space-fractional super-diffusion ($\alpha = 1$, $\beta = 1$) of the form in (Equation 2.8), and time-fractional sub-diffusion ($\alpha = 0.5$, $\beta = 2$) of the form in (Equation 2.9). The simulated random noise was modeled using the Rician noise profile measured from the diffusion experiments and gradually increased until either α or β diverged more than ± 0.1 from their given values. For all simulated permutations of α and β, the estimated values were swithin ± 0.1 from their given values ($p < 0.05$) when random noise was added up to three standard deviations larger than the experimental noise profile.

After the MLF parameters were determined, the characteristic decay curve for $p(q, \bar{\Delta})$ was constructed using N=1,500 increments arrayed over variable q or variable $\bar{\Delta}$ for b-values between 0 and 25,000 s/mm^2. Then, the entropy (defined in (Equation 2.16)) in the diffusion process, as modeled by the MLF, was computed as $H(q, \bar{\Delta})_{MLF}$. For comparison, using the mono-exponential model (D_m) in (Equation 2.12), a characteristic decay curve of N = 1,500 increments arrayed over b-values between 0 and 25,000 s/mm^2 was constructed. The entropy in the diffusion process, as modeled by the mono-exponential function, was computed as $H(q, \bar{\Delta})_{mono}$.

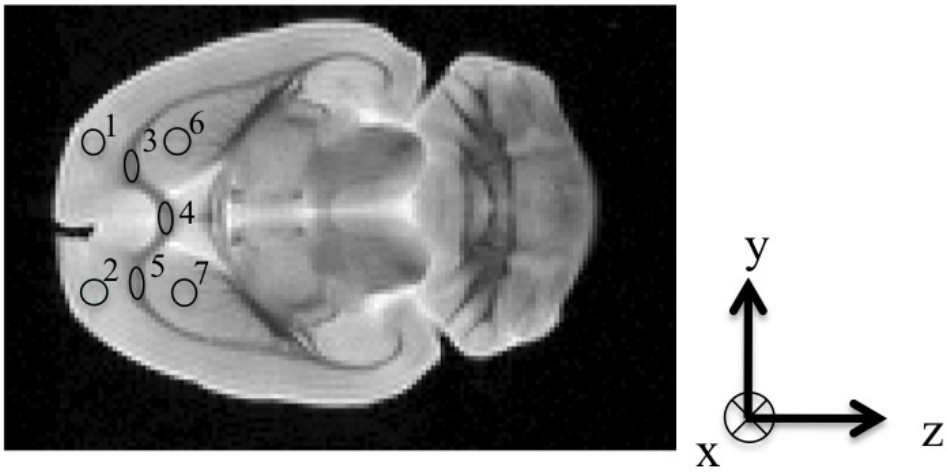

Figure 8. T2-weighted image of an axial slice in a fixed rat brain with ROIs: left (1) and right (2) cerebral cortex; left (3), central (4), and right (5) corpus callosum; left (6) and right (7) striatum.

4.2 Results and Discussion

Figure 8 shows a T2-weighted image of an axial slice through a whole, healthy fixed rat brain with 7 ROIs in the cerebral Cor, Str, and CC. These ROIs were selected in order to analyze tissue compositions ranging from gray matter (cerebral cortex), to a mixture of gray and white matter (striatum), and to white matter (corpus callosum). Furthermore, the y-axis diffusion weighting direction was selected to coincide with the principal fiber orientation of the CCC (ROI 4).

Figure 9 - Figure 12 show the parameter maps for the MLF in (Equation 2.13) and the entropy in (Equation 2.16) in the four fixed $\Delta_1 = 17.5\,ms$, $\Delta_2 = 50\,ms$, $q_1 = 78\,mm^{-1}$,

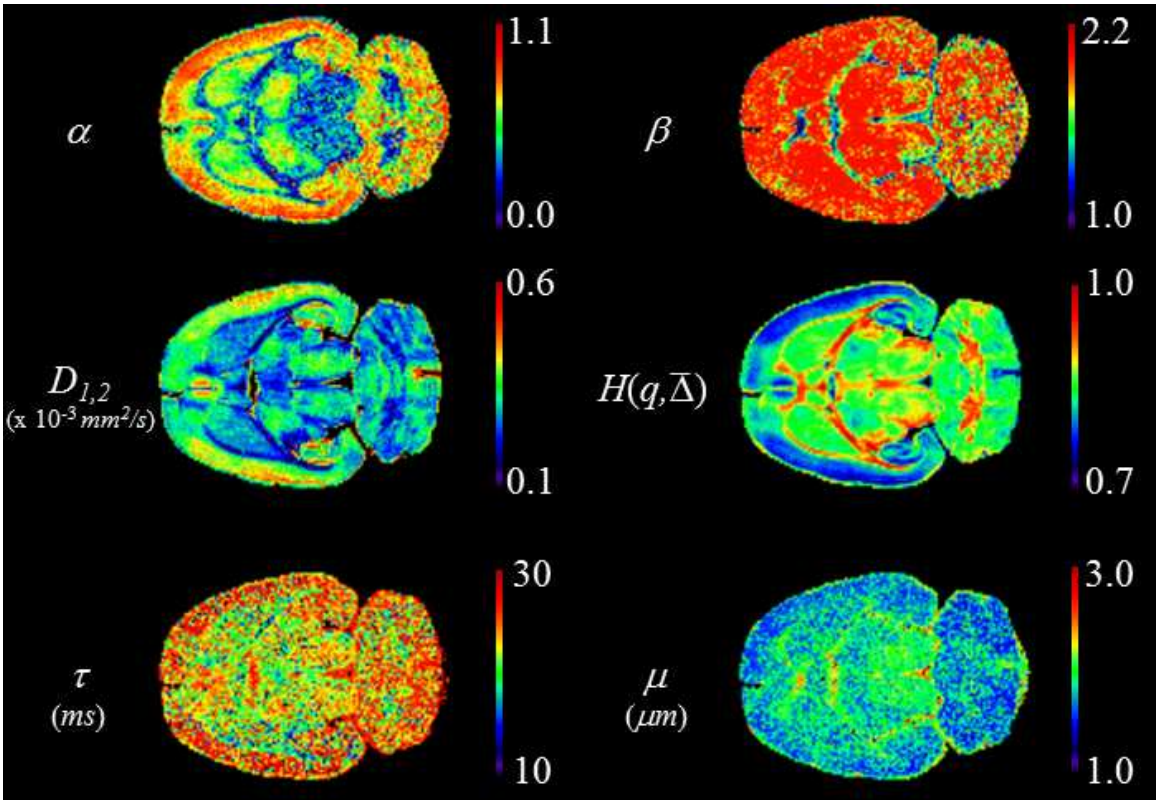

Figure 9. MLF and entropy parameter maps for fixed $\Delta_1 = 17.5\,ms$ experiment (y-axis diffusion weighting).

$q_2 = 52\,mm^{-1}$ experiments. For the 7 ROIs, all numerical values for the MLF parameters in the four experiments are available in the Table XVIII. The results for the MLF parameter maps are reported as the mean and standard deviation values for each ROI. In all experiments, α separated the cerebral cortex (ROIs 1, 2), the CCC (ROI 4), and the striatum (ROIs 6, 7). In the q_1 (Figure 11) and q_2 (Figure 12) experiments, α distinguished the CCC (ROI 4) from

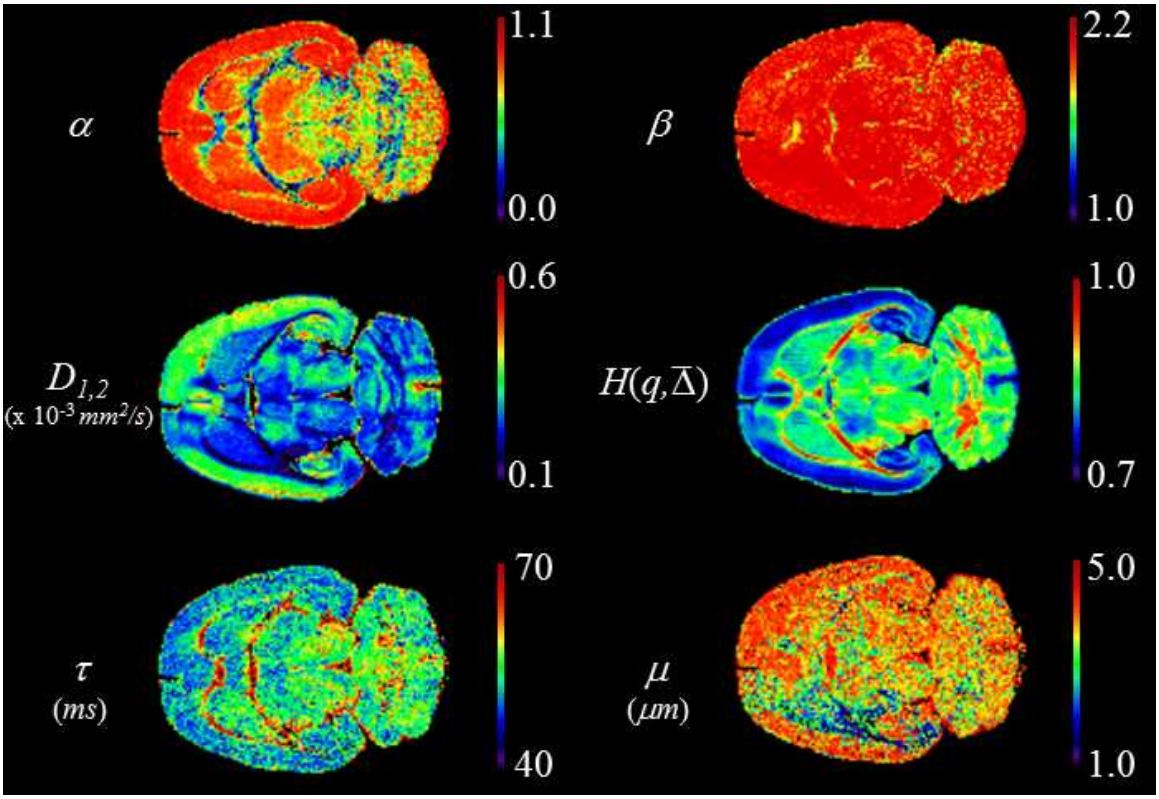

Figure 10. MLF and entropy parameter maps for fixed $\Delta_2 = 50\,ms$ experiment (y-axis diffusion weighting).

the lateral corpus callosum (ROIs 3, 5). In all of the experiments, β showed less contrast than α and for the regions containing gray matter, $\beta \to 2$, indicating Gaussian statistics on the jump length distributions. However, in the Δ_1 (Figure 9) and Δ_2 (Figure 10) experiments, β separated the CCC from the regions containing gray matter (ROIs 1, 2, 6, 7). In the Δ_1 and Δ_2 experiments, the diffusion coefficient, $D_{1,2}$, separated the CCC from the striatum (ROIs 6, 7). In the q_1 experiment, μ separated the CCC from the regions containing gray matter (ROIs 1,

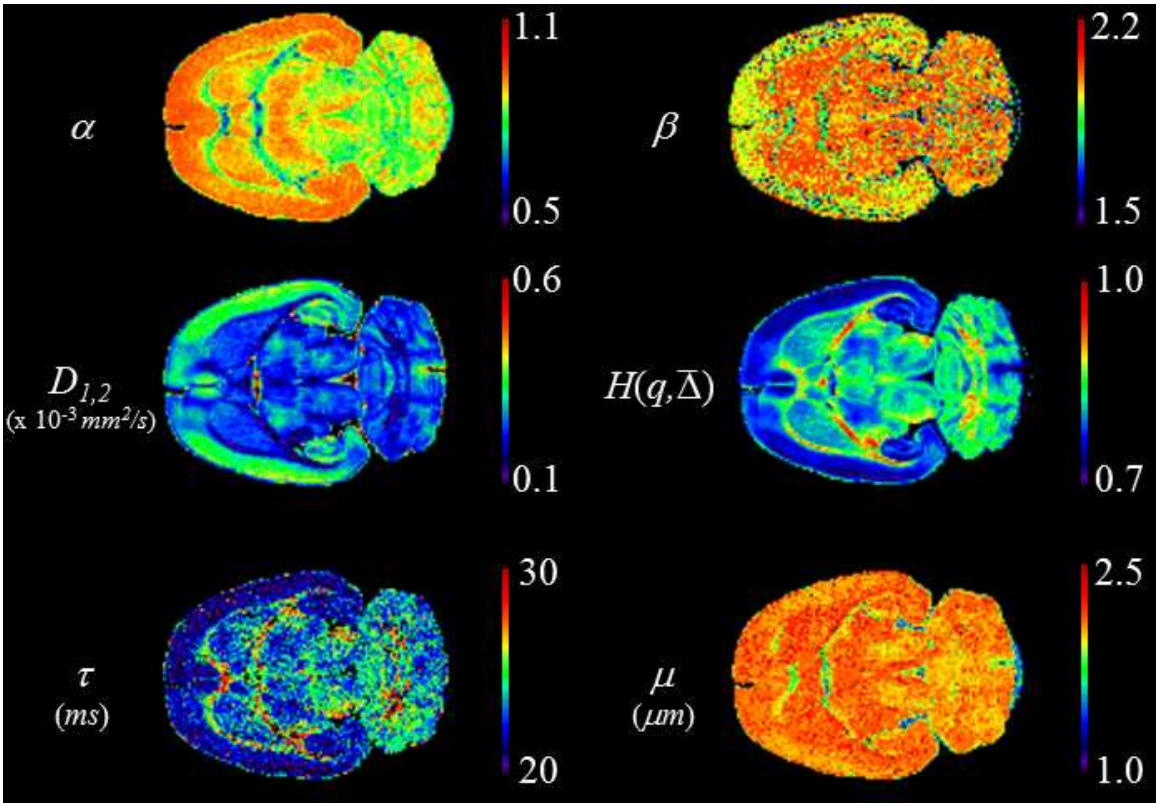

Figure 11. MLF and entropy parameter maps for fixed $q_1 = 78\,mm^{-1}$ experiment (y-axis diffusion weighting).

2, 6, 7). In the Δ_1, Δ_2, and q_1 experiments, τ separated the CCC from the regions containing gray matter (ROIs 1, 2, 6, 7). It should also be noted the mean values across the ROIs for μ and τ had significant change when fixing Δ and fixing q to the different values in the experiments. From the Δ_1 to the Δ_2 experiment, the mean μ scaled from $\sim 2.3\,\mu m$ to $\sim 3.6\,\mu m$ and the

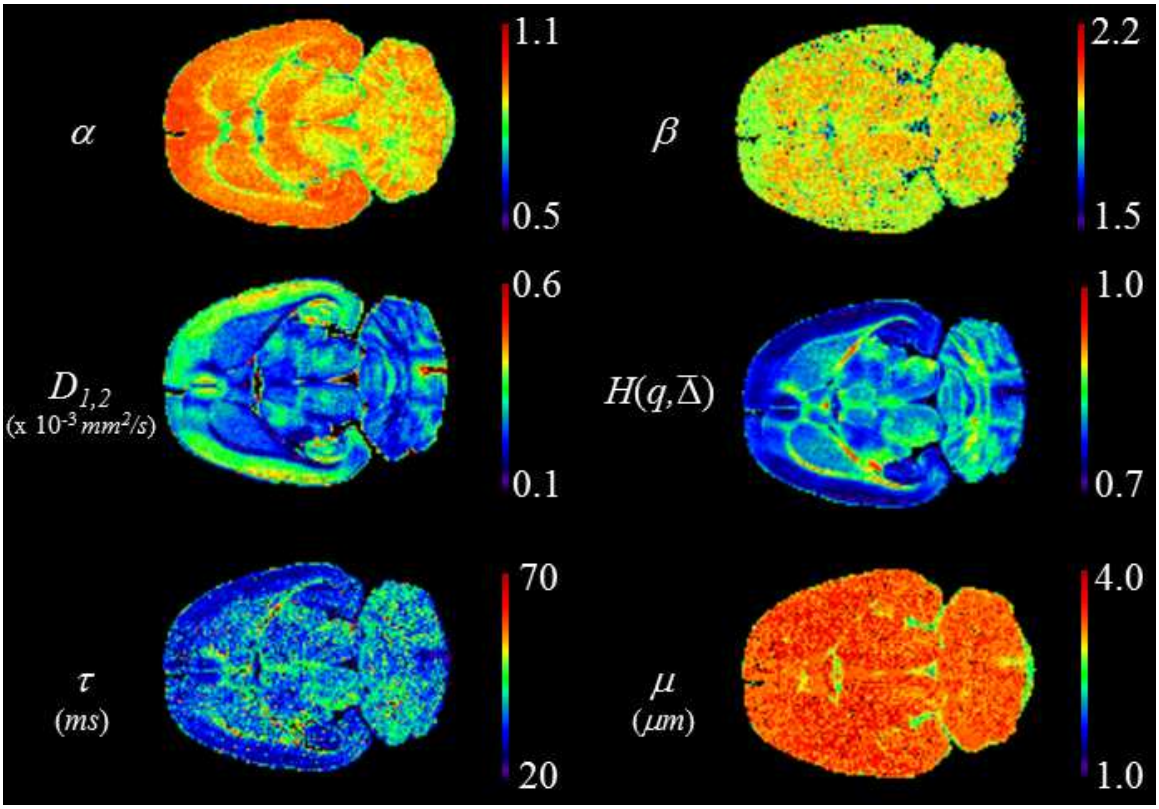

Figure 12. MLF and entropy parameter maps for fixed $q_2 = 52\,mm^{-1}$ experiment (y-axis diffusion weighting).

mean τ scaled from $\sim 19.2\,ms$ to $\sim 57.1\,ms$. From the q_1 to the q_2 experiment, the mean μ scaled from $\sim 2.1\,\mu m$ to $\sim 3.3\,\mu m$ and the mean τ scaled from $\sim 24.1\,ms$ to $\sim 36.8\,ms$.

Table I.a reports the entropy of the characteristic function as represented by the MLF. In the Δ_1, Δ_2, and q_1 experiments, $H(q, \bar{\Delta})_{MLF}$ distinguished the CCC (ROI 4) from the lateral

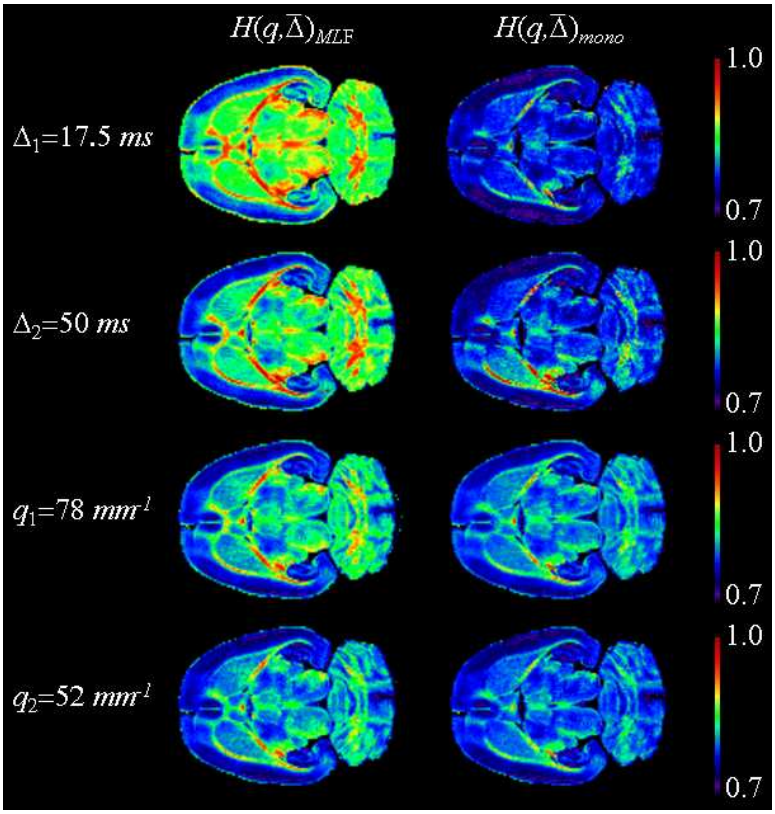

Figure 13. Entropy parameter maps for the MLF (left) and mono-exponential (right) fits of the characteristic function in the $\Delta_1 = 17.5\,ms$ (row 1), $\Delta_2 = 50\,ms$ (row 2), $q_1 = 78\,mm^{-1}$ (row 3), $q_2 = 52\,mm^{-1}$ (row 4) experiments (y-axis diffusion weighting).

white matter (ROIs 3, 5). In the Δ_1, Δ_2, and q_1 experiments, $H(q,\bar{\Delta})_{MLF}$ separated the cerebral cortex (ROIs 1, 2), the CCC (ROI 4), and the striatum (ROIs 6, 7).

Table II shows the ratio, $2\alpha/\beta$ as the composite exponent in the context of the trajectory of the MSD as defined in (Equation 1.1). In the Δ_1 experiment, all ROIs reported sub-diffusion ($2\alpha/\beta < 1$), with the lateral corpus callosum regions growing slowest with respect to time.

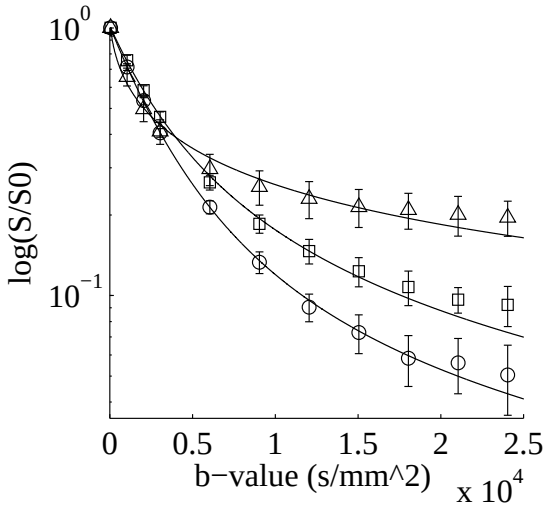

Figure 14. Signal decay plots and MLF fits for the cerebral cortex (ROI 1, circles), striatum (ROI 6, squares), and corpus callosum (ROI 4, triangles) in the $\Delta = 17.5\,ms$ experiment (y-axis diffusion weighting).

In the Δ_2 experiment, the corpus callosum ROIs are most sub-diffusive, whereas the cortex and striatum show slight sub-diffusion and effective normal diffusion ($2\alpha/\beta \to 1$). In the q_1 experiment, the CCC ROI is most sub-diffusive, whereas the cortex and striatum show slight sub-diffusion and effective normal diffusion. In the q_2 experiment, the ROIs report a diminished range of slight sub-diffusion and effective normal diffusion.

In the classical mono-exponential model when α is fixed at 1 and β at 2 in (Equation 2.7), the characteristic function is concisely written as (Equation 2.12), (i.e., $exp(-bD)$). Using entropy, it is possible to measure the amount of 'information' contained in an ROI as the characteristic function deviates from a mono-exponential decay. Table I.b reports the entropy of the

TABLE I

ENTROPY VALUES FOR THE ROIS IN THE FIXED $\Delta_1 = 17.5\,MS$, $\Delta_2 = 50\,MS$, $Q_1 = 78\,MM^{-1}$, $Q_2 = 52\,MM^{-1}$ EXPERIMENTS.

parameter	ROI	Δ_1	Δ_2	q_1	q_2
a. $H(q,\Delta)_{MLF}$	(1) Cor, l	0.82 ± 0.01	0.78 ± 0.01	0.78 ± 0.01	0.76 ± 0.01
	(2) Cor, r	0.83 ± 0.01	0.81 ± 0.01	0.79 ± 0.01	0.78 ± 0.01
	(3) CC, l	0.88 ± 0.02	0.85 ± 0.03	0.83 ± 0.02	0.80 ± 0.02
	(4) CC, c	0.93 ± 0.01	0.91 ± 0.01	0.88 ± 0.02	0.83 ± 0.01
	(5) CC, r	0.88 ± 0.02	0.86 ± 0.03	0.83 ± 0.02	0.81 ± 0.02
	(6) Str, l	0.86 ± 0.01	0.83 ± 0.01	0.82 ± 0.01	0.81 ± 0.01
	(7) Str, r	0.86 ± 0.01	0.83 ± 0.01	0.82 ± 0.01	0.81 ± 0.01
b. $H(q,\Delta)_{mono}$	(1) Cor, l	0.76 ± 0.01	0.75 ± 0.01	0.78 ± 0.01	0.77 ± 0.01
	(2) Cor, r	0.77 ± 0.01	0.80 ± 0.01	0.79 ± 0.01	0.78 ± 0.01
	(3) CC, l	0.76 ± 0.02	0.76 ± 0.04	0.80 ± 0.02	0.78 ± 0.02
	(4) CC, c	0.74 ± 0.01	0.75 ± 0.02	0.81 ± 0.01	0.78 ± 0.01
	(5) CC, r	0.76 ± 0.01	0.79 ± 0.02	0.80 ± 0.01	0.78 ± 0.01
	(6) Str, l	0.78 ± 0.01	0.78 ± 0.01	0.80 ± 0.01	0.79 ± 0.01
	(7) Str, r	0.78 ± 0.01	0.81 ± 0.01	0.80 ± 0.01	0.80 ± 0.01

characteristic function as represented by the mono-exponential. Across all of the experiments, $H(q,\bar{\Delta})_{mono}$ is unable to distinguish between the ROIs. However, a comparison can be made to Table I.a in which the MLF model is used to model the diffusion process. In the Δ_1 experiment, for example, the most information was learned about the diffusion process in the corpus callosum ROIs, followed by Str, and cortex ROIs, respectively. It is interesting to note that the amount of information learned diminishes as the fixed diffusion time increases (i.e., from Δ_1 to Δ_2 experiment) and, inversely, as the fixed diffusion gradient strength decreases (i.e., from q_1 to q_2 experiment). Figure 13 shows the entropy maps for the MLF and mono-exponential models with each experiment demonstrating the improved image contrast in $H(q,\bar{\Delta})_{MLF}$ compared to

TABLE II

$2\alpha/\beta$ COMPOSITE EXPONENT FOR THE ROIS IN THE FIXED $\Delta_1 = 17.5\,MS$, $\Delta_2 = 50\,MS$, $Q_1 = 78\,MM^{-1}$, $Q_2 = 52\,MM^{-1}$ EXPERIMENTS.

ROI	Δ_1	Δ_2	q_1	q_2
(1) Cor, l	0.76 ± 0.08	0.98 ± 0.09	0.98 ± 0.02	1.00 ± 0.03
(2) Cor, r	0.76 ± 0.08	0.92 ± 0.02	0.98 ± 0.03	0.99 ± 0.02
(3) CC, l	0.45 ± 0.12	0.57 ± 0.30	0.86 ± 0.04	0.91 ± 0.03
(4) CC, c	0.74 ± 0.12	0.54 ± 0.05	0.75 ± 0.05	0.84 ± 0.03
(5) CC, r	0.37 ± 0.16	0.56 ± 0.17	0.87 ± 0.05	0.87 ± 0.04
(6) Str, l	0.62 ± 0.08	0.90 ± 0.13	0.90 ± 0.01	0.95 ± 0.03
(7) Str, r	0.58 ± 0.06	0.83 ± 0.03	0.91 ± 0.02	0.94 ± 0.03

$H(q, \bar{\Delta})_{mono}$. It should also be noted that D_m and $D_{1,2}$ were statistically indistinguishable (see Table XVII for comparison), which indicates the diffusion coefficient units were preserved in the MLF fitting routine. Another way to visualize 'information' contained in the characteristic function is simply to look at the diffusion decay signals in log-linear plots, for example, as shown on Figure 14. On this scale, a mono-exponential decay would appear as a straight line, however, the Cor, Str, and CC all deviate as the $b-$values increase. As the corpus callosum data is more anomalous than the Str, and the striatum more anomalous than the Cor, corresponding information is added at high $b-$values to distinguish the ROIs. Figure 14 also shows the MLF curves to demonstrate the small mean squared error of the fits, which is representative for all data analyzed in this study.

In the context of CTRW theory, it is interesting to break down the composite exponent on the MSD trajectory, $2\alpha/\beta$, in the context of waiting time, jump length distributions and entropy.

In the continuum limit, the waiting time ($\Delta t \to 0$) and jump length ($\Delta x \to 0$) increments can be represented, in the most general case, as fractional time and space derivatives of arbitrary orders, α and β, respectively. As the order of the fractional derivatives move away from the special case of Brownian motion ($\alpha = 1$, $\beta = 2$), the waiting times and jump lengths are governed by heavy tailed distributions in which the diffusing particle has a greater probability of waiting longer and jumping further. So, the composite exponent on the MSD trajectory can take on a particular value to indicate sub-diffusive growth, but can be comprised of different combinations of fractional values for α and β. For example, in the Δ_1 experiment, the composite exponents are similar for the right cerebral cortex (~ 0.76) and the CCC (~ 0.74), indicating sub-diffusive growth. However, the individual values of α and β are clearly different for the right cerebral cortex ($\alpha \sim 0.74$, $\beta \sim 1.95$) and the CCC ($\alpha \sim 0.42$, $\beta \sim 1.15$). Therefore, the characteristic function representation for the waiting time and jump length distributions is more uncertain (anomalous) in the CCC compared to the right cerebral cortex. And, this difference is clearly encoded in the entropy with the corpus callosum ($H(q, \bar{\Delta}) \sim 0.93$) and the cerebral cortex ($H(q, \bar{\Delta}) \sim 0.83$). Increasing the diffusion time from the Δ_1 to the Δ_2 experiment, the composite exponent increased for all ROIs, except the CCC where $2\alpha/\beta$ decreased from ~ 0.74 to ~ 0.54. Between these two experiments, there was no significant change in α, however β increased from ~ 1.15 to ~ 1.42 reflecting the smaller range of q-values sampled in the Δ_2 experiment to resolve the spatial component of the anomalous diffusion in this heterogenous and tortuous ROI.

The probabilistic framework of the CTRW models diffusion in any environment that has heterogeneous, tortuous, and multi-scale properties (12, 13, 28–31). In this study, we have applied this abstract approach to the realm of biological tissues and MRI physics. However, work remains to correlate these new parameters to anatomical features as has been done to validate DTI parameters with histology (32–34). It is encouraging to consider the results of this study in the context of high resolution electron micrograph images of fixed mouse neural tissue reported in (45). These images show that although there is a principal fiber direction in the CC, within the resolution of one imaging voxel ($\sim 200\,um$), there are also clearly visible populations of heterogeneous, tortuous, and crossing fibers, particularly in the central region. So, it is a reasonable hypothesis to propose the tissue microstructure is reflected in α as the likelihood for water to be 'trapped' within a hindrance and β as the likelihood for water to 'jump' along a less-hindered environment.

As the images in Figure 9-Figure 13 show, there is new contrast that is different from the diffusion coefficient map. Even where contrast is not as apparent (i.e., β, μ, τ), there is information in the ROI and the experiment. When $\beta \to 2$, the spatial component (i.e. jump length) of the diffusion dynamics approaches the form of a normal distribution. When raising the arguments, q and $\bar{\Delta}$ to fractional powers, μ and τ are required to preserve the units of the diffusion coefficient, and the scale of their values are initially dependent on the diffusion experiment's fixed component (q or Δ) in the b-value array, as described in the Appendix. As the fits for the signal decay data converge to fractional values for α and β, mathematically, the values for μ and τ are affected, and this was observed in the CCC for the Δ_1, Δ_2, and

q_1 experiments, mentioned above. By dissecting and weighting a b-value with its controllable pulse sequence variables, μ and τ are reflective of both the experimental setup and the decay curve. The values for μ are scaled on the order of microns and, perhaps, are indicative of the sub-voxel resolution in the diffusion experiment. Whereas the values for τ are scaled on the order of milliseconds and, perhaps, are indicative of the non-Markovity (i.e., memory) of the diffusion process as the longest times were observed in the central CC, along the principal fiber orientation.

It is difficult to compare the outcomes of this study with respect to other reports of anomalous diffusion modeled with a stretched exponential function. In (7-9), the stretching exponent is raised over the entire $b-$value (i.e., $(q^2\bar{\Delta})$). In (15; 16), the q^2 term is raised by a β parameter, however there is no stretching term on $\bar{\Delta}$ (i.e., $\alpha = 1$) as the Bloch-Torrey equation was generalized solely with a fractional space derivative to arrive at the stretched exponential form. However, it is encouraging to note that the values (i.e., microns) estimated for μ in our study are similar to those reported in (15; 16). In (36), stretching exponents were placed each on q^2 and $\bar{\Delta}$, but were done so with individual fits in which one of the exponents was fixed at a time, whereas our approach ultimately produces a simultaneous estimation of the stretching exponents on q^2 and $\bar{\Delta}$. In (21), numerous diffusion experiments were performed by manipulating the weightings of q and $\bar{\Delta}$ to investigate temporal scaling of fractal measures by applying a $q-$space analysis in a rat hippocampus where sub-diffusive power-law growth of the propagator is also reported.

Finally, it is apparent that how the experiment's parameters are designed, by either arraying the gradient strength or the mixing time, and the weightings therein, affect the diffusion dynamics observed within an ROI. In the context of entropy (Table I and Figure 13) as a measure of 'uncertainty' in the diffusion decay signal, our study suggests that fixing Δ at the shortest time and arraying across a large range of q values produced the most 'information' about the probed neural tissue in comparison to the three other experiments. That is to say, the experiment should minimize the diffusion time such that the water still has enough time to explore the environment, while the gradient strength is maximized to resolve the tissue microstructure within the imaging voxel. From this perspective, it is important that the diffusion experiment is tuned to match the neural tissue under study to observe dynamics, which may not be as clearly resolved if the mixing time or the diffusion gradient strength is not optimal.

4.3 Conclusions

In this study, we approached the diffusion decay signal in the probabilistic regime as a representation of the characteristic function – the Fourier transform of the pdf (46; 47). In the context of CTRW theory, we examined the diffusion dynamics in terms of the waiting time and jump length distributions. For ROIs that are heterogenous and tortuous, like the CC, the representative parameters, α and β, showed deviations away from the Gaussian case of Brownian motion ($\alpha = 1$, $\beta = 2$). To quantify these deviations, we applied entropy as an overall measure of the anomalous nature of the diffusion process. At high b-values, new 'information' was learned by using a model (MLF) that is able to capture heavy-tailed diffusion signal decays which are not mono-exponential. As such, the MLF and entropy parameters are potential

biomarkers for degeneration, plasticity, therapeutic response in neural tissue. It is important to emphasize that the choice of q and Δ impacts the observed outcomes as demonstrated in each of the fixed q and fixed Δ experiments. Future studies will focus on control vs. disease models and histological correlation to these parameters as well as tensor constructs. Additionally, the methods presented in this report will be adapted for human clinical systems (Chapter 6), which have a smaller range of diffusion gradient strengths and mixing times. Finally, we will investigate the directional dependence of the CTRW parameters, and of the entropy, which can in principle – just as the diffusion coefficient – be described with tensor constructs in Chapter 4.

CHAPTER 5

DIFFUSION TENSOR IMAGING OF RANDOM WALKS AND ENTROPY IN HEALTHY AGING OF NEURAL TISSUE

5.1 Methods

To evaluate the MLF parameters in (Equation 2.13) and the entropy, H, defined in (Equation 2.16) as potential biomarkers for biological tissue features, we performed diffusion weighted MRI measurements to investigate the effects of arraying q vs. arraying Δ on three samples of healthy 25 day old and three samples of 90 day old fixed rat brains. Additionally, the scope of this study is to investigate the effects of experimental setup on observed diffusion processes and the directional anisotropy, six diffusion weighted gradient direction were used in order to describe the MLF and entropy parameters in tensor constructs.

The animals were prepared according to University of Florida's UF IACUC protocol D710 (44). Overnight, prior to imaging experiments, the rat brain was soaked in phosphate buffered saline. For the imaging experiment, the rat brain was placed in a 20 mm imaging tube, and the tube was filled with Fluorinert and secured with a magnetic susceptibility-matched plug to minimize vibrational movement due to the pulsed gradients. The rat brain was oriented in the spectrometer such that the anterior-posterior aligned with the main B0 field (z-axis), the superior-inferior with x-axis, and the lateral with the y-axis. At the AMRIS Facility (Gainesville, Florida), PGSTE diffusion weighted experiments were performed on a Bruker

spectrometer at 750 MHz (17.6 Tesla, 89 mm bore) with the following parameters: TR=2 s, TE=28 ms, b-values up to 25,000 s/mm^2, δ = 3.5 ms, NA = 2, 4 central slice in the $y-z$ plane, slice thickness = 1 mm, FOV = 27x18 mm, matrix size of 142x94 pixels, in-plane resolution of 190 μm. The six diffusion weighted gradient directions were $[x, y, z]$ [0 0 1; 0.894429 0 0.44721; 0.276391 0.850653 0.447211; -0.723607 -0.525731 0.447213; 0.276382 -0.850666 0.447193; -0.723607 0.525731 0.447213]. It should be highlighted that in all experiments, $\delta << \Delta$ to ensure the short-pulse approximation remained valid. Variable TR data (TE = 12.5 ms, TR = 300–3600 ms, increments of 300 ms) were collected to correct the PGSTE data for T1 relaxation effects. Additionally, the PGSTE data was Rician noise corrected. See Appendix Afor data processing details.

Based on the experimental outcomes found in Chapter 4, one fixed Δ, variable q experiment was performed with Δ fixed at 17.5 and one fixed q, variable Δ experiment was performed with gradient strengths (g) 525 mT/m to achieve a q of 78 mm^{-1}. For the fixed Δ = 17.5 ms experiment, q was arrayed at 0, 39.7, 55.5, 67.7, 95.4, 116.7, 134.7, 150.5, 164.9, 178.1, and 190.3 mm^{-1}. For the fixed $q = 78\, mm^{-1}$ experiment, Δ was arrayed at 17.5, 31.5, 45.5, 59.5, 73.5, 87.5, 101.5, 108.5, and 115 ms.

For each diffusion weighted gradient experiment, the data were fit to the 1D MLF and entropy parameters as described in (Equation 2.13) and (Equation 2.16). The MLF parameters were estimated using the same methodology described in Chapter 4 and Appendix A. After the MLF parameters were determined, the characteristic decay curve for $p(q, \bar{\Delta})$ was constructed using N=1,500 increments arrayed over variable q or variable $\bar{\Delta}$ for b-values between 0 and

25,000 s/mm^2. Then, the entropy (defined in (Equation 2.16)) in the diffusion process, as modeled by the MLF, was computed as H_{MLF}. For comparison, using the mono-exponential model (D_m) in (Equation 2.12), a characteristic decay curve of N = 1,500 increments arrayed over b-values between 0 and 25,000 s/mm^2 was constructed. The entropy in the diffusion process, as modeled by the mono-exponential function, was computed as H_{mono}. Then, using (Equation 2.17), Gaussian ellipsoids were fitted to obtain tensor maps for each parameter (i.e. $\mathbf{D}$, $\boldsymbol{\alpha}$, $\boldsymbol{\beta}$, $\boldsymbol{\tau}$, $\boldsymbol{\mu}$, $\mathbf{H}$ and $\mathbf{C}$) and were diagonalized to obtain eigenvalues and eigenvectors. Rotationally invariant isotropic (Tr) and anisotropic (FA) maps were computed for each MLF parameter. Eigenvector orientation was visualized using DEC which colors eigenvector orientations red in the sinister-dexter direction, green in the anterior-posterior direction and blue in the superior-inferior direction (48). Brightness of the DEC parameter map was modulated by FA of the parameter. For each sample, based on the T2 weighted image, ROIs were drawn for the central corpus callosum, lateral corpus callosum, striatum, and cerebral cortex, and then parameter maps were constructed for the entire slice. Figure 15 shows the T2 weighted images of the 25 and 90 day old healthy fixed rat brains with ROIs circled in black.

5.2 Results and Discussion

5.2.1 Fixed Δ experiment

For visual comparison in the fixed Δ experiment, the trace maps of the MLF parameters, entropy of the diffusion decay as modeled by the MLF (H_{MLF}), entropy of the diffusion decay as modeled by the mono-exponential (H_{mono}) are shown for a 25 and 90 day sample in Figure 16 and Figure 17, respectively. As shown in Table III, from the adolescent to the adult neural

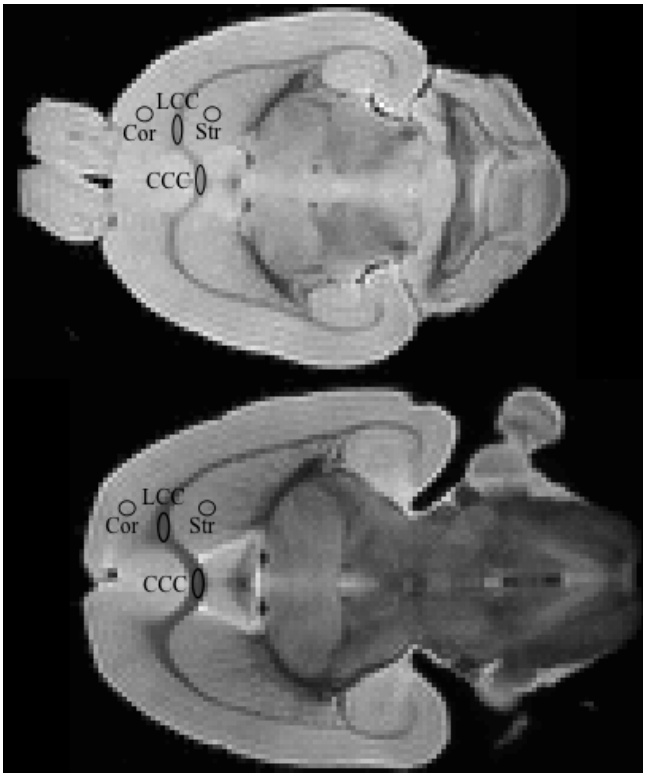

Figure 15. T2-weighted images of 25 day old healthy fixed rat brain (top) and 90 day old healthy fixed rat brain (bottom) with ROIs of the CCC, LCC, Str, and cerebral cortex.

tissue in the CCC, the trace values for α, β, C and D had significant decrease, which is reflected in an increase in the entropy, H. The mean values for the FA measures of α and C increased in the adult samples by $\sim 80\%$, which was more than $FA(D)$ ($\sim 15\%$). There was no change in $FA(H)$ between the two groups. It should be noted that within each group, $FA(D)$ was the most anisotropic parameter.

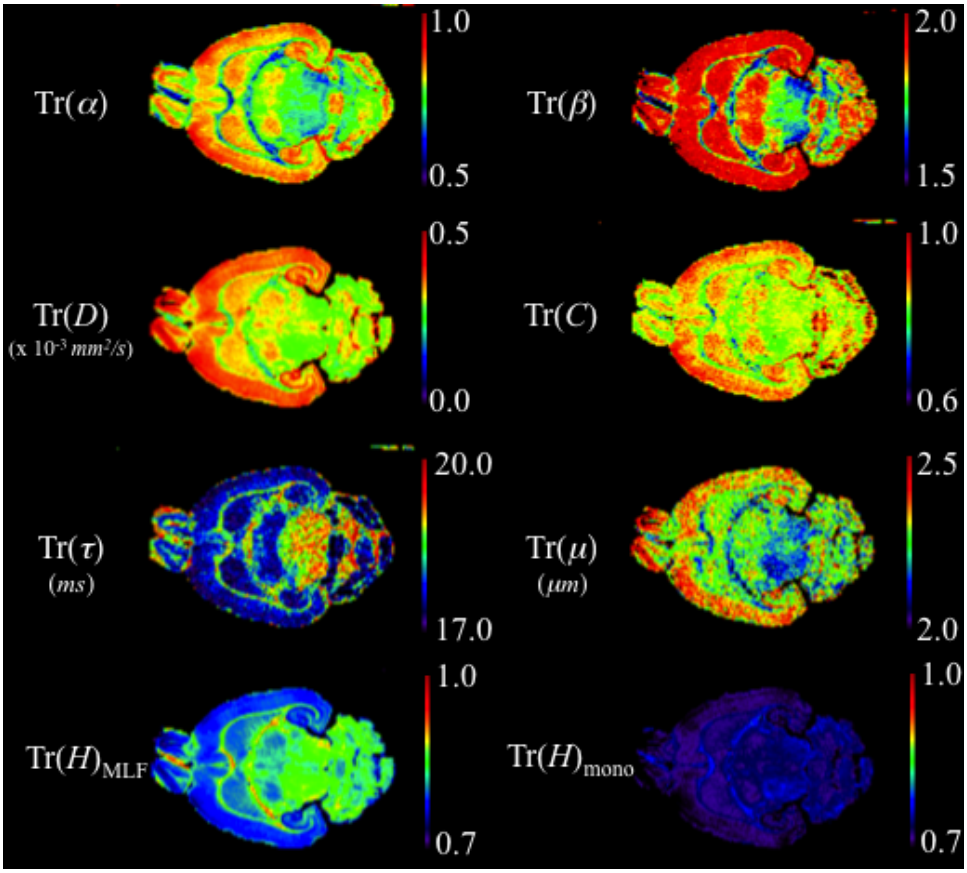

Figure 16. Trace maps of a healthy 25 day old brain in the fixed Δ experiment.

In the LCC (Table IV), the trace values for both α and β significantly dropped from the 25 day to the 90 day samples, which was also reflected in a small increase in H. As C represents the ratio $2\alpha/\beta$, the overall MSD did not change between the groups. Likewise, there was no change in the trace value of D between the groups. Overall, the FA values for α, β, and C were lower in comparison to the CCC ROI (Table III). However, significant increases in the

anisotropic features of α, β, and C were found with age in the LCC, whereas $FA(D)$ only showed a mild increase. $FA(H)$ did not change between the groups.

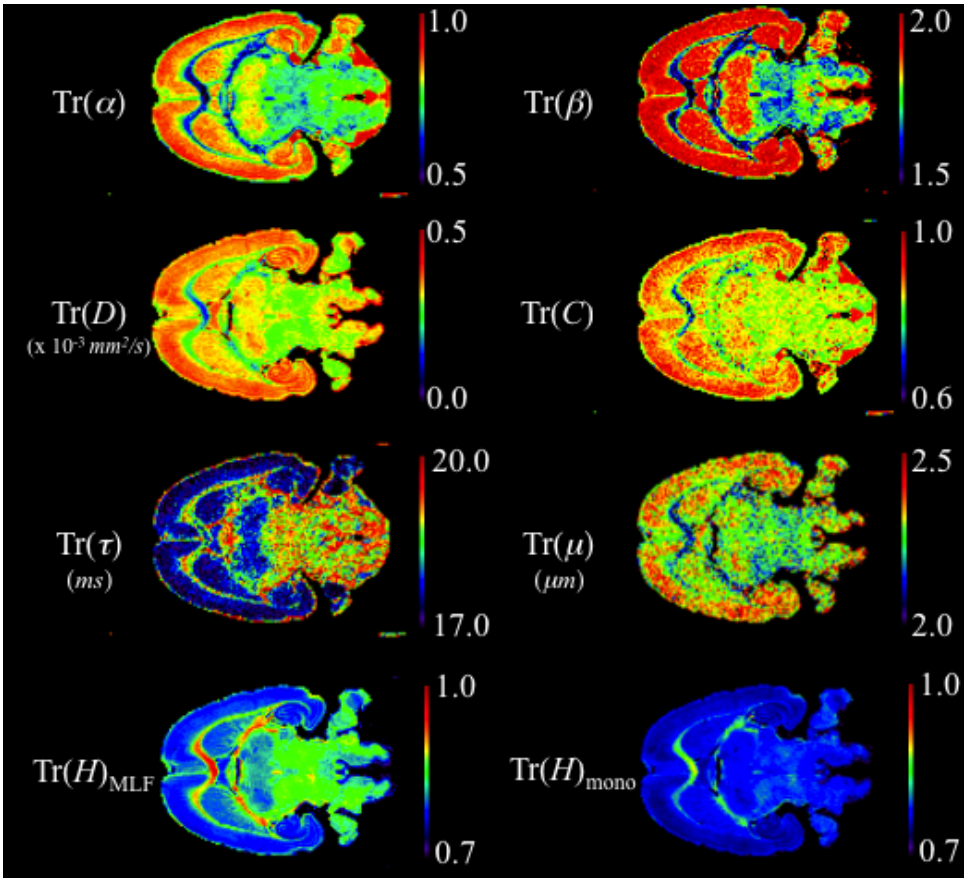

Figure 17. Trace maps of a healthy 90 day old brain in the fixed Δ experiment.

Surprisingly, the Str and the Cor ROIs of the 25 day group showed more anomalous diffusion features compared to the 90 day group (Table V and Table VI). The trace values of α, C, and D increased from the 25 day to the 90 day group, which was reflected as a decrease in $Tr(H)$. The anisotropic features of the MLF and entropy parameters did not change between the adolescent and adult samples, except for, perhaps, a slight decrease in $FA(H)$ for the 90 day group.

TABLE III

MEAN AND STD (SIGNIFICANT DIFFERENCE IN MEANS INDICATED BY P) FOR THE MLF AND ENTROPY PARAMETERS IN THE CCC ROI OF (3) HEALTHY 25 DAY AND (3) 90 DAY RATS FOR THE FIXED Δ EXPERIMENT.

	25 Day	90 Day	p
Tr($\boldsymbol{\alpha}$)	0.61 ± 0.05	0.54 ± 0.07	< 0.001
Tr($\boldsymbol{\beta}$)	1.62 ± 0.07	1.50 ± 0.13	< 0.001
Tr($\mathbf{H}$)	0.90 ± 0.02	0.94 ± 0.02	< 0.001
Tr($\mathbf{C}$)	0.76 ± 0.06	0.74 ± 0.09	0.185
Tr($\mathbf{D}$) ($\times 10^{-3} mm^2/s$)	0.22 ± 0.04	0.17 ± 0.04	< 0.001
Tr($\boldsymbol{\tau}$) (ms)	18.51 ± 0.47	17.78 ± 1.24	0.001
Tr($\boldsymbol{\mu}$) (μm)	2.13 ± 0.10	2.02 ± 0.40	0.112
FA($\boldsymbol{\alpha}$)	0.20 ± 0.09	0.36 ± 0.10	< 0.001
FA($\boldsymbol{\beta}$)	0.11 ± 0.04	0.14 ± 0.05	0.001
FA($\mathbf{H}$)	0.06 ± 0.01	0.05 ± 0.02	0.208
FA($\mathbf{C}$)	0.21 ± 0.11	0.38 ± 0.12	< 0.001
FA($\mathbf{D}$)	0.48 ± 0.16	0.56 ± 0.15	0.012
FA($\boldsymbol{\tau}$)	0.07 ± 0.02	0.12 ± 0.13	0.015
FA($\boldsymbol{\mu}$)	0.14 ± 0.06	0.19 ± 0.14	0.031

TABLE IV

MEAN AND STD (SIGNIFICANT DIFFERENCE IN MEANS INDICATED BY P) FOR THE MLF AND ENTROPY PARAMETERS IN THE LCC ROI OF (3) HEALTHY 25 DAY AND (3) 90 DAY RATS FOR THE FIXED Δ EXPERIMENT.

	25 Day	90 Day	p
Tr($\boldsymbol{\alpha}$)	0.69 ± 0.03	0.61 ± 0.04	< 0.001
Tr($\boldsymbol{\beta}$)	1.68 ± 0.08	1.56 ± 0.06	< 0.001
Tr($\mathbf{H}$)	0.87 ± 0.02	0.89 ± 0.02	< 0.001
Tr($\mathbf{C}$)	0.82 ± 0.02	0.79 ± 0.06	0.017
Tr($\mathbf{D}$) ($\times 10^{-3} mm^2/s$)	0.27 ± 0.03	0.25 ± 0.04	0.044
Tr($\boldsymbol{\tau}$) (ms)	18.81 ± 0.34	18.79 ± 0.40	0.778
Tr($\boldsymbol{\mu}$) (μm)	2.17 ± 0.06	2.23 ± 0.16	0.025
FA($\boldsymbol{\alpha}$)	0.08 ± 0.04	0.18 ± 0.07	< 0.001
FA($\boldsymbol{\beta}$)	0.08 ± 0.03	0.11 ± 0.03	< 0.001
FA($\mathbf{H}$)	0.05 ± 0.01	0.06 ± 0.02	0.003
FA($\mathbf{C}$)	0.11 ± 0.03	0.19 ± 0.10	< 0.001
FA($\mathbf{D}$)	0.34 ± 0.09	0.42 ± 0.12	0.002
FA($\boldsymbol{\tau}$)	0.07 ± 0.02	0.07 ± 0.02	0.808
FA($\boldsymbol{\mu}$)	0.11 ± 0.05	0.15 ± 0.06	0.009

Figure 18 and Figure 19 show the DEC and FA maps for an axial slice through a 25 day and 90 day sample, respectively. In the DEC maps, it is apparent that $v_3(\alpha)$ and $v_3(C)$ (i.e., the eigenvector associated with smallest eigenvalue) are approximately aligned orthogonal to $v_1(D)$ (i.e., the eigenvector associated with the principal direction of diffusivity), indicating diffusion is more anomalous perpendicular to the fiber tract orientation. This relationship appears to become stronger in coherence going from the 25 day to the 90 day groups. For $v_3(\beta)$, similar behavior is found, albeit with less coherence as $FA(\beta)$ is modulated with a smaller amplitude. In comparison, it is clear that $v_1(H)$ (i.e. the eigenvector associated with

TABLE V

MEAN AND STD (SIGNIFICANT DIFFERENCE IN MEANS INDICATED BY P) FOR THE MLF AND ENTROPY PARAMETERS IN THE STR ROI OF (3) HEALTHY 25 DAY AND (3) 90 DAY RATS FOR THE FIXED Δ EXPERIMENT.

	25 Day	90 Day	p
Tr($\boldsymbol{\alpha}$)	0.83 ± 0.01	0.88 ± 0.02	< 0.001
Tr($\boldsymbol{\beta}$)	1.93 ± 0.02	1.94 ± 0.04	0.341
Tr($\mathbf{H}$)	0.80 ± 0.01	0.77 ± 0.02	< 0.001
Tr($\mathbf{C}$)	0.86 ± 0.02	0.91 ± 0.03	< 0.001
Tr($\mathbf{D}$) ($\times 10^{-3} mm^2/s$)	0.33 ± 0.01	0.36 ± 0.02	< 0.001
Tr($\boldsymbol{\tau}$) (ms)	17.54 ± 0.30	17.48 ± 1.06	0.606
Tr($\boldsymbol{\mu}$) (μm)	2.28 ± 0.06	2.32 ± 0.11	0.006
FA($\boldsymbol{\alpha}$)	0.05 ± 0.02	0.06 ± 0.02	0.097
FA($\boldsymbol{\beta}$)	0.05 ± 0.02	0.05 ± 0.02	0.328
FA($\mathbf{H}$)	0.03 ± 0.01	0.04 ± 0.02	0.004
FA($\mathbf{C}$)	0.07 ± 0.03	0.09 ± 0.05	0.001
FA($\mathbf{D}$)	0.23 ± 0.06	0.23 ± 0.06	0.713
FA($\boldsymbol{\tau}$)	0.07 ± 0.02	0.09 ± 0.15	0.136
FA($\boldsymbol{\mu}$)	0.07 ± 0.03	0.12 ± 0.09	< 0.151

the largest entropy eigenvalue) is aligned approximately orthogonal to $v_1(D)$ and shows strong geometrical coherence, albeit modulated by a small range of values of $FA(H)$, which did not exceed ~ 0.1 in the most anisotropic ROIs.

5.2.2 Fixed q experiment

For visual comparison in the fixed q experiment, the trace maps of the MLF parameters, entropy of the diffusion decay as modeled by the MLF (H_{MLF}), entropy of the diffusion decay as modeled by the mono-exponential (H_{mono}) are shown for a 25 and 90 day sample in Figure 20 and Figure 21, respectively. As shown in Table VII, from the adolescent to the adult neural

TABLE VI

MEAN AND STD (SIGNIFICANT DIFFERENCE IN MEANS INDICATED BY P) FOR THE MLF AND ENTROPY PARAMETERS IN THE COR ROI OF (3) HEALTHY 25 DAY AND (3) 90 DAY RATS FOR THE FIXED Δ EXPERIMENT.

	25 Day	90 Day	p
Tr($\boldsymbol{\alpha}$)	0.83 ± 0.01	0.87 ± 0.02	< 0.001
Tr($\boldsymbol{\beta}$)	1.92 ± 0.03	1.95 ± 0.03	< 0.001
Tr($\mathbf{H}$)	0.78 ± 0.01	0.76 ± 0.02	< 0.001
Tr($\mathbf{C}$)	0.86 ± 0.01	0.89 ± 0.02	< 0.001
Tr($\mathbf{D}$) ($\times 10^{-3} mm^2/s$)	0.38 ± 0.01	0.41 ± 0.03	< 0.001
Tr($\boldsymbol{\tau}$) (ms)	17.92 ± 0.23	17.55 ± 0.28	< 0.001
Tr($\boldsymbol{\mu}$) (μm)	2.36 ± 0.05	2.38 ± 0.13	0.337
FA($\boldsymbol{\alpha}$)	0.06 ± 0.02	0.07 ± 0.02	0.656
FA($\boldsymbol{\beta}$)	0.06 ± 0.02	0.04 ± 0.03	0.009
FA($\mathbf{H}$)	0.05 ± 0.01	0.04 ± 0.01	< 0.001
FA($\mathbf{C}$)	0.06 ± 0.03	0.07 ± 0.04	0.128
FA($\mathbf{D}$)	0.21 ± 0.04	0.19 ± 0.06	0.100
FA($\boldsymbol{\tau}$)	0.06 ± 0.02	0.07 ± 0.03	0.523
FA($\boldsymbol{\mu}$)	0.07 ± 0.02	0.12 ± 0.08	< 0.391

tissue in the CCC, the trace values for α, C and D had significant decrease, which is reflected in an increase in the entropy, H. The mean values of $FA(D)$ increased ($\sim 35\%$) with age, however there is considerable overlap in the standard deviation between the groups. In general, for all of the ROIs, the magnitude of FA of the anomalous parameters (α, β, C) was reduced in the fixed q experiment compared to the fixed Δ experiment. Interestingly, though, is that $FA(\tau)$ in the fixed q experiment was significantly higher than when estimated in the fixed Δ experiment. For, the CCC, the mean of $FA(\tau)$ increased from ~ 0.50 to ~ 0.75 with age, however there is considerable overlap in the standard deviations, just as is the case with $FA(D)$. The magnitude

of $FA(H)$ did not change between the fixed Δ and fixed q experiments. There was no change in $FA(H)$ between the two groups. It should be noted that within each group, $FA(D)$ was the most anisotropic parameter.

In the LCC (Table VIII), again, the trace values for α, C and D had significant decrease, which is reflected in an increase in the entropy, $Tr(H)$ from the 25 day to the 90 day samples. In general, fractional anisotropy estimations of the MLF and entropy parameters did not distinguish between the adolescent and adult groups, however, there was a small increase in $FA(\alpha)$ associated with adult neural tissue.

TABLE VII

MEAN AND STD (SIGNIFICANT DIFFERENCE IN MEANS INDICATED BY P) FOR THE MLF AND ENTROPY PARAMETERS IN THE CCC ROI OF (3) HEALTHY 25 DAY AND (3) 90 DAY RATS FOR THE FIXED Q EXPERIMENT.

	25 Day	90 Day	p
Tr($\boldsymbol{\alpha}$)	0.88 ± 0.02	0.84 ± 0.02	< 0.001
Tr($\boldsymbol{\beta}$)	1.96 ± 0.05	1.97 ± 0.03	0.267
Tr($\mathbf{H}$)	0.85 ± 0.01	0.89 ± 0.02	< 0.001
Tr($\mathbf{C}$)	0.90 ± 0.02	0.85 ± 0.02	< 0.001
Tr($\mathbf{D}$) ($\times 10^{-3} mm^2/s$)	0.22 ± 0.03	0.18 ± 0.04	< 0.001
Tr($\boldsymbol{\tau}$) (ms)	11.98 ± 5.21	23.51 ± 11.92	< 0.001
Tr($\boldsymbol{\mu}$) (μm)	2.12 ± 0.02	2.23 ± 0.32	0.110
FA($\boldsymbol{\alpha}$)	0.06 ± 0.02	0.09 ± 0.04	0.002
FA($\boldsymbol{\beta}$)	0.05 ± 0.04	0.03 ± 0.04	0.400
FA($\mathbf{H}$)	0.06 ± 0.02	0.06 ± 0.02	0.398
FA($\mathbf{C}$)	0.08 ± 0.04	0.11 ± 0.05	0.073
FA($\mathbf{D}$)	0.55 ± 0.18	0.75 ± 0.10	0.001
FA($\boldsymbol{\tau}$)	0.49 ± 0.35	0.75 ± 0.33	0.030
FA($\boldsymbol{\mu}$)	0.02 ± 0.01	0.11 ± 0.10	0.024

TABLE VIII

MEAN AND STD (SIGNIFICANT DIFFERENCE IN MEANS INDICATED BY P) FOR THE MLF AND ENTROPY PARAMETERS IN THE LCC ROI OF (3) HEALTHY 25 DAY AND (3) 90 DAY RATS FOR THE FIXED Q EXPERIMENT.

	25 Day	90 Day	p
Tr($\boldsymbol{\alpha}$)	0.89 ± 0.01	0.83 ± 0.02	< 0.001
Tr($\boldsymbol{\beta}$)	1.97 ± 0.03	1.99 ± 0.02	0.014
Tr($\mathbf{H}$)	0.80 ± 0.01	0.84 ± 0.02	< 0.001
Tr($\mathbf{C}$)	0.90 ± 0.02	0.84 ± 0.02	< 0.001
Tr($\mathbf{D}$) ($\times 10^{-3} mm^2/s$)	0.29 ± 0.02	0.25 ± 0.04	< 0.001
Tr($\boldsymbol{\tau}$) (ms)	8.44 ± 0.63	11.37 ± 3.65	< 0.001
Tr($\boldsymbol{\mu}$) (μm)	2.11 ± 0.01	2.12 ± 0.02	0.126
FA($\boldsymbol{\alpha}$)	0.04 ± 0.01	0.06 ± 0.02	< 0.001
FA($\boldsymbol{\beta}$)	0.04 ± 0.03	0.01 ± 0.03	0.017
FA($\mathbf{H}$)	0.07 ± 0.01	0.06 ± 0.01	0.021
FA($\mathbf{C}$)	0.07 ± 0.04	0.06 ± 0.03	0.779
FA($\mathbf{D}$)	0.40 ± 0.11	0.38 ± 0.09	0.582
FA($\boldsymbol{\tau}$)	0.24 ± 0.15	0.34 ± 0.23	0.064
FA($\boldsymbol{\mu}$)	0.02 ± 0.01	0.02 ± 0.01	0.685

Surprisingly, for the fixed q experiment, the Str and the Cor ROIs of the 25 day group showed more anomalous diffusion features compared to the 90 day group (Table IX and Table X), which is similar to findings in the fixed Δ experiment. The trace values of α, C increased from the 25 day to the 90 day group, which was reflected as a decrease in $Tr(H)$. The anisotropic features of the MLF and entropy parameters did not change between the adolescent and adult samples, and should be highlighted the change in $Tr(D)$ and $FA(D)$ were not able to consistently distinguish between the 25 and 90 groups.

TABLE IX

MEAN AND STD (SIGNIFICANT DIFFERENCE IN MEANS INDICATED BY P) FOR THE MLF AND ENTROPY PARAMETERS IN THE STR ROI OF (3) HEALTHY 25 DAY AND (3) 90 DAY RATS FOR THE FIXED Q EXPERIMENT.

	25 Day	90 Day	p
Tr($\boldsymbol{\alpha}$)	0.92 ± 0.01	0.94 ± 0.01	< 0.001
Tr($\boldsymbol{\beta}$)	1.98 ± 0.02	1.95 ± 0.06	0.004
Tr($\mathbf{H}$)	0.76 ± 0.01	0.74 ± 0.01	< 0.001
Tr($\mathbf{C}$)	0.93 ± 0.02	0.97 ± 0.05	< 0.001
Tr($\mathbf{D}$) ($\times 10^{-3} mm^2/s$)	0.33 ± 0.02	0.34 ± 0.02	0.005
Tr($\boldsymbol{\tau}$) (ms)	8.05 ± 0.95	7.49 ± 1.89	0.102
Tr($\boldsymbol{\mu}$) (μm)	2.09 ± 0.02	2.07 ± 0.03	< 0.001
FA($\boldsymbol{\alpha}$)	0.03 ± 0.01	0.02 ± 0.01	0.022
FA($\boldsymbol{\beta}$)	0.02 ± 0.01	0.05 ± 0.04	0.008
FA($\mathbf{H}$)	0.04 ± 0.01	0.03 ± 0.01	0.049
FA($\mathbf{C}$)	0.05 ± 0.04	0.10 ± 0.08	0.007
FA($\mathbf{D}$)	0.22 ± 0.06	0.20 ± 0.05	0.237
FA($\boldsymbol{\tau}$)	0.22 ± 0.14	0.29 ± 0.23	0.093
FA($\boldsymbol{\mu}$)	0.02 ± 0.01	0.02 ± 0.01	0.605

Figure 22 and Figure 23 show the DEC and FA maps for an axial slice through a 25 day and 90 day sample, respectively. In general, for the fixed q experiment, the DEC and FA maps show less contrast and anisotropy compared to the fixed Δ experiment. In the CCC, although modulated by small range of $FA(\alpha)$ (< 0.1), $v_3(\alpha)$ (i.e., the eigenvector associated with smallest eigenvalue) are approximately aligned parallel to $v_1(D)$ (i.e., the eigenvector associated with the principal direction of diffusivity). This relationship appears to become stronger in coherence going from the 25 day to the 90 day groups. Although this geometrical relationship is different from that which was found for $v_3(\alpha)$ and $v_1(D)$ in the fixed Δ experiment, it should

be considered that the dynamic range in α estimations was small. Additionally, the DEC and FA maps for β and C show little to no contrast with tissue structure. In comparison, it is clear that $v_1(H)$ (i.e. the eigenvector associated with the largest entropy eigenvalue) is aligned approximately orthogonal to $v_1(D)$ and shows strong geometrical coherence, albeit modulated by a small range of values of $FA(H)$, which did not exceed ~ 0.1 in the most anisotropic ROIs.

TABLE X

MEAN AND STD (SIGNIFICANT DIFFERENCE IN MEANS INDICATED BY P) FOR THE MLF AND ENTROPY PARAMETERS IN THE COR ROI OF (3) HEALTHY 25 DAY AND (3) 90 DAY RATS FOR THE FIXED Q EXPERIMENT.

	25 Day	90 Day	p
Tr($\boldsymbol{\alpha}$)	0.92 ± 0.01	0.94 ± 0.01	< 0.001
Tr($\boldsymbol{\beta}$)	1.97 ± 0.04	1.96 ± 0.04	0.134
Tr($\mathbf{H}$)	0.74 ± 0.01	0.73 ± 0.01	< 0.001
Tr($\mathbf{C}$)	0.94 ± 0.03	0.96 ± 0.03	0.018
Tr($\mathbf{D}$) ($\times 10^{-3} mm^2/s$)	0.37 ± 0.02	0.37 ± 0.03	0.759
Tr($\boldsymbol{\tau}$) (ms)	7.17 ± 0.49	6.78 ± 0.67	0.013
Tr($\boldsymbol{\mu}$) (μm)	2.09 ± 0.02	2.07 ± 0.02	< 0.001
FA($\boldsymbol{\alpha}$)	0.03 ± 0.01	0.02 ± 0.01	0.022
FA($\boldsymbol{\beta}$)	0.04 ± 0.03	0.05 ± 0.04	0.509
FA($\mathbf{H}$)	0.05 ± 0.02	0.04 ± 0.01	0.001
FA($\mathbf{C}$)	0.08 ± 0.07	0.08 ± 0.06	0.952
FA($\mathbf{D}$)	0.18 ± 0.03	0.21 ± 0.04	0.015
FA($\boldsymbol{\tau}$)	0.20 ± 0.11	0.24 ± 0.12	0.182
FA($\boldsymbol{\mu}$)	0.02 ± 0.01	0.02 ± 0.01	0.382

In the context of CTRW theory, the MLF, and entropy, diffusion in the WM in the adult neural tissue compared to the WM in the adolescent neural tissue, both for the fixed Δ and fixed q experiments. Additionally, it appears that the anomalous measurements are more anisotropic in the adult neural tissue, particularly for the CC, as described by $FA(\alpha)$ and $FA(C)$ (Table III and Table IV) for the fixed Δ experiment. In general, compared to the fixed q experiment, the fixed Δ experiment produced more anomalous diffusion features as represented by lower α, β values and higher H values for the ROIs. This finding is reasonable as the fixed Δ experiment samples numerous increasing q values (for higher spatial resolution) to acquire the signal decay, whereas the fixed q experiment samples numerous increasing Δ values to acquire the signal decay. At long Δ values, there is more time for the water particles to interact with the diffusion environment and spatial averaging occurs, which is reflected in the $Tr(\beta)$ maps in both Figure 20 and Figure 21 where $\beta \to 2$, indicating a Gaussian statistics on the jump length distributions. Whereas, in the fixed Δ experiment, from the q-space perspective, the diffusion propagator is estimated from numerous measurements in the inverse-spatial (Fourier) domain such that the resolution of the experiment is increasingly magnified and, perhaps is a more accurate measurement of the actual diffusion dynamics, following (4; 49).

The surprising finding that the deep GM and cortical tissue was more anomalous and sub-diffusive in the 25 day group compared to the 90 day group was verified both in the fixed Δ and fixed q experiments. Lower values for α and C while higher values of H indicate that the Str and Cor are more heterogeneous at a young age and, upon adulthood, these structures become more homogeneous. This would indicate that healthy aging in neural tissue is not only limited

to increased anisotropy and heterogeneity in the WM, but also a decrease in heterogeneity in the GM, such that complexity is exchanged from the GM to the WM. A possible biological mechanism for this could be the migration of astrocytes, oligodendrocytes, glia in GM to the WM during neural development, contributing to increased heterogeneity.

With regard to the directional orientation of the MLF parameters, it is clear, particularly with α and C, that the eigenvectors associated with the smallest eigenvalues are not aligned with the principal direction of diffusivity as given by D. In the fixed Δ experiment, the most anomalous diffusion was found to be perpendicular to the orientation of the WM fiber tract bundle direction, that is, in the direction for which the highest entropy estimations were also found. From an experimental setup perspective, this relationship is reasonable to intuit as the fixed Δ experiment probes an increasingly greater spatial resolution as the diffusion encoding gradient strengths are amplified, such that the appearance of tissue microstructure orthogonal to the principal WM fiber direction is more sub-diffusive due to the hinderances of the cell walls, membranes, and wrapped layers of myelinated sheathing. In contrast, for the direction parallel to the fiber orientation, although the diffusion process is anomalous, it is not as anomalous as the perpendicular case due to the less hindered diffusion at lower spatial resolutions. For the fixed q experiment, albeit scaled be a small dynamic range of FA (i.e., < 0.1)and less directional coherence, the smallest estimations for α appear to align parallel to the principal direction of diffusivity. Though this relationship may, at first, appear counterintuitive, the experimental setup of the fixed q, variable Δ experiment provides insight. That is, as the values for the mixing time, Δ, are increased in the b-value array. Perpendicular to the fiber direction, the distribution

of distances traveled by the water particles is more normal, as on one spatial resolution (i.e. q-value), the hinderances are homogenous with respect to time. Parallel to the fiber direction, the distribution of distances traveled by the water particles is less normal, as on one spatial resolution, the hinderances are more heterogeneous when considering that some water particles are trapped and some are free to jump as is indicated by the high resolution micrographs of the corpus callosum in (45).

It is clear, regardless of the experimental setup, that D is the most anisotropic diffusion parameter, however it is not necessarily the most sensitive indicator of tissue type or change in tissue microstructure in healthy aging. The anomalous measurements of α, β, and C showed anisotropic characteristics that were scaled on a smaller dynamic range, but provided better separation of the WM tissue structural morphology, particularly in the corpus callosum. However, it should be highlighted that the trace values of the MLF parameters performed well in being able to distinguish between tissue types and age groups. Hence, in order to classify tissue microstructure, it may not be necessary to build anisotropic tensor constructs, and, perhaps one or three directions are sufficient to determine an isotropic estimation anomalous diffusion in an ROI. Regardless, it is clear in Figure 16, Figure 17, Figure 20, and Figure 21, that additional tissue information is shed when comparing the decay signal captured by the MLF ($Tr(H)_{MLF}$) in comparison to a mono-exponential decay ($Tr(H)_{mono}$).

5.3 Conclusions

In this study, the one-dimensional anomalous diffusion model represented by the MLF and entropy were extended to a three-dimensional case utilizing tensor constructs. This analysis

was performed on healthy adolescent and adult rat tissue to investigate the potential changes in isotropic and anisotropic features of anomalous diffusion in both WM and GM. Fixed Δ and fixed q experiments were performed and it was found that, in general, the fixed Δ protocol produced more anisotropic and anomalous measurements for the same ROIs compared to the fixed q experiment. For the fixed Δ protocol, α, β, and C were anisotropic and more sensitive to healthy aging than the classical diffusion coefficient, D. Additionally, the orientation of these anomalous measures were found to be perpendicular to the principal direction of diffusivity. The entropy, H, provided excellent tissue contrast, ROI separation, age group segmentation, and was in agreement with the directional dependence of the MLF parameters. For the WM, the tissue heterogeneity increased with age marked as a decrease in the MLF parameters and an increase in entropy. Conversely, and surprisingly, for the GM, the tissue heterogeneity decreased with age as marked as an increase in MLF parameters and a decrease in entropy. These results indicate that the multi-b-value data acquisition strategy and anomalous diffusion modeling are promising techniques to produce biomarkers for neural tissue microstructure *in vivo* for humans on a clinical scanner, which is addressed in the following chapter.

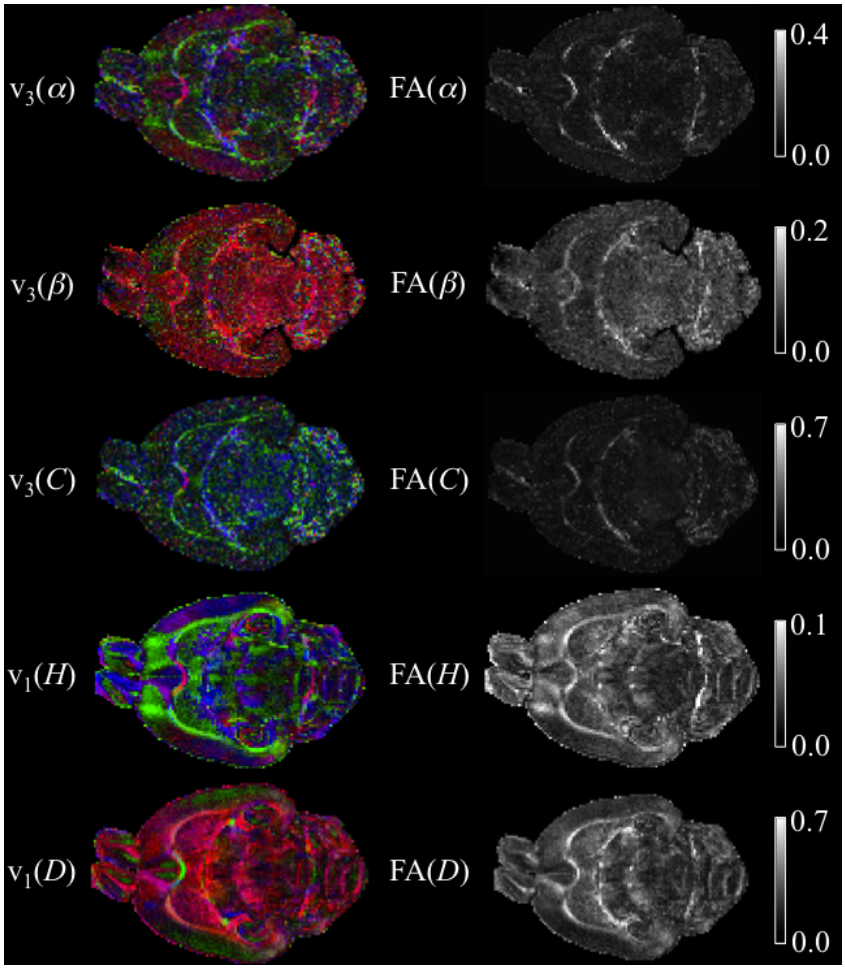

Figure 18. DEC and FA maps of a healthy 25 day old brain in the fixed Δ experiment.

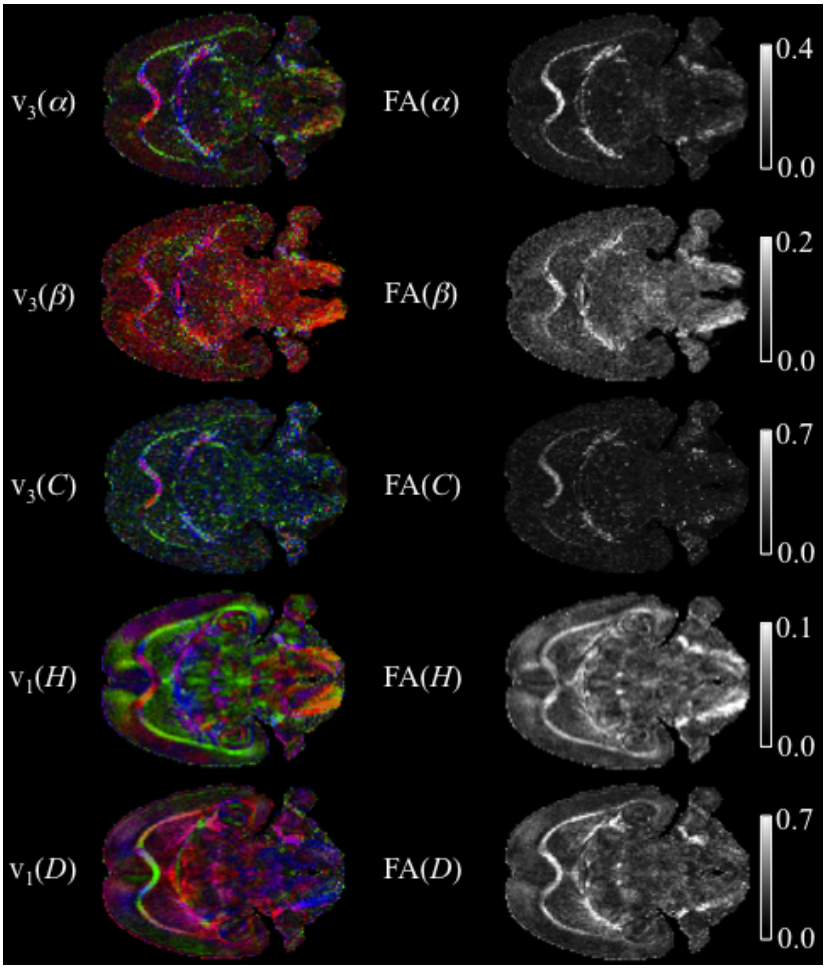

Figure 19. DEC and FA maps of a healthy 90 day old brain in the fixed Δ experiment.

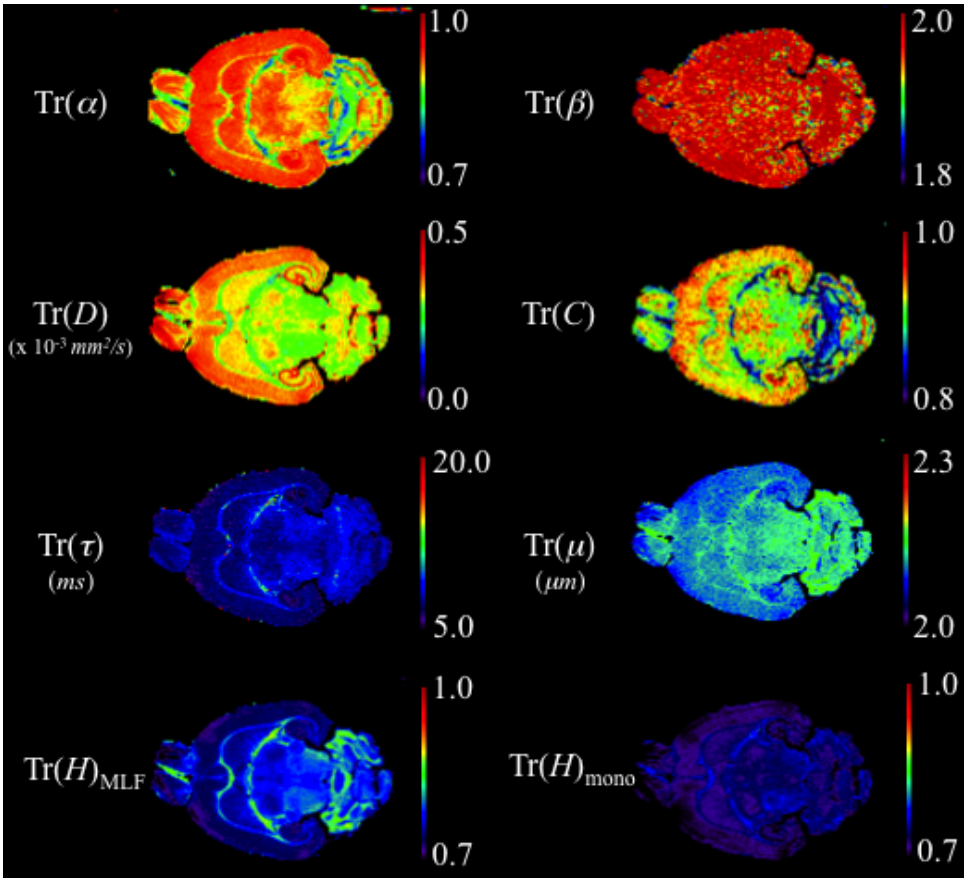

Figure 20. Trace maps of a healthy 25 day old brain in the fixed q experiment.

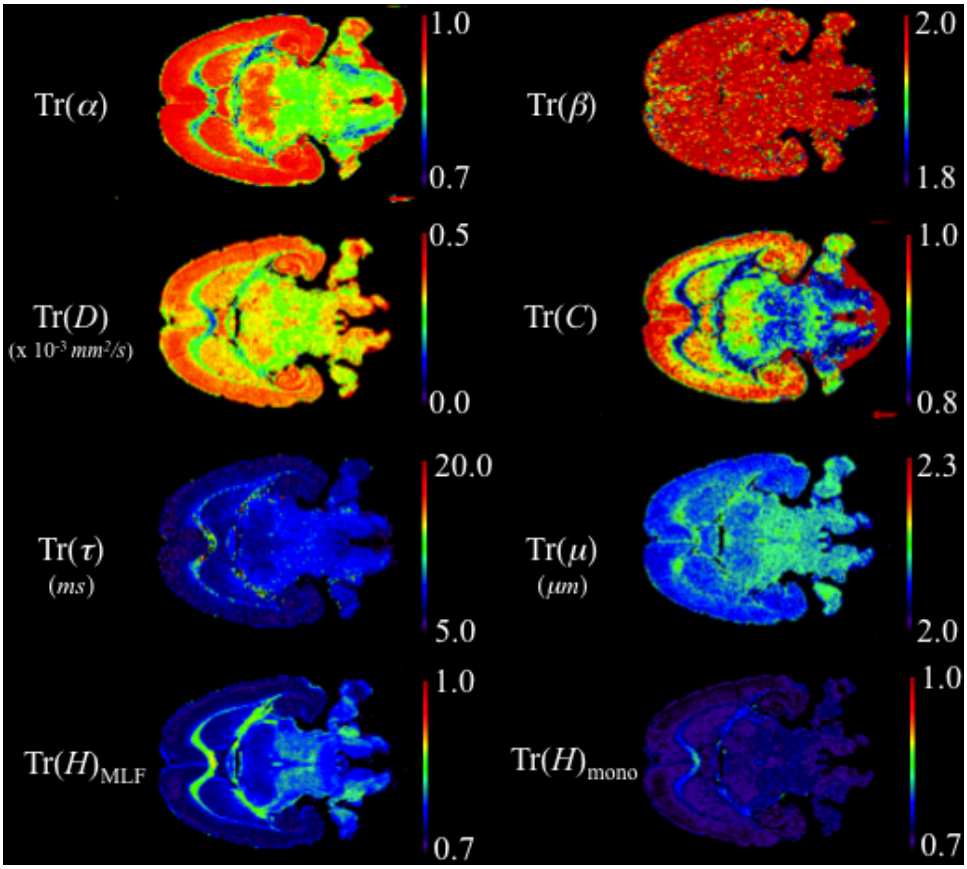

Figure 21. Trace maps of a healthy 90 day old brain in the fixed q experiment.

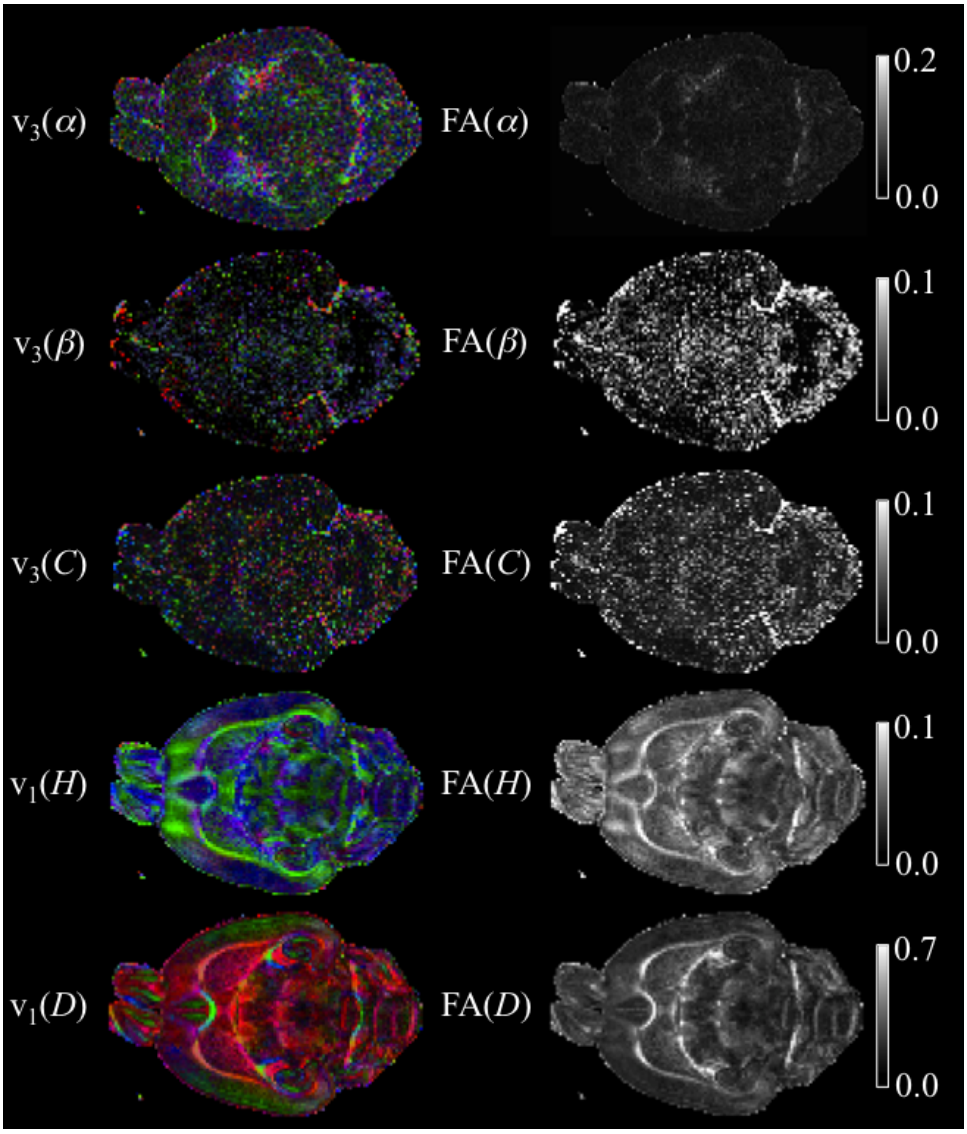

Figure 22. DEC and FA maps of a healthy 25 day old brain in the fixed q experiment.

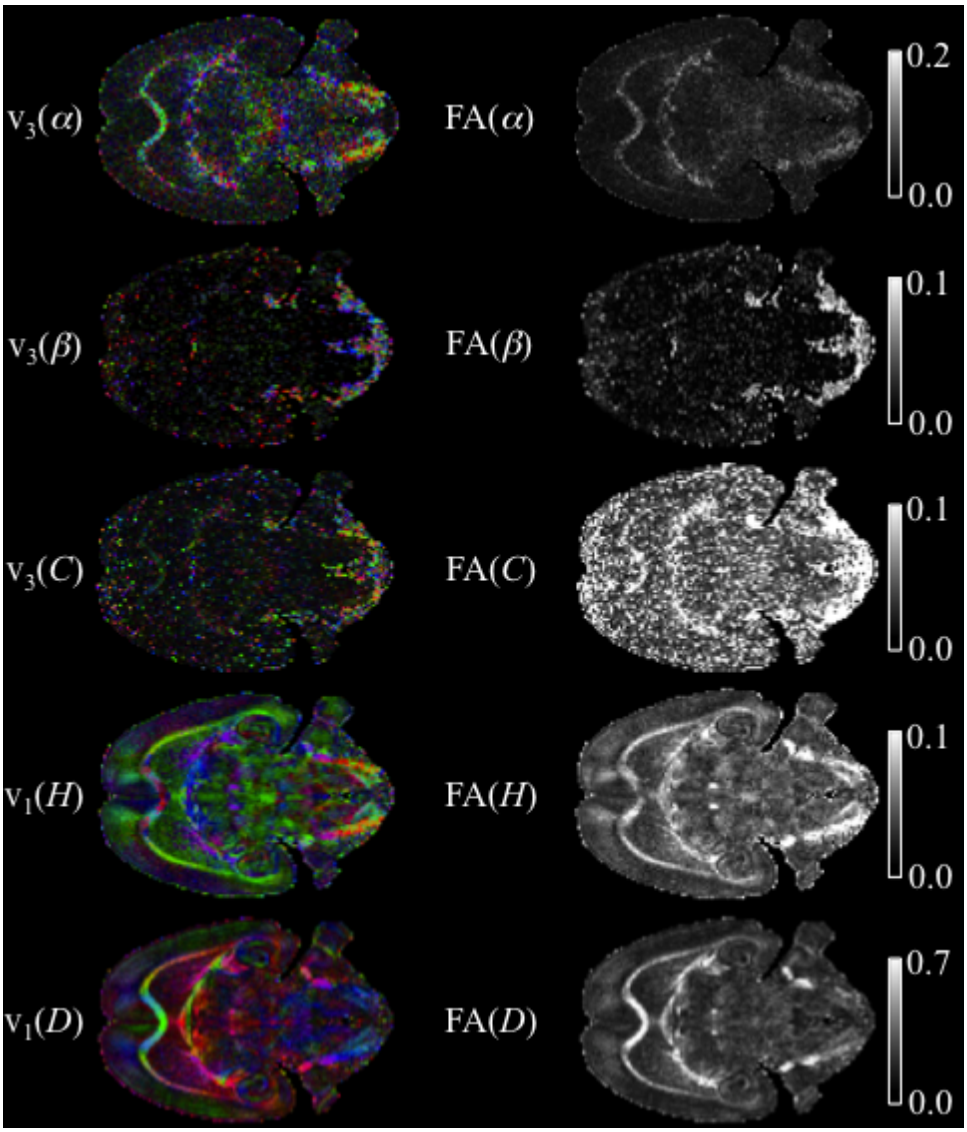

Figure 23. DEC and FA maps of a healthy 90 day old brain in the fixed q experiment.

CHAPTER 6

CLINICAL DIFFUSION TENSOR IMAGING OF RANDOM WALKS AND ENTROPY IN HEALTHY HUMAN NEURAL TISSUE

6.1 Methods

Moving from the high field imaging spectrometer to the clinical MRI scanner at 3T, SE-EPI diffusion weighted protocols were applied to healthy volunteers at SGUL (London, UK) with multi-b-value acquisitions up to 5,000 s/mm^2 and, in addition, HCP data were utilized to demonstrate feasibility of the MLF and entropy parameters to provide tissue contrast at multi-$b-$value acquisitions up to 3,000 s/mm^2.

At SGUL, for the 12 direction low resolution aDTI protocol, images were acquired from nine healthy young male subjects (30 ± 3 years) on a 3T Philips Achieva Dual TX MR scanning system (Philips Healthcare, Best, Netherlands) at SGUL equipped with gradients up to 80mTm^{-1} using a 32 channel head coil. Written consent was obtained from each subject prior to the procedure. For each subject, T1-weighted 3D volume images were acquired using a TFE sequence (TE=3700ms, TR=8200ms, flip angle 8°, 160 sagittal slices, FOV 240mm×240mm giving isotropic 1mm^3 voxel resolution). DWIs were acquired using a diffusion-sensitized SE-EPI sequence using the enhanced gradient mode (80mTm^{-1} at a slew rate of 100mTm^{-1}ms^{-1}) after a second order shim. Fat suppression was achieved using SPIR and SSGR. Scan parameters were as follows: TE = 82ms, TR = 10500ms, δ = 27.5ms, Δ = 40.2ms, FOV

210mm×210mm with 33 3mm thick slices giving 3mm^3 isotropic voxel resolution, SENSE factor 2 and half scan factor 0.745. DWIs were acquired in 12 non-collinear directions at 7 b-values The 12 gradient directions were [-0.049091 -0.911723 0.407862; -0.206148 0.498342 0.842115; 0.738888 -0.614058 0.277448; 0.468899 0.790365 0.394281; -0.956810 -0.102862 -0.271907; -0.444925 -0.283931 0.849367; -0.928648 -0.068217 0.364635; 0.175416 -0.967668 -0.181237; 0.534255 0.226736 0.814348; 0.730370 -0.676931 -0.091239; 0.730584 -0.580541 -0.359469; 0.322146 -0.471761 0.820770]. The b-values were separated approximately log-linearly with greater averaging at higher b-values to increase signal to noise ratio (SNR). b-value(number of acquisitions): 0(8), 90(2), 200(2), 450(2), 1000(2), 2250(4), 5000(8).

Additionally, at SGUL, for the 3 direction (Tr) high resolution aDWI protocol, images were acquired from one healthy young male subject (33 years) on a 3T Philips Achieva Dual TX MR scanning system (Philips Healthcare, Best, Netherlands) at SGUL equipped with gradients up to 80mTm^{-1} using a 32 channel head coil. Written consent was obtained from the subject prior to the procedure. Scan parameters were as follows: TE = 78ms, TR = 8000ms, δ = 18.5ms, Δ = 43.6ms, FOV 140mm×140mm for a 5mm thick slice giving 1×1×5mm^3 voxel resolution which were reconstructed to 0.6×0.6×5mm^3. DWIs were acquired in 3 orthogonal directions at 10 different b-values with greater averaging at higher b-values to increase SNR. b-value(number of acquisitions): 0(2), 150(2), 300(2), 450(2), 600(4), 750(6), 1000(4), 2000(4), 3000(4), 3500(8).

Finally, HCP dMRI and T1 data were utilized from eight subjects using the protocol described in(50). The T1 data were collected with the following parameters: TR=2400 ms, TE=2.14 ms, TI=1000 ms, Flip Angle = 8 deg, FOV=224×224, voxel size = 0.7 mm isotropic.

The SE-EPI diffusion data were collected with the following parameters: TR=5520 ms, TE 89.5 ms, flip angle 78 deg, refocusing flip angle 160 deg, FOV=210x180 mm (RO x PE), matrix=168x144 (RO x PE), slice thickness=1.25 mm, 111 slices, 1.25 mm isotropic voxels, Multiband factor 3 Echo spacing=0.78 ms, BW=1488 Hz/Px, Phase partial Fourier=6/8, b-values 1000, 2000, and 3000 s/mm^2.

6.2 Data Processing

All low and high resolution DWIs acquired at SGUL were corrected for subject motion and eddy current distortion in SPM12 (Wellcome Department of Cognitive Neurology, Institute of Neurology, London, UK, `http://www.fil.ion.ac.uk/spm12`) using the technique described in (19).

In the low resolution SGUL data set, for each diffusion weighted gradient experiment, the data were fit to the 1D MLF and entropy parameters as described in (Equation 2.13) and (Equation 2.16). In the high resolution SGUL data set, the Tr data were fit to the 1D MLF and entropy parameters as described in (Equation 2.13) and (Equation 2.16). The MLF parameters were estimated using the same methodology described in Chapter 4 and Appendix A. After the MLF parameters were determined, the characteristic decay curve for $p(q, \bar{\Delta})$ was constructed using N=1,500 increments arrayed over variable q or variable $\bar{\Delta}$ for b-values between 0 and 25,000 s/mm^2. Then, the entropy (defined in (Equation 2.16)) in the diffusion process, as modeled by the MLF, was computed as $H(q, \bar{\Delta})_{MLF}$. For comparison, using the mono-exponential model (D_m) in (Equation 2.12), a characteristic decay curve of N = 1,500 increments arrayed over b-values between 0 and 10,000 s/mm^2 was constructed. Then, for

the SGUL low resolution data, using (Equation 2.17), Gaussian ellipsoids were fitted to obtain tensor maps for each parameter (i.e. $\mathbf{D}$, $\boldsymbol{\alpha}$, $\boldsymbol{\beta}$, $\boldsymbol{\tau}$, $\boldsymbol{\mu}$, $\mathbf{H}$ and $\mathbf{C}$) and were diagonalized to obtain eigenvalues and eigenvectors. Rotationally invariant isotropic (Tr) and anisotropic (FA) maps were computed for each MLF parameter. Eigenvector orientation was visualized using DEC which colors eigenvector orientations red in the sinister-dexter direction, green in the anterior-posterior direction and blue in the superior-inferior direction (48). Brightness of the DEC parameter map was modulated by FA of the parameter.

As the scope of this study determine the feasibility of the MLF and entropy parameters to identify tissue features through anomalous diffusion measurements, the HCP data is used to compute high resolution isotropic MLF and entropy parameter maps and not investigate anisotropic measures. Furthermore, based on the findings in Chapter 5 on the healthy adolescent and adult neural tissue, the trace values performed well in distinguishing both tissue type as well as age group. To convert the HCP data to a format that may be readily fitted to the MLF the data was initially simplified from a multi b-value shell high angular resolution diffusion weighted acquisition to multi b-value shell trace DWIs. Diffusion weighted tensors were computed for each b-value shell (i.e. at b=1000, b=2000 and b=3000 s mm^{-2}) using (Equation 2.17). Trace DWIs were then computed by diagonalizing these tensors and computing the mean of the eigenvalues. Additionally, trace DWIs were estimated at b=300, b=550 and b=800 s mm^{-2} in the mono-exponential regime of diffusion (assuming a mono-exponential decay) in order to provide the necessary 6 b-value shell DWIs required for MLF fitting using (Equation 2.13).

For comparison of MLF parameter estimates obtained from the low resolution aDTI dataset and the HCP dataset ROIs were parcellated using FreeSurfer (https://surfer.nmr.mgh.harvard.edu/) to process the T1-weighted volume images. ROIs were chosen to include the lateral ventricles (i.e. CSF), cortical and sub-cortical gray matter and white matter anatomical locations. Mean, standard deviation, median, lower and upper quartiles were computed for each ROI across each dataset.

6.3 Results and Discussion

The trace values of MLF and entropy parameter maps showed, in general, exceptional tissue contrast between CSF, cortical GM and WM regions in the low resolution aDTI and HCP datasets (Figure 24, Table XI, Table XII). The diffusion coefficient maps for D had values for the CSF values $\sim 3.0\times10^{-3}$ mm^2/s greater than cortical GM $\sim 0.9\times10^{-3}$ mm^2/s and WM $\sim 0.8\times10^{-3}$ mm^2/s. Clear contrast was observed in α between the three tissue types with values ~ 1 in CSF (revealing a mono-exponential decay curve) and lower values in cortical GM (~ 0.8) and WM (~ 0.7) indicating increased waiting times in WM compared to cortical GM. Similar step length exponents, β were observed in CSF and GM regions which were closer to 2 (i.e. indicating normal distribution) in the HCP data. Values for β were lower in white matter (~ 1.8)indicating shorter step lengths in white matter structure. The tissue contrast in α and β maps is particularly apparent when histogram distributions are considered in terms of the minimal overlap between quartiles in Table XI and Table XII for the ROIs.

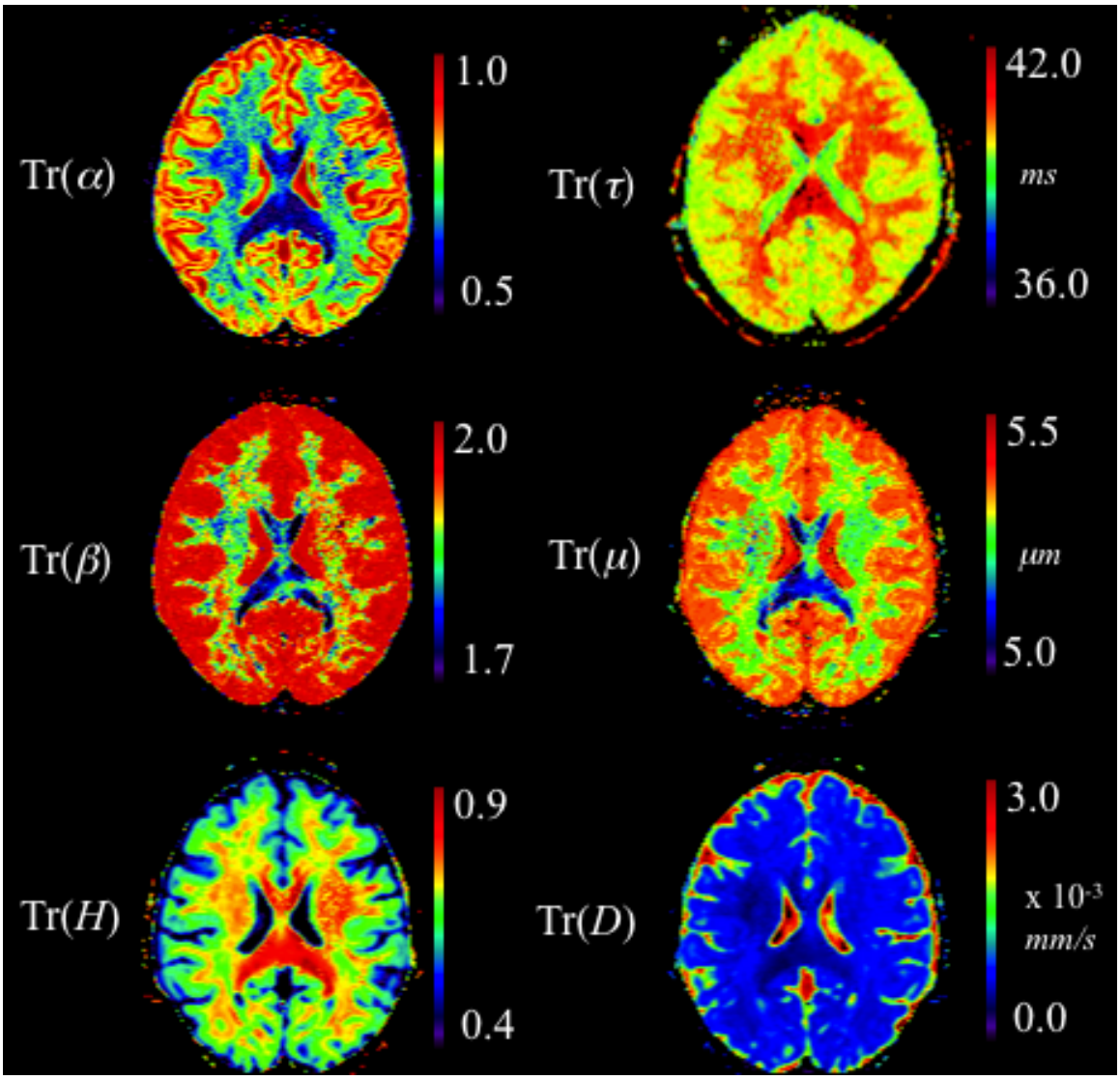

Figure 24. Tr maps of $D_{1,2}$, α, β, τ, μ, and H for a single subject from the HCP dataset.

TABLE XI

SGUL LOW RESOLUTION DATA RESULTS FOR THE CSF, CORTICAL GM, AND WM ROIS.

CSF

	Mean ± StD	LQ	Median	UQ
$Tr(\mathbf{D})(\times 10^{-3} mm^2/s)$	3.01 ± 0.32	2.41	2.76	3.21
$Tr(\boldsymbol{\alpha})$	0.88 ± 0.02	0.78	0.91	0.98
$Tr(\boldsymbol{\beta})$	1.86 ± 0.04	1.80	1.93	1.97
$Tr(\mathbf{C})$	0.94 ± 0.01	0.91	0.97	1.00
$Tr(\boldsymbol{\tau})$ (ms)	31.6 ± 0.2	31.10	31.30	31.90
$Tr(\boldsymbol{\mu})$ (μm)	5.13 ± 0.03	5.07	5.18	5.24
$Tr(\mathbf{H})$	0.3 ± 0.02	0.24	0.27	0.33

Cortical GM

	Mean ± StD	LQ	Median	UQ
$Tr(\mathbf{D})(\times 10^{-3} mm^2/s)$	1.32 ± 0.09	0.86	1.10	1.48
$Tr(\boldsymbol{\alpha})$	0.77 ± 0.01	0.70	0.76	0.83
$Tr(\boldsymbol{\beta})$	1.86 ± 0.02	1.84	1.91	1.95
$Tr(\mathbf{C})$	0.83 ± 0.01	0.75	0.82	0.90
$Tr(\boldsymbol{\tau})$ (ms)	32.2 ± 0.1	31.30	32.10	32.90
$Tr(\boldsymbol{\mu})$ (μm)	5.09 ± 0.02	4.99	5.10	5.22
$Tr(\mathbf{H})$	0.58 ± 0.01	0.54	0.60	0.64

WM

	Mean ± StD	LQ	Median	UQ
$Tr(\mathbf{D})(\times 10^{-3} mm^2/s)$	0.94 ± 0.06	0.74	0.84	1.01
$Tr(\boldsymbol{\alpha})$	0.69 ± 0.02	0.63	0.67	0.72
$Tr(\boldsymbol{\beta})$	1.78 ± 0.01	1.73	1.79	1.85
$Tr(\mathbf{C})$	0.78 ± 0.02	0.72	0.75	0.81
$Tr(\boldsymbol{\tau})$ (ms)	32.7 ± 0.2	31.70	32.60	33.60
$Tr(\boldsymbol{\mu})$ (μm)	5.06 ± 0.03	4.93	5.05	5.18
$Tr(\mathbf{H})$	0.7 ± 0.01	0.68	0.72	0.75

Images computed from the MLF parameters, such as C, and entropy, H maps also showed exceptional tissue contrast. In particular, $C \sim 1$ was found in CSF regions consistent with Gaussian diffusion, whereas $C < 1$ was found in gray matter and white matter indicating a sub-diffusive growth of the diffusion propagator. Furthermore, lower values of C were found in white matter (~ 0.78) than cortical gray matter (~ 0.85) indicating a more sub-diffusive dynamic in white matter than cortical gray matter. Entropy maps showed greatest quantified and visible tissue contrast in comparison to other MLF parameter maps as shown by the lack of overlap between quartiles. Lowest entropy was found in the CSF ($H \sim 0.3$) with greater values in cortical gray matter ($H \sim 0.6$) and highest values in white matter ($H \sim 0.7$) and were consistent between datasets. As stated in the theory section, entropy measures the amount of information present in the signal decay curve, and a greater entropy is related to a more anomalous diffusion (i.e. greater deviation from Gaussian). This indicates that intuitively white matter has greater tissue complexity than cortical gray matter with CSF exhibiting the least complexity.

ROI results for lateral ventricle CSF, cortical GM, deep GM and WM are shown in Figure 25, Figure 26, and Figure 27. Figure 25 shows differentiation between the location of ROIs in (α,β) space with CSF represented by the most Gaussian decay curves. Moving from the cortex to deep GM structures (i.e., hippocampus, caudate, lentiform nucleus, thalamus) and to the WM, α and β exhibited progressively decreasing anomalous exponents (and increasing sub-diffusion). WM exponents were lowest and overlapped with thalamic ROI measures obtained for the step length distribution, β. Greater separation of ROIs was apparent in the graph

of entropy, H, against diffusion characteristic, C (Figure 26) where error bars show more robust characterization of tissue diffusion properties than Figure 25. In contrast, Figure 27 shows diffusion coefficient, D, against C and provides a less reliable separation of ROIs with overlapping error bars between the cortex and amygdala and the thalamus and WM regions. Interestingly, Figure 28 shows aggregate entropy values computed for the ROIs with respect to the estimated values forα and β in those pixels. Interestingly, Figure 28.c displays the entropy surface for the thalamus values and displays 3 distinct peaks that indicate differences in α, β and H in thalamic nuclei. Furthermore, it is clear that the ROIs presented in Figure 28 demonstrate that α, β, and H are able to describe a spectrum to distinguish tissue complexity through anomalous diffusion measurements. This analysis of parameter relationships to an ROI can be extended by performing a Spearman's correlation analysis on all of the fitted results of (Equation 2.13) and (Equation 2.16) as shown in Table XIII, Table XIV, and Table XV (51). As these tables show, each ROI has different fingerprint of parameter correlations to provide a general description of the type of diffusion measured in the tissue microstructure. And, to further elucidate the value of these anomalous diffusion measurement techniques, visible tissue contrast in the thalamus and other anatomical structures is clearly visible in MLF parameter maps shows for the high spatial resolution aDWI dataset obtained on a single, healthy subject (Figure 29).

Anisotropic MLF parameter maps and tissue contrast results computed in the low spatial resolution aDTI dataset are shown in Figure 30 and Table XVI. With regard to the directional orientation of the MLF parameters, it is clear, particularly with H that the eigenvector asso-

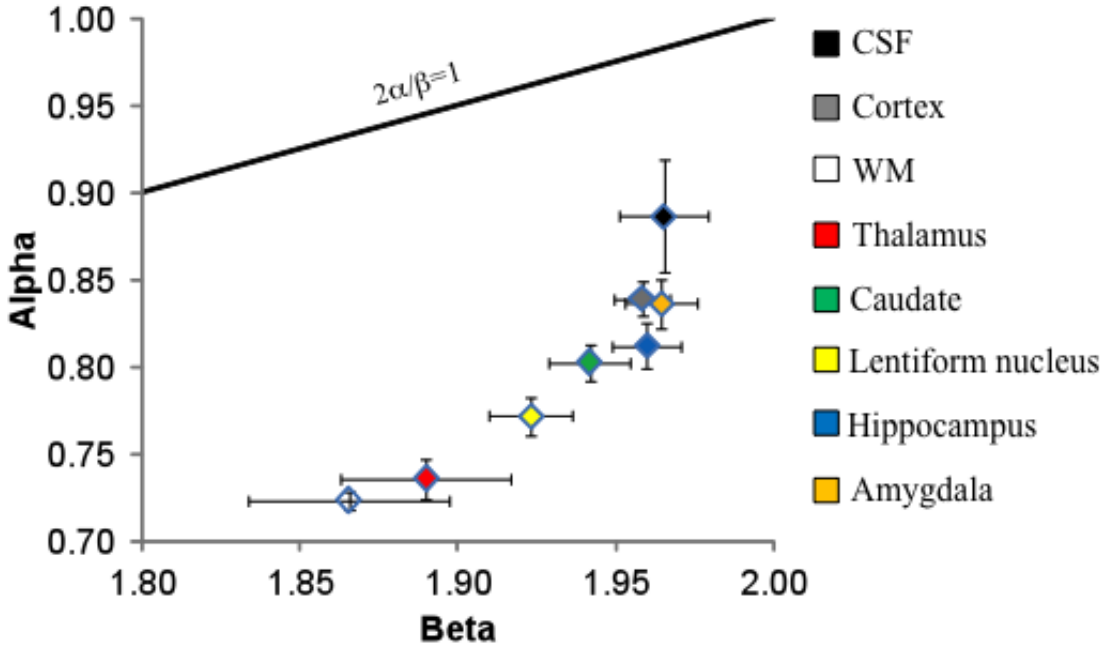

Figure 25. α, β scatter plot for ROIs in the HCP dataset with $2\alpha/\beta = 1$ line.

ciated with the largest eigenvalue is not aligned with the principal direction of diffusivity as given by D. With regard to α, β, and C it is apparent, though with markedly less coherence, that the eigenvectors associated with the smallest eigenvalues also are not aligned with the principal direction of diffusivity. These results indicate that, in general, the most anomalous diffusion was found to be perpendicular to the orientation of the WM fiber tract bundle direction, that is, in the direction for which the highest entropy estimations were found. However, as was determined in Chapter 5, it is clear that D is the most anisotropic diffusion parameter as can be seen by the scale of the FA maps in Figure 30, where $FA(D) < 0.7$, $FA(H) < 0.1$,

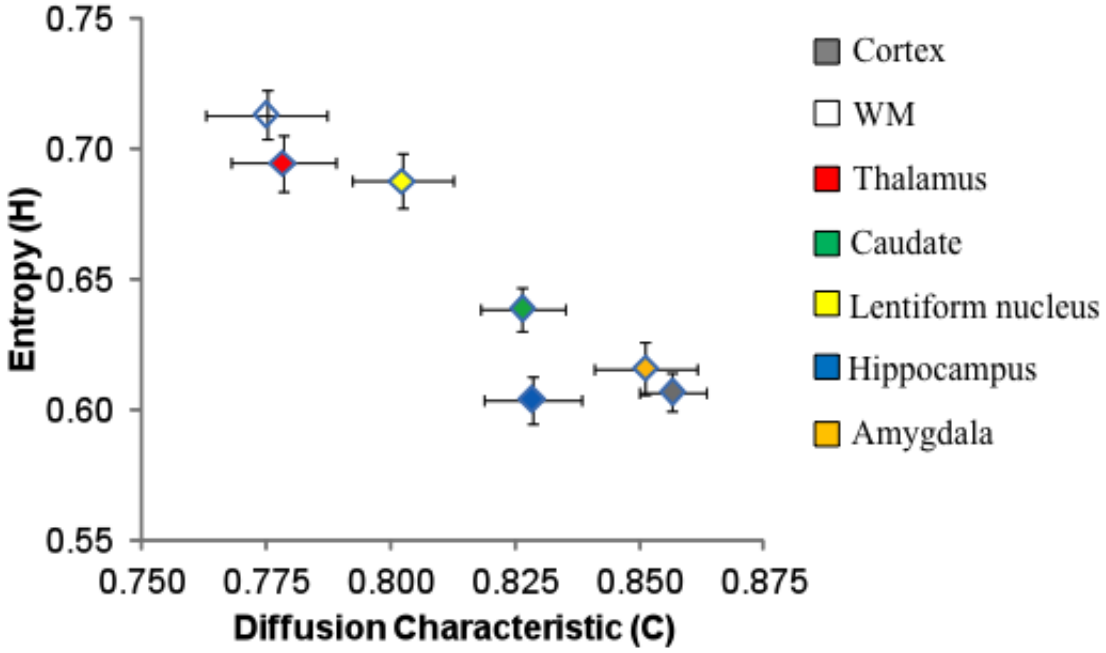

Figure 26. H, C scatter plot for ROIs in the HCP dataset, where $C = 2\alpha/\beta$.

$FA(\alpha) < 0.1$, $FA(\beta) < 0.1$, $FA(C) < 0.1$. In comparison to the anisotropic results on the high field imaging spectrometer for the rat brain shown in Figure 19, it is encouraging to find that similar parameter orientations are found on a clinical MRI system to image healthy human neural tissue. It appears that the study in Chapter 5 found that α and C are more anisotropic than has been determined in Chapter 6, however, this behavior can be explained by the experimental setup at 17.6T, sampling b-values up to 25,000 s/mm^2, whereas the results reported here sample b-values only up to 25,000 s/mm^2 which is limited in estimating the order of the power-law decay which is intimately associated with α.

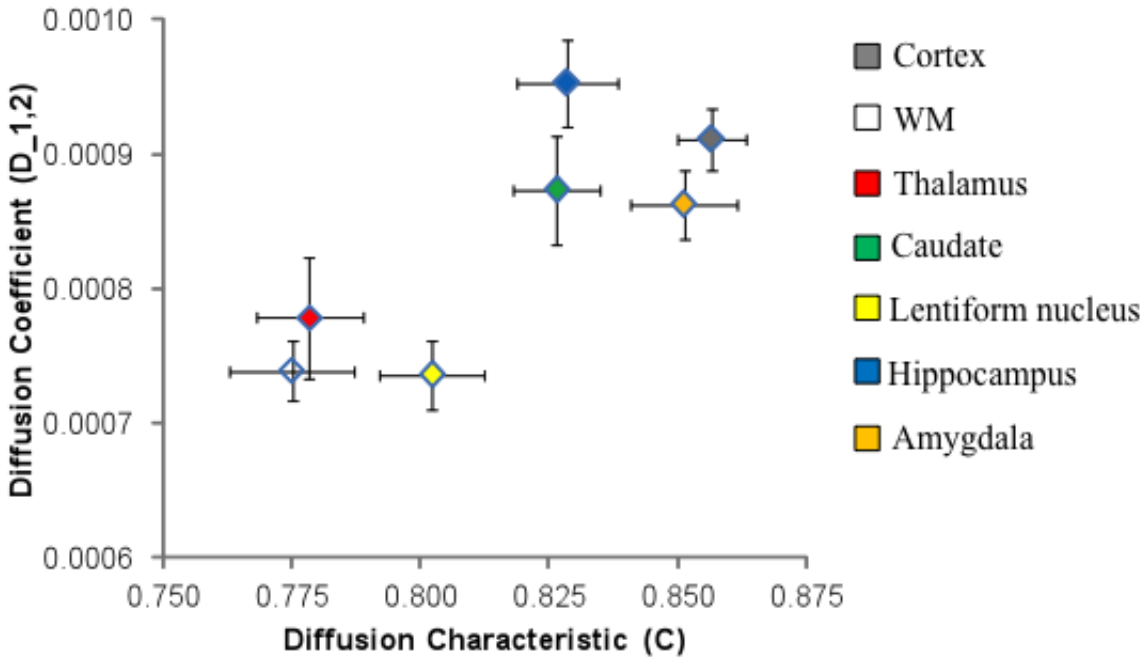

Figure 27. D, C scatter plot for ROIs in the HCP dataset, where $C = 2\alpha/\beta$.

6.4 Conclusions

This study demonstrated the viability of performing anomalous diffusion measurements on a clinical scanner to determine isotropic (Tr) and anisotropic (FA) estimations of tissue microstructure characteristics. The CTRW parameters in the form of the MLF provided new tissue contrast to classify ROIs in the CSF, cortical GM, deep GM, and WM. Additionally, the entropy in the diffusion process was able to provide clear separation of tissue types as an overall measure of statistical uncertainty in the characteristic function (i.e. spatial Fourier transform)

of the probability distribution for displacement. HCP data sets were also utilized to build MLF parameter maps utilizing only three $b - values$ (i.e. 1000, 2000, 3000 s/mm^2) and the results were constant for the low and high resolution acquisitions which collected six and ten b-values, respectively. Furthermore, the directional dependence of the MLF parameters and entropy indicate that the most anomalous behavior is not aligned with the principal direction of diffusivity, but rather appears to be aligned in a perpendicular fashion. Finally, with new and different contrast (to that of the diffusion coefficient) made available by these clinical *in vivo* analyses to classify healthy neural tissue structure, the MLF and entropy parameters are also potential clinical *in vivo* biomarkers for neurodegeneration.

TABLE XII

HCP DATA RESULTS FOR THE CSF, CORTICAL GM, AND WM ROIS.

CSF

	Mean ± StD	LQ	Median	UQ
$Tr(\mathbf{D})(\times 10^{-3} mm^2/s)$	2.49 ± 0.09	2.16	2.57	2.86
$Tr(\boldsymbol{\alpha})$	0.89 ± 0.03	0.85	0.93	0.96
$Tr(\boldsymbol{\beta})$	1.97 ± 0.01	1.98	1.98	1.98
$Tr(\mathbf{C})$	0.9 ± 0.03	0.86	0.94	0.97
$Tr(\boldsymbol{\tau})$ (ms)	39.1 ± 0.3	39.20	39.40	39.50
$Tr(\boldsymbol{\mu})$ (μm)	5.43 ± 0.03	5.38	5.40	5.43
$Tr(\mathbf{H})$	0.33 ± 0.02	0.27	0.30	0.38

Cortical GM

	Mean ± StD	LQ	Median	UQ
$Tr(\mathbf{D})(\times 10^{-3} mm^2/s)$	0.91 ± 0.02	0.74	0.82	0.99
$Tr(\boldsymbol{\alpha})$	0.84 ± 0.01	0.80	0.84	0.89
$Tr(\boldsymbol{\beta})$	1.96 ± 0.01	1.95	1.98	1.98
$Tr(\mathbf{C})$	0.86 ± 0.01	0.81	0.86	0.90
$Tr(\boldsymbol{\tau})$ (ms)	39.7 ± 0.1	39.60	39.60	39.80
$Tr(\boldsymbol{\mu})$ (μm)	5.37 ± 0.01	5.34	5.37	5.38
$Tr(\mathbf{H})$	0.61 ± 0.01	0.58	0.62	0.64

WM

	Mean ± StD	LQ	Median	UQ
$Tr(\mathbf{D})(\times 10^{-3} mm^2/s)$	0.74 ± 0.02	0.67	0.72	0.77
$Tr(\boldsymbol{\alpha})$	0.72 ± 0.01	0.68	0.71	0.76
$Tr(\boldsymbol{\beta})$	1.87 ± 0.03	1.80	1.87	1.93
$Tr(\mathbf{C})$	0.78 ± 0.01	0.74	0.77	0.80
$Tr(\boldsymbol{\tau})$ (ms)	40.1 ± 0.1	39.90	40.10	40.40
$Tr(\boldsymbol{\mu})$ (μm)	5.29 ± 0.01	5.25	5.29	5.33
$Tr(\mathbf{H})$	0.71 ± 0.01	0.69	0.72	0.74

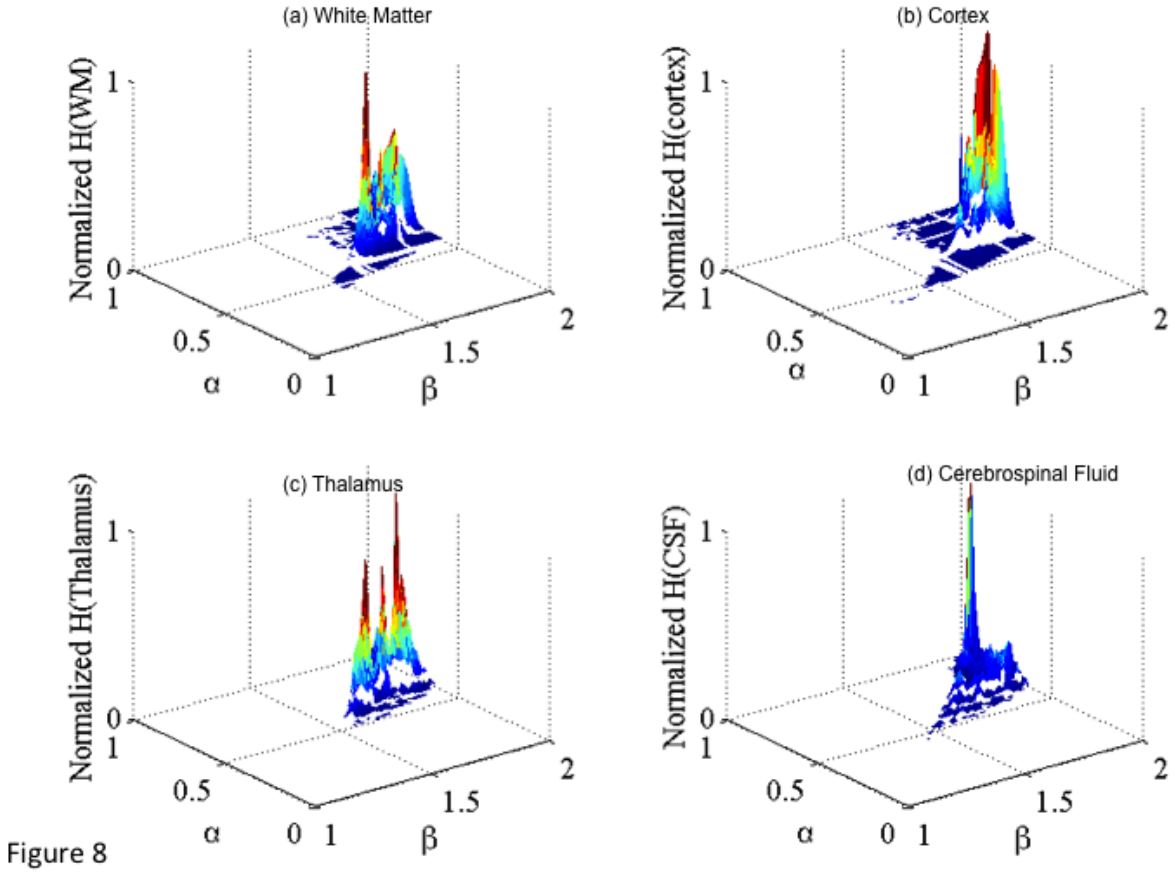

Figure 8

Figure 28. For eight HCP subjects, composite entropy surfaces with respect to (α,β) phase space for ROIs in the (a) cerebrospinal fluid, (b) cortical gray matter, (c) white matter and (d) thalamus.

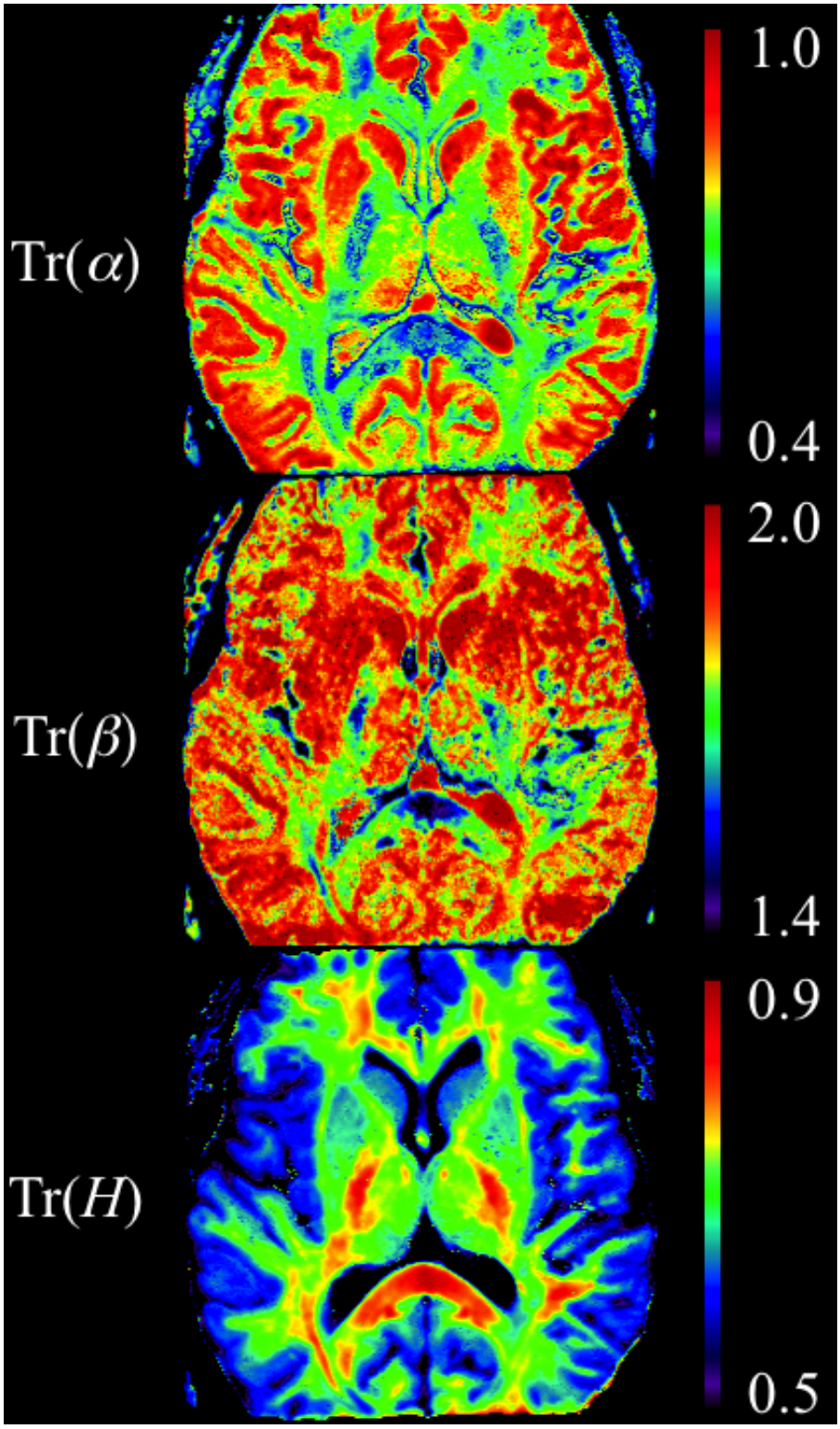

Figure 29. High resolution trace maps of α, β and H obtained from a single subject are shown.

TABLE XIII

SPEARMAN'S CORRELATIONS OF THE MLF AND ENTROPY PARAMETERS IN THE CSF

	$Tr(D)$	$Tr(\alpha)$	$Tr(\beta)$	$Tr(C)$	$Tr(\tau)$	$Tr(\mu)$	$Tr(H)$
$Tr(D)$	*	0.72	0.64	0.65	0.50	-0.49	-0.98
$Tr(\alpha)$	*	*	0.71	0.96	0.04	-0.02	-0.81
$Tr(\beta)$	*	*	*	0.54	0.34	-0.34	-0.70
$Tr(C)$	*	*	*	*	-0.10	0.12	-0.74
$Tr(\tau)$	*	*	*	*	*	-0.99	-0.45
$Tr(\mu)$	*	*	*	*	*	*	0.44
$Tr(H)$	*	*	*	*	*	*	*

TABLE XIV

SPEARMAN'S CORRELATIONS OF THE MLF AND ENTROPY PARAMETERS IN THE CORTICAL GM.

	$Tr(D)$	$Tr(\alpha)$	$Tr(\beta)$	$Tr(C)$	$Tr(\tau)$	$Tr(\mu)$	$Tr(H)$
$Tr(D)$	*	-0.13	0.23	-0.22	0.73	-0.73	-0.87
$Tr(\alpha)$	*	*	0.50	0.95	0.05	-0.08	-0.27
$Tr(\beta)$	*	*	*	0.26	0.48	-0.48	-0.47
$Tr(C)$	*	*	*	*	-0.10	0.06	-0.16
$Tr(\tau)$	*	*	*	*	*	-0.99	-0.77
$Tr(\mu)$	*	*	*	*	*	*	0.79
$Tr(H)$	*	*	*	*	*	*	*

TABLE XV

SPEARMAN'S CORRELATIONS OF THE MLF AND ENTROPY PARAMETERS IN THE WM.

	$Tr(D)$	$Tr(\alpha)$	$Tr(\beta)$	$Tr(C)$	$Tr(\tau)$	$Tr(\mu)$	$Tr(H)$
$Tr(D)$	*	0.29	0.46	0.09	0.69	-0.71	-0.79
$Tr(\alpha)$	*	*	0.80	0.84	0.61	-0.65	-0.76
$Tr(\beta)$	*	*	*	0.42	0.83	-0.82	-0.83
$Tr(C)$	*	*	*	*	0.25	-0.33	-0.48
$Tr(\tau)$	*	*	*	*	*	-0.98	-0.88
$Tr(\mu)$	*	*	*	*	*	*	0.90
$Tr(H)$	*	*	*	*	*	*	*

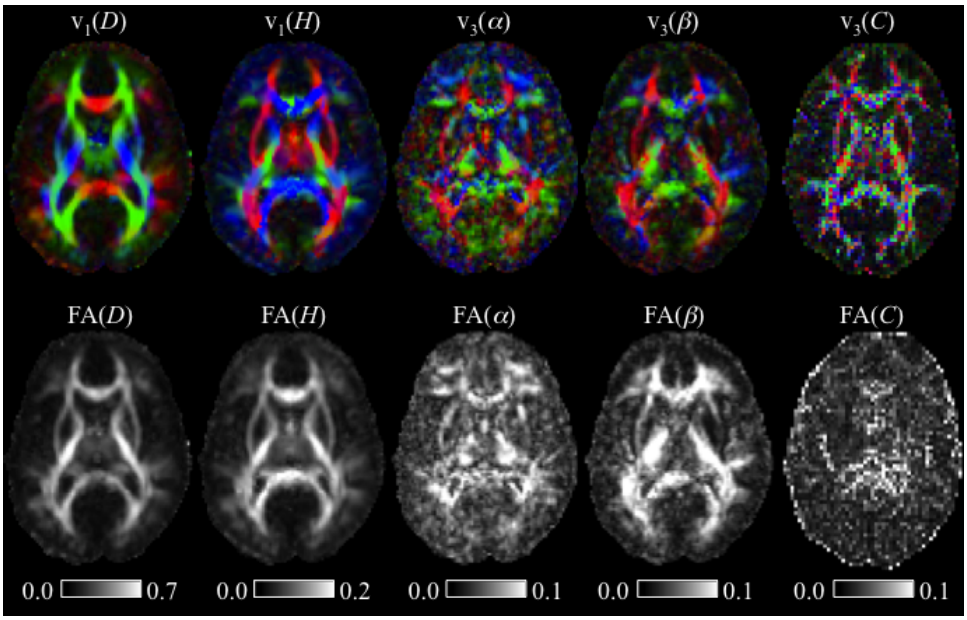

Figure 30. DEC and FA maps for the normalized composite image of eight healthy volunteers.

TABLE XVI

RESULTS FOR ANISOTROPY OF THE MLF AND ENTROPY PARAMETERS USING THE LOW RESOLUTION (3 MM ISOTROPIC, 12-DIRECTIONS, B-VALUES UP TO 5,000 S/MM^2) ACQUIRED AT SGUL

	CSF	Cortical GM	WM
$FA(\mathbf{D})$	0.18 ± 0.02	0.27 ± 0.02	0.59 ± 0.02
$FA(\boldsymbol{\alpha})$	0.11 ± 0.01	0.11 ± 0.01	0.15 ± 0.02
$FA(\boldsymbol{\beta})$	0.18 ± 0.02	0.14 ± 0.01	0.24 ± 0.01
$FA(\mathbf{C})$	0.16 ± 0.01	0.14 ± 0.02	0.18 ± 0.02
$FA(\boldsymbol{\tau})$	0.05 ± 0.01	0.04 ± 0.00	0.05 ± 0.01
$FA(\boldsymbol{\mu})$	0.04 ± 0.00	0.03 ± 0.00	0.05 ± 0.00
$FA(\mathbf{H})$	0.08 ± 0.01	0.08 ± 0.00	0.17 ± 0.01

CHAPTER 7

CONCLUSIONS & FUTURE WORK

In the course of this project, the following key points have been established:

1. *Chapter 2 & Chapter 3.* As measured by the entropy formalism, systems described by fractional order derivatives contain more information than do systems described by integer order derivatives. From this perspective, measurements of anomalous diffusion in biological tissue can infer an estimation of structural complexity (i.e., heterogeneity, tortuousity) through fractional powers (α and β) and entropy (H).

2. *Chapter 2 & Chapter 4.* The MLF represents the characteristic function of the pdf and is the closed form solution to the generalized diffusion equation, which encapsulates the four special classes of diffusion: Gaussian diffusion for $\alpha = 1$ and $\beta = 2$ (Brownian motion), time-fractional sub-diffusion for $\alpha < 1$ and $\beta = 2$, space-fractional super-diffusion $\alpha = 1$ and $\beta < 2$, time- and space-fractional anomalous diffusion for $\alpha < 1$ and $\beta < 2$. Diffusion measurements performed on healthy neural tissue demonstrated the data conformed to either Gaussian, time-fractional, or time- and space-fractional diffusion. The data did not indicate a mode of super-diffusion, which would have implied a stretched exponential formalism (i.e. $exp(-D_{1,\beta}q^{\beta}\bar{\Delta})$). Furthermore, the composite exponent for the MSD of the diffusion propagator indicate that all ROIs in the WM, GM, and CSF were either sub diffusive or Gaussian, that is, $2\alpha/\beta = C \leq 1$.

3. *Chapter 4.* Fixed Δ and fixed q protocols produced different measured diffusion dynamics for the same neural tissue, indicating that the values chosen for pulse sequence parameters Δ, δ, and q are crucial in order to extract the most information about the tissue microstructure. In general, the fixed Δ protocols provided better tissue contrast compared to the fixed q protocols. Within the fixed Δ protocols, the acquisition that minimized the mixing time and maximized the range of q-values sampled produced the best tissue contrast.

4. *Chapter 5.* Anisotropic investigations of the MLF and entropy parameters demonstrated that there is a directional dependence of α, β, C, and H in the WM, which is particularly coherent when performing a fixed Δ protocol. The orientation of the eigenvector associated with the smallest α, β, C eigenvalues and the eigenvector associated with largest H are not aligned with the principal direction of diffusivity (as determined by D). Rather, the directions appear to be orthogonal to the eigenvector associated with the largest D. However, the anisotropy in the MLF and entropy measures are modulated by significantly smaller magnitudes of FA, compared to D. In the fixed q experiment, the MLF parameters are more isotropic compared to the fixed Δ experiment.

5. *Chapter 5.* The MLF and entropy parameters were able to provide additional information to the diffusion coefficient in order to characterize ROIs in healthy adolescent and adult neural tissue. Whereas $FA(D)$ showed a moderate increase in the CCC, $FA(\alpha)$, and $FA(C)$ increased with greater separation for the ROI, indicating that the shape of the

tail on the decay curve–which is described by α and β–may be a more effective indicator of morphology in tissue microstructure than D–indicative of the initial decay.

6. *Chapter 5.* Although the MLF and entropy parameters demonstrated anisotropic features, the trace values provided excellent contrast in both WM and GM as well as between the young and adult groups. This finding indicates that an isotropic, or even a one dimensional DWI acquisition protocol has the capability to capture tissues microstructure features. In general, for the WM, the diffusion became more anomalous as age increased. Surprisingly, in contrast, for the GM, the diffusion became less anomalous as age increased.

7. *Chapter 6.* The MLF and entropy analyses of anomalous diffusion in neural tissue was successfully extended from *ex vivo* studies of fixed rat brain tissue on a high field imaging spectrometer to *in vivo* studies of human volunteers on a clinical MRI system. In general, the clinical results for the orientation of the anisotropic measures were in agreement with the results reported in Chapter 5. That is, the direction of the most anomalous diffusion is not aligned with the principal direction of diffusivity.

8. *Chapter 6.* At b-values arrayed up to only $\sim$3,000 s/mm^2, the MLF is able to describe anomalous diffusion to provide clear tissue contrast and separation of WM, cortical GM and deep GM structures. The high resolution HCP dataset was utilized in order to estimate trace values of α, β, and H in which GM ROIs such as the thalamus, lentiform nucleus, caudate, hippocampus, and amygdala were clearly separated from each other. Additionally, within a deep GM ROI, such as the thalamus, it is apparent that α, β, and H are able to identify detailed anatomical features like the individual nuclei. These

results indicate that high resolution acquisitions, anomalous diffusion measurements, and analyses, when combined, serve as a valuable tool in pre-surgical planning.

Future work will focus applying these techniques and analyses to characterize microstructure in neurodegeneration. Additionally, histological validation will be performed in order to visualize the tissue composition, within the resolution of one voxel that generates a signature of α, β, and H. It should be emphasized that the analyses are only as good as the quality of the DWI acquisition, and as such, continual improvement of the gradient coil amplitude capability and main magnetic field strength (e.g., 7T full body clinical system) will only improve the characterization of neural tissue with anomalous diffusion measurements.

APPENDICES

Appendix A

DATA PROCESSING

A.1 Raw signal corrections

For each voxel, the raw signal S_{raw} was Rician noise corrected with,

$$S_{rc} = \sqrt{S_{raw}^2 - 2\sigma_n^2}, \tag{A.1}$$

where S_{rc} is the Rician corrected signal and σ_n^2 is the variance in the background noise floor.

To account for T1 recovery effects at long diffusion times, S_{rc} was corrected with,

$$S = S_{rc} exp(\Delta/T1), \tag{A.2}$$

where T1 was computed using the variable TR data.

A.2 Fixed Δ experiment μ and τ estimations

For the fixed Δ, variable q experiments, first an estimate of μ was made followed by an estimate of τ. To estimate μ as $\bar{\mu}$, the signal decay was fit to,

$$S/S_0 = exp[-(bD_{\bar{\beta}})^{\bar{\beta}}], \tag{A.3}$$

Appendix A (Continued)

where $D_{\bar{\beta}}$ is the apparent diffusion coefficient of an exponential function stretched in $\bar{\beta}$. Thus, it follows that a diffusion coefficient equivalency can be formulated as,

$$(D_{\bar{\beta}})^{\bar{\beta}} = D_m\Big(\frac{\bar{\Delta}}{\bar{\mu}^2}\Big)^{1-\bar{\beta}} \tag{A.4}$$

to solve for $\bar{\mu}$,

$$\bar{\mu} = \sqrt{\bar{\Delta}}\Big[\frac{(D_{\bar{\beta}})^{\bar{\beta}}}{D_m}\Big]^{\frac{1}{2(\bar{\beta}-1)}}, \tag{A.5}$$

where the value for Δ is known from the fixed Δ experiment. Then, to estimate τ as $\bar{\tau}$, the signal decay was fit to,

$$S/S_0 = exp\Big[-D_{\bar{\alpha}}\frac{1}{\bar{\mu}^2}(b\bar{\mu}^2)^{\bar{\alpha}}\Big], \tag{A.6}$$

where $D_{\bar{\alpha}}$ is the apparent diffusion coefficient of an exponential function stretched in $\bar{\alpha}$. Thus, it follows that a diffusion coefficient equivalency can be formulated as,

$$D_{\bar{\alpha}} = D_m\Big(\frac{\bar{\Delta}}{\bar{\tau}^{\bar{\alpha}}}\Big) \tag{A.7}$$

to solve for $\bar{\tau}$,

$$\bar{\tau} = \Big(\bar{\Delta}\frac{D_m}{D_{\bar{\alpha}}}\Big)^{\frac{1}{\bar{\alpha}}}, \tag{A.8}$$

again, where the value for $\bar{\Delta}$ is known from the fixed Δ experiment.

Appendix A (Continued)

A.3 Fixed q experiment μ and τ estimations

For the fixed q, variable Δ experiments, first an estimate of τ was made followed by an estimate of μ. To estimate τ as $\bar{\tau}$, the signal decay was fit to,

$$S/S_0 = exp[-(bD_{\bar{\alpha}})^{\bar{\alpha}}], \tag{A.9}$$

where $D_{\bar{\alpha}}$ is the apparent diffusion coefficient of an exponential function stretched in $\bar{\alpha}$. Thus, it follows that a diffusion coefficient equivalency can be formulated as,

$$(D_{\bar{\alpha}})^{\bar{\alpha}} = D_m(q^2\bar{\tau})^{1-\bar{\alpha}} \tag{A.10}$$

to solve for $\bar{\tau}$,

$$\bar{\tau} = \frac{1}{q^2}\Big[\frac{(D_{\bar{\alpha}})^{\bar{\alpha}}}{D_m}\Big]^{\frac{1}{1-\bar{\alpha}}}, \tag{A.11}$$

where the value for q is known from the fixed q experiment. Then, to estimate μ as $\bar{\mu}$, the signal decay was fit to,

$$S/S_0 = exp\Big[-D_{\bar{\beta}}\bar{\tau}(\frac{b}{\bar{\tau}})^{\bar{\beta}}\Big], \tag{A.12}$$

where $D_{\bar{\beta}}$ is the apparent diffusion coefficient of an exponential function stretched in $\bar{\beta}$. Thus, it follows that a diffusion coefficient equivalency can be formulated as,

$$D_{\bar{\beta}} = D_m\Big(\frac{\mu^{\bar{\beta}}}{q^2}\Big) \tag{A.13}$$

Appendix A (Continued)

to solve for $\bar{\mu}$,

$$\bar{\mu} = \left(q^2 \frac{D_{\bar{\beta}}}{D_m}\right)^{\frac{1}{\bar{\beta}}}, \tag{A.14}$$

again, where the value for q is known from the fixed q experiment.

Appendix B

TABLES

TABLE XVII

COMPARISON OF D_M AND $D_{1,2}$ FOR THE FIXED $\Delta_1 = 17.5\,MS$, $\Delta_2 = 50\,MS$, $Q_1 = 78\,MM^{-1}$, $Q_2 = 52\,MM^{-1}$ EXPERIMENTS.

parameter	ROI	Δ_1	Δ_2	q_1	q_2
D_m ($\times 10^{-3} mm^2/s$)	(1) Cor, l	0.32± 0.01	0.35± 0.02	0.28± 0.01	0.31± 0.01
	(2) Cor, r	0.31± 0.01	0.25± 0.02	0.26± 0.01	0.28± 0.01
	(3) CC, l	0.32± 0.05	0.33± 0.09	0.25± 0.04	0.29± 0.04
	(4) CC, c	0.37± 0.03	0.34± 0.04	0.23± 0.02	0.29± 0.03
	(5) CC, r	0.34± 0.02	0.26± 0.03	0.24± 0.02	0.27± 0.02
	(6) Str, l	0.27± 0.02	0.29± 0.01	0.23± 0.01	0.25± 0.01
	(7) Str, r	0.28± 0.02	0.23± 0.02	0.23± 0.01	0.25± 0.01
$D_{1,2}$ ($\times 10^{-3} mm^2/s$)	(1) Cor, l	0.32 ± 0.01	0.35 ± 0.02	0.29 ± 0.01	0.32 ± 0.01
	(2) Cor, r	0.31 ± 0.01	0.26 ± 0.02	0.27 ± 0.01	0.28 ± 0.01
	(3) CC, l	0.32 ± 0.05	0.35 ± 0.11	0.26 ± 0.05	0.29 ± 0.05
	(4) CC, c	0.36 ± 0.04	0.35 ± 0.05	0.25 ± 0.02	0.30 ± 0.03
	(5) CC, r	0.34 ± 0.03	0.27 ± 0.03	0.26 ± 0.02	0.28 ± 0.02
	(6) Str, l	0.27 ± 0.02	0.28 ± 0.01	0.24 ± 0.01	0.26 ± 0.01
	(7) Str, r	0.28 ± 0.02	0.23 ± 0.01	0.24 ± 0.01	0.25 ± 0.01

Appendix B (Continued)

TABLE XVIII

MLF PARAMETER VALUES FOR ROIS IN THE FIXED $\Delta_1 = 17.5\,MS$, $\Delta_2 = 50\,MS$, $Q_1 = 78\,MM^{-1}$, $Q_2 = 52\,MM^{-1}$ EXPERIMENTS (Y-AXIS DIFFUSION WEIGHTING).

parameter	ROI	Δ_1	Δ_2	q_1	q_2
α	(1) Cor, l	0.76 ± 0.05	0.92 ± 0.04	0.95 ± 0.01	0.96 ± 0.01
	(2) Cor, r	0.74 ± 0.06	0.92 ± 0.02	0.94 ± 0.01	0.95 ± 0.01
	(3) CC, l	0.40 ± 0.11	0.50 ± 0.25	0.82 ± 0.04	0.89 ± 0.02
	(4) CC, c	0.42 ± 0.04	0.39 ± 0.05	0.69 ± 0.05	0.80 ± 0.03
	(5) CC, r	0.33 ± 0.13	0.55 ± 0.18	0.82 ± 0.03	0.86 ± 0.04
	(6) Str, l	0.58 ± 0.07	0.79 ± 0.09	0.89 ± 0.01	0.91 ± 0.02
	(7) Str, r	0.57 ± 0.06	0.83 ± 0.03	0.91 ± 0.02	0.92 ± 0.01
β	(1) Cor, l	1.95 ± 0.06	1.76 ± 0.14	1.91 ± 0.03	1.98 ± 0.02
	(2) Cor, r	1.95 ± 0.08	1.99 ± 0.03	1.93 ± 0.04	1.90 ± 0.05
	(3) CC, l	1.79 ± 0.17	1.80 ± 0.16	1.91 ± 0.08	1.97 ± 0.04
	(4) CC, c	1.15 ± 0.13	1.42 ± 0.07	1.85 ± 0.07	1.96 ± 0.04
	(5) CC, r	1.82 ± 0.16	1.97 ± 0.09	1.88 ± 0.09	1.92 ± 0.05
	(6) Str, l	1.99 ± 0.04	1.87 ± 0.14	1.98 ± 0.03	1.92 ± 0.03
	(7) Str, r	2.00 ± 0.02	2.00 ± 0.04	1.98 ± 0.02	1.97 ± 0.03
$D_{1,2}$ $(\times 10^{-3} mm^2/s)$	(1) Cor, l	0.32 ± 0.01	0.35 ± 0.02	0.29 ± 0.01	0.32 ± 0.01
	(2) Cor, r	0.31 ± 0.01	0.26 ± 0.02	0.27 ± 0.01	0.28 ± 0.01
	(3) CC, l	0.32 ± 0.05	0.35 ± 0.11	0.26 ± 0.05	0.29 ± 0.05
	(4) CC, c	0.36 ± 0.04	0.35 ± 0.05	0.25 ± 0.02	0.30 ± 0.03
	(5) CC, r	0.34 ± 0.03	0.27 ± 0.03	0.26 ± 0.02	0.28 ± 0.02
	(6) Str, l	0.27 ± 0.02	0.28 ± 0.01	0.24 ± 0.01	0.26 ± 0.01
	(7) Str, r	0.28 ± 0.02	0.23 ± 0.01	0.24 ± 0.01	0.25 ± 0.01
μ (μm)	(1) Cor, l	2.39 ± 0.27	4.09 ± 0.22	2.15 ± 0.11	3.37 ± 0.54
	(2) Cor, r	2.40 ± 0.37	3.01 ± 0.97	2.12 ± 0.08	3.36 ± 0.29
	(3) CC, l	2.26 ± 0.27	3.94 ± 0.45	1.96 ± 0.13	3.38 ± 0.26
	(4) CC, c	2.44 ± 0.09	4.08 ± 0.36	1.82 ± 0.11	2.95 ± 0.17
	(5) CC, r	2.33 ± 0.06	3.29 ± 0.47	1.96 ± 0.05	3.23 ± 0.20
	(6) Str, l	2.18 ± 0.29	3.86 ± 0.35	2.16 ± 0.10	3.45 ± 0.23
	(7) Str, r	2.15 ± 0.35	2.97 ± 0.67	2.17 ± 0.11	3.49 ± 0.25
τ (ms)	(1) Cor, l	16.88 ± 1.48	50.62 ± 2.14	21.47 ± 1.17	30.98 ± 6.85
	(2) Cor, r	16.67 ± 1.65	54.46 ± 6.57	22.09 ± 1.89	33.88 ± 5.08
	(3) CC, l	19.94 ± 1.42	60.61 ± 6.71	25.50 ± 1.28	36.62 ± 6.99
	(4) CC, c	23.14 ± 1.41	67.50 ± 2.53	27.88 ± 2.05	41.21 ± 3.67
	(5) CC, r	20.25 ± 0.84	58.99 ± 2.89	25.57 ± 1.35	38.56 ± 3.97
	(6) Str, l	18.39 ± 1.42	52.68 ± 3.17	23.80 ± 1.90	38.15 ± 7.80
	(7) Str, r	18.78 ± 1.28	55.04 ± 2.78	22.87 ± 1.04	38.12 ± 4.21

CITED LITERATURE

1. Shannon, C. E.: A mathematical theory of communication. Bell Sys Tech J, 27:379–423, July 1948.

2. Wigner, E. P.: The unreasonable effectiveness of mathematics in the natural sciences. Communications on Pure and Applied Mathematics, 13(1):1–14, 1960.

3. Abragam, A.: The principles of nuclear magnetism. Oxford, Clarendon Press, 1961.

4. Callaghan, P. T.: Principles of nuclear magnetic resonance microscopy. Oxford, Clarendon Press, 1991.

5. Basser, P. J. and Pierpaoli, C.: Microstructural and physiological features of tissues elucidated by quantitative-diffusion-tensor mri. J Magn Reson B, 111(3):209–19, Jun 1996.

6. Metzler, R. and Klafter, J.: The random walk's guide to anomalous diffusion: a fractional dynamics approach. Physics Reports, 339(1):1–77, 2000.

7. Meerschaert, M. M. and Sikorskii, A.: Stochastic models for fractional calculus, volume 43. Berlin, De Gruyter, 2012.

8. Haus, J. W., Kehr, K. W., and Kitahara, K.: Long-time tail effects on particle diffusion in a disordered system. Phys. Rev. B, 25:4918–4921, Apr 1982.

9. Haus, J. and Kehr, K.: Diffusion in regular and disordered lattices. Physics Reports, 150(5–6):263 – 406, 1987.

10. Klages, R., Radons, G., and Sokolov, I. M.: Anomalous transport: foundations and applications. Weinheim, Wiley, 2008.

11. Mazo, R. M.: Brownian motion: fluctuations, dynamics, and applications. Oxford, UK, Clarendon Press, 2009.

12. Cushman, J. H., O'Malley, D., and Park, M.: Anomalous diffusion as modeled by a nonstationary extension of brownian motion. Phys Rev E Stat Nonlin Soft Matter Phys, 79(3):032101, 2009.

13. Le Bihan, D.: Diffusion and perfusion magnetic resonance imaging: applications to functional MRI. New York, Raven Press, 1995.

14. Bennett, K. M., Schmainda, K. M., Bennett, R. T., Rowe, D. B., Lu, H., and Hyde, J. S.: Characterization of continuously distributed cortical water diffusion rates with a stretched-exponential model. Magn Reson Med, 50(4):727–34, Oct 2003.

15. Magin, R. L., Abdullah, O., Baleanu, D., and Zhou, X. J.: Anomalous diffusion expressed through fractional order differential operators in the bloch-torrey equation. J Magn Reson, 190(2):255–270, Feb 2008.

16. Zhou, X. J., Gao, Q., Abdullah, O., and Magin, R. L.: Studies of anomalous diffusion in the human brain using fractional order calculus. Magn Reson Med, 63(3):562–569, 2010.

17. De Santis, S., Gabrielli, A., Bozzali, M., Maraviglia, B., Macaluso, E., and Capuani, S.: Anisotropic anomalous diffusion assessed in the human brain by scalar invariant indices. Magn Reson Med, 65(4):1043–52, Apr 2011.

18. Hall, M. G. and Barrick, T. R.: From diffusion-weighted mri to anomalous diffusion imaging. Magn Reson Med, 59(3):447–55, Mar 2008.

19. Hall, M. G. and Barrick, T. R.: Two-step anomalous diffusion tensor imaging. NMR Biomed, 25(2):286–94, Feb 2012.

20. Ozarslan, E., Basser, P. J., Shepherd, T. M., Thelwall, P. E., Vemuri, B. C., and Blackband, S. J.: Characterization of anomalous diffusion from mr signal may be a new probe to tissue microstructure. Conf Proc IEEE Eng Med Biol Soc, 1:2256–9, 2006.

21. Özarslan, E., Shepherd, T. M., Koay, C. G., Blackband, S. J., and Basser, P. J.: Temporal scaling characteristics of diffusion as a new mri contrast: findings in rat hippocampus. Neuroimage, 60(2):1380–93, Apr 2012.

22. Zaslavsky, G. M.: Hamiltonian chaos and fractional dynamics. New York, Oxford University Press, 2005.

23. Gorenflo, R., Vivoli, A., and Mainardi, F.: Discrete and continuous random walk models for space-time fractional diffusion. Nonlinear Dynam, 38:101–116, 2004.

24. Podlubny, I.: Fractional differential equations. San Diego, Academic Press, 1999.

25. Herrmann, R.: Fractional calculus: an introduction for physicists. Singapore, World Scientific, 2011.

26. Hilfer, R.: Applications of fractional calculus in physics. Singapore, World Scientific, 2000.

27. Ortigueira, M. D.: Fractional calculus for scientists and engineers. New York, Springer, 2011.

28. Saxena, R. K., Mathai, A. M., and Haubold, H. J.: Fractional reaction-diffusion equations. Astrophys. Space Sci., 305(3):289–296, 2006.

29. Haubol, H. J., Mathai, A. M., and Saxena, R. K.: Mittag-leffler functions and their applications. J App Math, 2011:298628, 2011.

30. Berberan-Santos, M. N.: Relation between the inverse laplace transforms of i(t) and i(t): Application to the mittag-leffler and asymptotic inverse power law relaxation functions. Journal of Mathematical Chemistry, 38(2):265–270, 2005.

31. Berberan-Santos, M. N.: Analytical inversion of the laplace transform without contour integration: application to luminescence decay laws and other relaxation functions. Journal of Mathematical Chemistry, 38(2):165–173, 2005.

32. Berberan-Santos, M. N.: Properties of the mittag-leffler relaxation function. Journal of Mathematical Chemistry, 38(4):629–635, 2005.

33. Wheatcraft, S. W. and Meerschaert, M. M.: Fractional conservation of mass. Adv. Water Resour, 31(10):1377 – 1381, 2008.

34. Leszczynski, J. S.: An introduction to fractional mechanics. Czestochowa University of Technology, 2011.

35. West, B. J., Bologna, M., and Grigolini, P.: Physics of fractal operators. New York, Springer, 2003.

36. Palombo, M., Gabrielli, A., De Santis, S., Cametti, C., Ruocco, G., and Capuani, S.: Spatio-temporal anomalous diffusion in heterogeneous media by nuclear magnetic resonance. J Chem Phys, 135(3):034504, Jul 2011.

37. Viertiö-Oja, H., Maja, V., Särkelä, M., Talja, P., Tenkanen, N., Tolvanen-Laakso, H., Paloheimo, M., Vakkuri, A., Yli-Hankala, A., and Meriläinen, P.: Description of the entropy algorithm as applied in the datex-ohmeda s/5 entropy module. Acta Anaesth Scand, 48(2):154–161, 2004.

38. Kirsch, M. R., Monahan, K., Weng, J., Redline, S., and Loparo, K. A.: Entropy-based measures for quantifying sleep-stage transition dynamics: relationship to sleep fragmentation and daytime sleepiness. IEEE Trans Biomed Eng, 59(3):787–96, Mar 2012.

39. Bar-Yam, Y.: Dynamics of Complex Systems. Reading MA, Perseus Books, 1997.

40. Vendruscolo and Marsili: Diffusion in disordered media as a process with memory. Phys Rev E Stat Phys Plasmas Fluids Relat Interdiscip Topics, 54(2):R1021–R1024, Aug 1996.

41. Wang, B., Kuo, J., Bae, S. C., and Granick, S.: When brownian diffusion is not gaussian. Nature Materials, 11:481–485, 2012.

42. Bruce, E. N.: Biomedical signal processing and signal modeling. New York, Wiley, 2001.

43. Podlubny, I.: The Mittag-Leffler function. www. mathworks. com/ matlabcentral/ fileexchange/ 8738, 2009.

44. Parekh, M. B., Carney, P. R., Sepulveda, H., Norman, W., King, M., and Mareci, T. H.: Early mr diffusion and relaxation changes in the parahippocampal gyrus precede the onset of spontaneous seizures in an animal model of chronic limbic epilepsy. Exp Neurol, 224(1):258 – 270, 2010.

45. Mikula, S., Binding, J., and Denk, W.: Staining and embedding the whole mouse brain for electron microscopy. Nat Methods, doi:10.1038/nmeth.2213, Oct 2012.

46. Ingo, C., Magin, R. L., Colon-Perez, L., Triplett, W., and Mareci, T. H.: On random walks and entropy in diffusion-weighted magnetic resonance imaging studies of neural tissue. Magn Reson Med, Mar 2013.

47. Magin, R. L., Ingo, C., Colon-Perez, L., Triplett, W., and Mareci, T. H.: Characterization of anomalous diffusion in porous biological tissues using fractional order derivatives and entropy. Microporous and Mesoporous Materials, 178(0):39 – 43, 2013.

48. Pajevic, S. and Pierpaoli, C.: Color schemes to represent the orientation of anisotropic tissues from diffusion tensor data: application to white matter fiber tract mapping in the human brain. Magn Reson Med, 42(3):526–40, Sep 1999.

49. Callaghan, P. T.: Translational dynamics and magnetic resonance: principles of pulsed gradient spin echo NMR. Oxford, Oxford University Press, 2011.

50. Van Essen, D. C., Ugurbil, K., Auerbach, E., Barch, D., Behrens, T. E. J., Bucholz, R., Chang, A., Chen, L., Corbetta, M., Curtiss, S. W., Della Penna, S., Feinberg, D., Glasser, M. F., Harel, N., Heath, A. C., Larson-Prior, L., Marcus, D., Michalareas, G., Moeller, S., Oostenveld, R., Petersen, S. E., Prior, F., Schlaggar, B. L., Smith, S. M., Snyder, A. Z., Xu, J., Yacoub, E., and WU-Minn HCP Consortium: The human connectome project: a data acquisition perspective. Neuroimage, 62(4):2222–31, Oct 2012.

51. Spearman, C.: The proof and measurement of association between two things. The American journal of psychology, 15(1):72–101, 1904.

52. Beck, C.: Generalised information and entropy measures in physics. Contemporary Physics, 50(4):495–510, 2009.

53. Budde, M. D. and Frank, J. A.: Examining brain microstructure using structure tensor analysis of histological sections. Neuroimage, 63(1):1–10, 2012.

54. Budde, M. D., Janes, L., Gold, E., Turtzo, L. C., and Frank, J. A.: The contribution of gliosis to diffusion tensor anisotropy and tractography following traumatic brain injury: validation in the rat using fourier analysis of stained tissue sections. Brain, 134(8):2248–2260, 2011.

55. Budde, M. D., Kim, J. H., Liang, H.-F., Russell, J. H., Cross, A. H., and Song, S.-K.: Axonal injury detected by in vivo diffusion tensor imaging correlates with neurological disability in a mouse model of multiple sclerosis. NMR Biomed, 21(6):589–597, 2008.

56. Budde, M. D., Xie, M., Cross, A. H., and Song, S.-K.: Axial diffusivity is the primary correlate of axonal injury in the experimental autoimmune encephalomyelitis spinal cord: a quantitative pixelwise analysis. J Neurosci, 29(9):2805–2813, 2009.

57. De Santis, S., Rebuzzi, M., Di Pietro, G., Fasano, F., Maraviglia, B., and Capuani, S.: In vitro and in vivo mr evaluation of internal gradient to assess trabecular bone density. Phys Med Biol, 55(19):5767–85, Oct 2010.

58. Gao, Q., Srinivasan, G., Magin, R. L., and Zhou, X. J.: Anomalous diffusion measured by a twice-refocused spin echo pulse sequence: analysis using fractional order calculus. J Magn Reson Imaging, 33(5):1177–83, May 2011.

59. Gleick, J.: The information: a history, a theory, a flood. New York, Pantheon Books, 1st ed edition, 2011.

60. Jensen, J. H. and Helpern, J. A.: Mri quantification of non-gaussian water diffusion by kurtosis analysis. NMR Biomed, 23(7):698–710, Aug 2010.

61. Kimmich, R.: NMR: tomography, diffusometry, relaxometry. Berlin, Springer, 1997.

62. Magin, R. and Ingo, C.: Entropy and information in a fractional order model of anomalous diffusion. IFAC Symposium on System Identification, 16(1):10.3182/20120711–3–BE–2027.00063, 2012.

63. Magin, R. L.: Fractional calculus in bioengineering. Connecticut, Begell House Publishers, 2006.

64. Magin, R. L., L., W., Velasco, M. P., Trujillo, J., Reiter, D. A., Morgenstern, A., and Spencer, R. G.: Anomalous nmr relaxation in cartilage matrix components and native cartilage: Fractional-order models. Journal of Magnetic Resonance, 210(2):184–191, 2011.

65. Magin, R. L., Li, W., Pilar Velasco, M., Trujillo, J., Reiter, D. A., Morgenstern, A., and Spencer, R. G.: Anomalous nmr relaxation in cartilage matrix components and native cartilage: fractional-order models. J Magn Reson, 210(2):184–91, Jun 2011.

66. Metzler, R., Glackle, W. G., and Nonnenmacher, T. F.: Fractional model equation for anomalous diffusion. Physica A: Statistical Mechanics and its Applications, 211(1):13 – 24, 1994.

VITA

Publications

1. Ingo C., Magin R. L.,Colon-Perez L.,Triplett W., and Mareci T. H., On random walks and entropy in diffusion weighted magnetic resonance imaging studies of neural tissue, Magnetic Resonance in Medicine, DOI: 10.1002/mrm.24706, 2013.
2. Magin R. L.,Ingo C.,Colon-Perez L.,Triplett W., and Mareci T. H., Characterization of anomalous diffusion in porous biological tissues using fractional order derivatives and entropy, Microporous and Mesoporous Materials, DOI: 10.1016/j.micromeso.2013.02.054, 2013.
3. Magin R. L. and Ingo C., Entropy and information in a fractional order model of anomalous diffusion, IFAC Proceedings on System Identification, vol. 16, no. 1, DOI: 10.3182/20120711-3-BE-2027.00063, 2012.
4. Magin R. L. and Ingo C., Spectral entropy in a fractional order model of anomalous diffusion, Carpathian Control Conference (ICCC), DOI: 10.1109/CarpathianCC.2012.6228687, 2012.

Talks

1. White Matter Study Group, Annual International Society of Magnetic Resonance in Medicine (ISMRM), Salt Lake City, UT, April 20-26 2013
2. Department of Biomedical Engineering, Northwestern University, Chicago, IL, April 10th, 2013 (invited)
3. Annual Biomedical Engineering Society Annual Conference (BMES), Atlanta, GA, October 26th, 2012
4. Magnetic Resonance in Porous Materials (MRPM), University of Surrey, Gilford, UK, September 10th, 2012
5. Department of Radiology, St George's, University of London, London, UK, July 19th, 2012 (invited)
6. MRI Research Center, Leiden University, Leiden, NL, July 16th, 2012 (invited)
7. Annual International Federation of Automation and Control (IFAC) Symposium on System Identification (SysID), Brussels, Belgium, July 12th, 2012
8. International Carpathian Control Conference (ICCC), High Tatras, Slovakia, May 29th, 2012
9. Annual Experimental Nuclear Resonance (ENC) Conference, Miami, FL, April 19th, 2012
10. NSF Workshop on Stochastic Transport and Emergent Scaling in Earth Surface Processes (STRESS 3), Glenbrook, NV, November 1st, 2011

Poster Presentations

1. Annual International Society of Magnetic Resonance in Medicine (ISMRM), Salt Lake City, UT, April 20-26 2013
2. Annual Experimental Nuclear Resonance (ENC) Conference, Miami, FL, April 12-19, 2013

Service Activities

1. Referee, *Translational Neuroscience* 2012-present
2. Member, Program Committee, Fractional Signals and Systems, Ghent University, Belgium Nov 7-8 2013
3. Editor-in-Chief, *UIC Bioengeering Student Journal* 2012-Present

Awards

1. International Institute of Education Whitaker Scholar Grant. Leiden University, Leiden, Netherlands, 2013 – 2015.
2. Honorable Mention, Best Poster Presentation, White Matter Study Group, annual conference of International Society for Magnetic Resonance in Medicine. Salt Lake City, Utah, 2013.
3. Stipend award for annual conference of International Society for Magnetic Resonance in Medicine. Salt Lake City, Utah, 2013.
4. Stipend award for annual conference of Experimental Nuclear Resonance Conference (ENC). Miami, Florida, 2012.
5. NSF fellowship award for Symposium on Biocomplexity. Istanbul, Turkey, 2011.